Microwave Transmission-Line-Based Chirped Electromagnetic Bandgap Structures

Joshua D. Schwartz

Department of Electrical and Computer Engineering
McGill University, Montréal, Canada
December 2007

A thesis submitted to the Faculty of Graduate Studies and Research in partial fulfillment of the requirements of the degree of Doctor of Philosophy

Your file Votre référence
ISBN: 978-0-494-50992-0
Our file Notre référence
ISBN: 978-0-494-50992-0

To my parents, who always knew they had a smart one on their hands
and made sure that everyone else knew, too.

Abstract

Although the concepts of chromatic dispersion and chirp are far from new in the world of wireless microwave communication, their application has always been constrained by the limited bandwidths, insertion losses and integration issues of dispersive devices. Often, a microwave designer seeking to incorporate chirping would fall back on surface-acoustic-wave structures, which are very lossy and do not easily penetrate into the GHz frequency-band, or else photonics-based solutions (e.g. chirped fiber Bragg gratings), which provide high bandwidths but incur integration and cost issues. This is in part due to the perceived lack of a convenient dispersive structure in electronics that is sufficiently low-loss and broadband in the GHz frequency range. Such a structure has in fact been recently demonstrated: it is a chirped electromagnetic bandgap (CEBG), and our work has explored its potential in a number of ultra-wideband sub-systems designed to perform a variety of signal processing tasks. Of particular interest is the close-fitting synergy between the operational frequencies of this new structure and the rapidly emerging ultra-wideband (UWB) wireless technology, which strives to handle signals with fractional bandwidths that can exceed 100% -a task for which CEBGs are well-suited.

This thesis details the first demonstrations of several practical microwave sub-systems made possible by employing dispersive CEBG structures implemented in transmission-line technologies at a bare minimum of cost and complexity. Many of these demonstrations challenge the assumption that transduction to the optical or acoustic domain is required in order to perform dispersion-enabled tasks on very broadband electrical signals.

Among the first-time demonstrations explored in the course of this thesis are: 1) passive, real-time Fourier transformations using CEBG structures, enabling time-domain measurement and processing based on the frequency content of

signals; 2) UWB tunable time-delay systems, capable of voltage-controlled, continuously-adjustable nanosecond-scale delays; 3) temporal imaging systems, for which we demonstrate a 5X time-magnification system for distortionless bandwidth-conversion; and 4) multi-frequency resonators designed to pass a number of resonant channels in a very broad stopband. Each demonstrated system represents a simple, fully-electronic solution to challenges facing the microwave community in subjects as diverse as analog-to-digital conversion, UWB communication, and arbitrary waveform generation.

Résumé

Même si les concepts de dispersion chromatique et de modulation linéaire de fréquence sont loin d'être nouveaux dans le monde de la communication sans fil par micro-ondes, leurs applications ont toujours été restreintes par les limites des bandes passantes, les pertes de puissance et les défis d'intégration des dispositifs dispersifs. Pour incorporer la modulation linéaire de fréquence, un concepteur de circuits micro-ondes s'en remettait souvent aux structures émettant des ondes acoustiques de surface, qui s'atténuent rapidement et qui rejoignent difficilement la bande de fréquences des GHz, ou encore les solutions d'origine photonique (comme les réseaux de Bragg sur fibre à modulation linéaire de fréquence), qui offrent de larges bandes passantes, mais qui entraînent des problèmes d'intégration et de coûts. Cela est explicable en partie par le supposé manque de structure dispersive électronique pratique dont la bande passante soit assez large et qui entraîne assez peu de pertes tout en étant convenable pour les fréquences dans la portée des GHz. Or, l'existence d'une telle structure a été démontrée récemment : il s'agit d'une bande interdite électromagnétique à modulation linéaire de fréquence (CEBG, soit *chirped electromagnetic bandgap*). Nos travaux ont exploré son potentiel dans bon nombre de sous-systèmes à ultralarge bande conçus pour effectuer diverses tâches de traitement des signaux. Ce qui est tout particulièrement intéressant est la grande synergie entre les fréquences de fonctionnement de cette nouvelle structure et la technologie sans fil à ultralarge bande (ULB), qui occupe une place de plus en plus importante. La technologie sans fil à ULB doit transmettre des signaux dont le ratio entre la fréquence et la bande passante peut dépasser 100 % : il s'agit d'une tâche pour laquelle les CEBG sont très bien adaptés.

La présente thèse présente les premières démonstrations d'une variété de sous-systèmes à micro-ondes pratiques rendus possibles grâce à l'utilisation de la

structure CEBG dispersive, incorporée aux technologies de lignes de transmission avec un minimum de coûts et de difficultés. Bon nombre de ces démonstrations remettent en question la supposition que la transduction aux domaines optique ou acoustique est nécessaire afin d'effectuer, sur des signaux électriques à très large bande, des tâches possibles grâce à la dispersion.

Les démonstrations innovatrices explorées par la présente thèse comprennent : 1) des transformations de Fourier passive en temps réel à l'aide de structures CEBG, ce qui permet des mesures dans le domaine temporel et le traitement basé sur les fréquences des signaux; 2) des systèmes temporisés à ULB accordables, capables de créer des délais de l'ordre de la nanoseconde continuellement ajustables et commandés en tension; 3) des systèmes d'imagerie temporelle, pour lesquels nous démontrons un système de grossissement temporel 5X permettant de convertir la bande passante sans distorsion; et 4) des résonateurs multifréquence conçus pour transmettre certains canaux résonants dans une bande atténuée très large. Chaque système démontré représente une solution simple et entièrement électronique aux défis auxquels fait face la communauté travaillant avec des micro-ondes, dans des sujets aussi variés que la conversion de l'analogique au numérique, la communication à ULB et la génération de signaux à formes arbitraires.

Acknowledgements

This work would not have been possible if not for the tireless dedication and guidance provided by my supervisors. My deepest thanks must go to David Plant for helping me to fully realize my potential. I am profoundly grateful for his constant encouragement; over many years he has helped me to overcome my self-doubts and clearly see the formidable strength and significance of my body of work. I was also very fortunate for the guidance of José Azaña, whose enthusiasm for research is absolutely contagious, and whose boundless ideas inspired this work and certainly many more to come. I will always consider Dave and José to be friends as well as mentors.

Many people have directly contributed to my research and I would like to acknowledge their contributions here. Many thanks go to Raphael Bouskila, Mike Guttman, Noha Kheder and Marija Nikolic for their dedicated assistance in design, simulation and layout; to Don Pavlasek from the departmental machine shop; to Robert Morawski and Tho Le-Ngoc for their assistance with measurement equipment; to Israel Arnedo, Miguel Ángel Gómez Laso and Txema Lopetegi at the University of Navarre for enlightening discussion on bandgap structures; and to Lawrence Chen, Mourad El-Gamal and Ramesh Abhari for their thoughtful answers to my questions over the years.

The research group I worked in was second-to-none and full of friendly people I came to know along the way. My deepest thanks go out to the many past and present members of the Photonics Systems Group: Madeleine Mony, Eric Bisaillon, Julien Faucher, Wei Tang, Jean-Philippe Thibodeau, Michael Venditti, Dave Rolston, Dominik Pudo, Rhys Adams, Michael Menard, Alan Lee, Bhavin Shastri, Christian Habib, Alaa Hayder, Veronique Pagé, Cristina Marinescu, Eduardo Lugo, Jacques Laniel, Nicolas Bélanger, Colin Alleyne, Reuven Gordon, Shafique Jamal, and Varghese Baby. Sincere apologies to anybody I may have

missed. I must also give special thanks to Chris Rolston, Carrie Serban and Kay Johnson for their administrative assistance and their constant willingness to help.

I would like to acknowledge the generous financial assistance of the National Science and Engineering Research Council of Canada (NSERC), which provided me with the Canada Graduate Scholarship (CGS-M) and Postgraduate Scholarship (PGS-B) that supported me during my research, as well as SYTACom for sponsoring my conference-related travel.

I am blessed with the warmth and loving support of my wonderful fiancée, Amélie, who helps me translate difficult technical abstracts into French with the same kind of steady assuredness she shows when she makes sure I'm wearing a warm-enough winter jacket to go outside in. Her companionship and love serve as an inspiration for this achievement and many more to come.

Finally, I wish to thank my family for always cheering me on –my parents Louise and Moses, my grandparents, uncles & aunts, cousins, and all of my extended family: Robin, Ari & Jordan, and Tony. Thank you all for encouraging me on the path to this thesis, and for those times you've all spent smiling at my indecipherable publications (which I am always happy to try to explain). This work would not have been possible were I not surrounded by such an amazing and supportive group of people.

Table of Contents

Chapter 1: Introduction

1.1 Motivation 1
1.1.1 Ultra-Wideband Systems 5
1.1.2 Real-time Spectral Analysis 7
1.1.3 Tunable Time-Delay Systems 8
1.1.4 Analog-to-Digital Conversion 8
1.1.5 Arbitrary Waveform Generation 10
1.2 Thesis Objectives 10
1.3 Thesis Organization 12
1.4 Original Contributions 13
References 13

Chapter 2: Chirped Electromagnetic Bandgap Structures

2.1 Review of the Literature 19
2.1.1 Electromagnetic Bandgap Structures 19
2.1.2 The Chirped EBG (CEBG) 24
2.2 Methodology & Prototype Design 29
2.2.1 Simulation Tools 29
2.2.2 Fabrication 29
2.2.3 Characterization 30
2.3 Real-Time Fourier Transformation 31
2.3.1 Background and Application 31
2.3.2 Demonstration 33
2.3.3 Conclusions 35
References 35

Chapter 3: Tunable Time-Delay Systems

3.1 Introduction 43
3.1.1 Areas of Application 43
3.1.2 Existing Techniques 46
3.2 Tunable TTD System 48
3.2.1 Proposed Design 48
3.2.2 Simulation & Measurement Results 51
3.2.3 Conclusions 55
References 55

Chapter 4: Temporal Imaging Systems

4.1 Introduction 59
4.1.1 Definition and Applications 59
4.1.2 Theory of Temporal Imaging 61
4.1.3 Review of Existing Techniques 65
4.2 An Electronic Time-Magnification System 71
4.2.1 Dispersion Elements 71
4.2.2 Electronic Time-Lens 73
4.2.3 Simulation and Measurement Results 75
4.2.4 Discussion 78
4.3 Electronic Time-Compression and Reversal Systems 81
4.3.1 Time-Compression 81
4.3.2 Time-Reversal 85
4.3.3 Conclusions 87
References 87

Chapter 5: Specialty CEBG Designs

5.1 Multiple-Frequency Resonant CEBGs 91
5.1.1 Phase-Shifted CEBGs 93
5.1.2 Moiré-Patterned CEBGs 95
5.2 CEBGs in Other Media 98

5.2.1 Stripline 98
5.2.2 Coplanar Waveguide 100
5.2.3 Other Media 101
5.2.4 Conclusions 102
References 102

Chapter 6: Conclusions

6.1 Summary 105
6.2 Future Research 106
6.2.1 Sub-Wavelength Structures 107
6.2.2 Deployment of CEBGs for Continuous-Time Operations 107
References 108

Appendix A – Theory of Temporal Imaging

Appendix B – Analog Multiplier

Associated publications and contribution of authors

The work reported in this thesis has been published or will be published in the form of the following journal articles and conference papers. The author of this thesis is solely responsible for all design, analysis and experimental and simulation work involved in these publications *except* as noted below:

- Israel Arnedo assisted in generating an ultra-wideband test pulse to test the system described in [1].
- Michael Guttman contributed to the simulation of several chirped-Moiré and phase-shifted CEBG structures as described in [2], [8].
- Michael Guttman, Noha Kheder and Marija Nikolic assisted in the design and layout of the analog multiplier described in [3], [7].
- Raphael Bouskila assisted in carrying out several designs and simulations involving stripline and coplanar waveguide structures (Chapter 5).

Journal Articles

[1] J. Schwartz, I. Arnedo, M. A. G. Laso, T. Lopetegi, J. Azaña and D. V. Plant, "An electronic UWB continuously tunable time-delay system with nanosecond delays," accepted for publication, IEEE Microwave Compon. Lett., Feb. 2008.

[2] J. Schwartz, Michael M. Guttman, J. Azaña and D. V. Plant, "Multi-Channel Filters Using Chirped Bandgap Structures in Microstrip Technology," IEEE Microwave Compon. Lett., vol. 17, no. 8, pp. 577-9, Aug. 2007.

[3] J. Schwartz, J. Azaña and D. V. Plant, "A fully-electronic system for the time magnification of GHz electrical signals," IEEE Trans. Microwave Theory Tech., vol. 55, no. 2, pp. 327-334, Feb. 2007.

[4] J. Schwartz, J. Azaña and D. V. Plant, "Experimental demonstration of real-time spectrum analysis using dispersive microstrip," IEEE Microwave Compon. Lett., vol. 16, no. 4, pp. 215-217, Apr. 2006.

Conference Papers

[5] J. Schwartz, J. Azaña and D. V. Plant, "An electronic temporal imaging system for compression and reversal of arbitrary UWB waveforms," to be presented at IEEE Radio & Wireless Symp. (RWS 2008), Orlando, FL, Jan. 2008.

[6] J. Schwartz, J. Azaña and D. V. Plant, "Design of a tunable UWB delay-line with nanosecond excursions using chirped electromagnetic bandgap structures," Proc. 4th IASTED Int. Conf. Antennas, Radar and Wave Propagation (ARP 2007), #566-814, May 2007.

[7] J. Schwartz, J. Azaña and D. V. Plant, "A fully-electronic time-stretch system," **Best Student Paper**, 12th Int. Symp. Antenna Technology and Applied Electromagnetics (ANTEM/URSI), pp. 119-22, Jul. 2006.

[8] J. Schwartz, M. Guttman, J. Azaña and D. V. Plant, "A multiple-frequency resonator in microstrip technology," 12th Int. Symp. Antenna Technology and Applied Electromagnetics (ANTEM/URSI), pp. 569-72, Jul. 2006.

[9] J. Schwartz, J. Azaña and D. V. Plant, "Real-time microwave signal processing using microstrip technology," IEEE MTT-S Int. Microwave Symp. Dig., San Francisco, CA, pp. 1991-4, Jun. 2006.

Other publications that do not directly relate to this thesis

[10] J. Schwartz, M. B. Venditti, and D. V. Plant, "Experimental techniques using optically-enabled ring oscillators," Appl. Opt. (Opt. Soc. America), vol. 43, no. 12, pp. 2456-61, Apr. 2004.

[11] M. B. Venditti, J. Schwartz, and D. V. Plant, "Skew reduction for synchronous OE-VLSI receiver applications," IEEE Photonics Technol. Lett., vol. 16, no. 6, pp. 1552-4, Jun. 2004.

[12] M. Kulishov, V. Grubsky, J. Schwartz, X. Daxhelet, D. V. Plant. "Tunable waveguide transmission gratings based on active gain control," IEEE J. Quantum Electron., vol. 40, no. 12, pp. 1715-24, Dec. 2004.

[13] M. Kulishov, X. Dahelet, V. Grusbky, J. Schwartz and D. V. Plant, "Distinctive behaviour of long-period gratings in amplifying waveguides," Conf. Opt. Fiber Commun. Tech. Dig. Ser., vol. 2, pp. 49-51, Mar. 2005.

[14] J. Schwartz, M. Kulishov, V. Grubsky, X. Daxhelet and D. V. Plant, "Experimental Demonstration of Loss as a Tuning Mechanism in Long-Period Gratings", 30th Europ. Conf. Opt. Commun., vol. 3, pp.550-1, Sept. 2004.

[15] A.K. Sood, S. K. Bhadra, P.R. Smith, Y. R. Puri, M. Cross, J. Ueda, R. Patel, L. Jiang, W. H. Chang, G. J. Simonis, D. V. Plant, A. G. Kirk, and J. Schwartz, "Design and development of high-speed fiber-optic transmit and receive network for commercial and military applications," Proc. SPIE - Int. Soc. Opt. Eng. (USA), vol. 5556, no. 1, pp. 214-220, 2004.

[16] M. B. Venditti, J. Schwartz, and D. V. Plant, "Skew reduction for synchronous OE-VLSI receiver applications," Proc. Optics in Computing (USA), pp. 53-6, Jun. 2003.

[17] M. B. Venditti, J. Schwartz and D. V. Plant, "Phase linearity and uniformity in OE-VLSI receiver arrays," Proc. SPIE – Int. Soc. Opt. Eng., vol. 4788, pp. 58-67, Jul. 2002.

[18] M. B. Venditti, E. Laprise, L. Malic, J. Schwartz, E. Shoukry, J.-P. Thibodeau, and D. V. Plant, "Design for testability and system level test for OE-VLSI chips," Proc. Optics in Computing, Taipei, Taiwan, pp.144-6, Apr. 2002.

Abbreviations

ADC	Analog-to-digital conversion
AWG	Arbitrary waveform generation
CEBG	Chirped electromagnetic bandgap
CMOS	Complementary metal-oxide semiconductor
CPW	Coplanar waveguide
DSB	Double-sideband
EBG	Electromagnetic bandgap
FBG	Fiber Bragg grating
MoM	Method of Moments
PBG	Photonic bandgap
PCB	Printed circuit board
RF	Radio-frequency
RTFT	Real-time Fourier transform
SAW	Surface acoustic wave
SMA	Sub-Miniature 'A' (a common RF connector type for <18 GHz)
SSB	Single-sideband
TTD	True time-delay
UWB	Ultra-wideband
VCO	Voltage-controlled oscillator
VNA	Vector network analyzer

CHAPTER 1

Introduction

A good scientist is a person with original ideas.
A good engineer is a person who makes a design that works with as few original ideas as possible.
-Freeman Dyson

1.1 Motivation

The phenomenon of chromatic dispersion, the understanding of which is of fundamental importance in the realm of optical communication, does not ordinarily inform the design of entirely electronic systems. This is primarily because while optical network engineers must grapple with the challenges of sending data through dispersive optical fibers, the chromatic dispersion of a typical electrical transmission line is, by comparison, a non-issue for most microwave engineers. Electronic systems *do* have a long history of interacting with dispersive transmission taking place in *other* wave-propagating media. Consider, for example, the chirped[1] surface acoustic wave (SAW) structures (Fig. 1.1a) widely employed in radar and pulse compression applications [1]; the chirped fiber Bragg gratings (FBGs) (Fig. 1.1b) employed in many microwave photonic systems [2]; or even less commonly known structures such as dispersive magnetostatic lines [3]. Clever electronic design has also been employed to perform dispersion compensation to correct for the degrading effect of optical fiber dispersion on long-haul optical links [4]. As it stands in native electrical media, however, strongly dispersive transmission lines spanning the microwave band are either relatively obscure (see, for example, some superconducting chirp filters [5]) or non-existent. This stands in stark contrast to the functional

[1] In this text, I will sometimes use the descriptive term "chirped" interchangeably with "dispersive" to indicate a structure that introduces non-linear phase behavior, although the former word often implies "by design" whereas the latter generally refers to the material phenomenon (e.g. a chirped filter to compensate for a dispersive optical fiber). In this work, "chirp" will also come to predominantly refer to the specific case of "linear frequency chirp" (quadratic phase filtering).

versatility of dispersive lines, as is evidenced by the vast body of work on chirped SAW and FBG structures, which are commonly employed to perform such diverse functions such as real-time spectral analysis [6]-[8], pulse shaping and tunable time-delays [9], and broadband filtering [10], or else form a key part of systems for spread-spectrum communication [11] and temporal imaging [12], to give only a few examples.

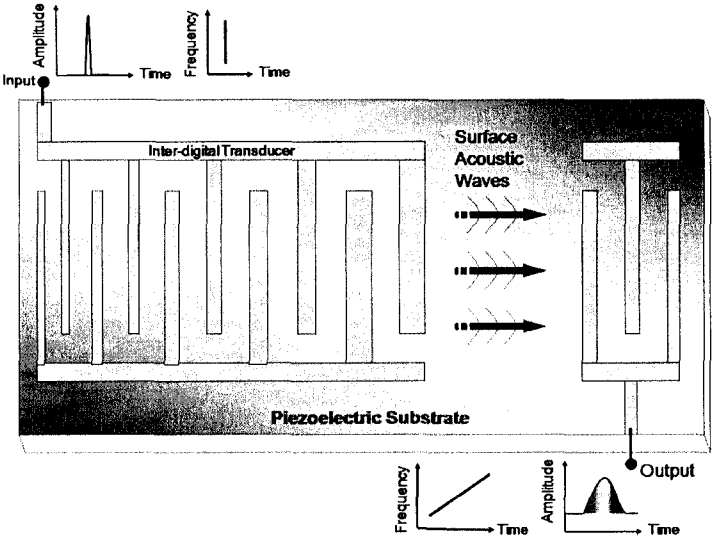

(a)

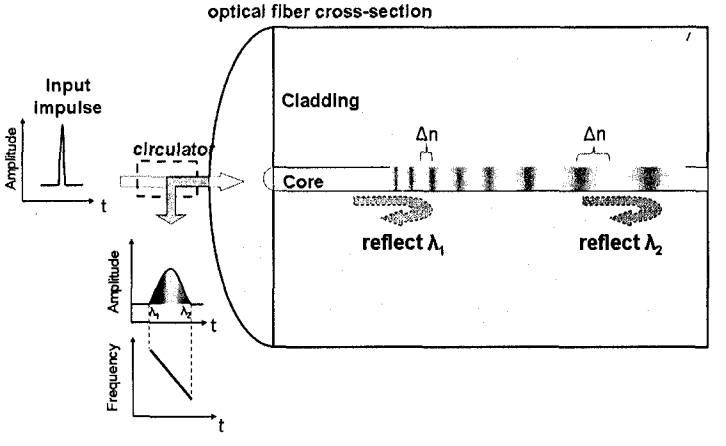

(b)

Fig. 1.1 Representations of (a) a chirped SAW structure on a piezoelectric substrate and (b) a chirped FBG in a standard optical fiber.

Presently, an increasing number of radar and communications systems are targeting operation in the 3-20 GHz range with fractional bandwidths approaching

and sometimes exceeding 100%. These are now commonly referred to as ultra-wideband (UWB) systems (see Section 1.1.1), and their development is accompanied by a need for equally broadband arbitrary waveform generators (AWG), high data-rate analog to digital converters (ADC), real-time spectrum analyzers, and a host of other components. Building a signal processing toolbox for UWB signals represents a compelling engineering challenge, and it is no surprise that many engineers seeking to deploy dispersion in their design strategies have turned to SAW- and photonics-based solutions. Unfortunately, SAW structures, apart from being characteristically very lossy, are generally limited by lithographical constraints to operating frequencies below 3 GHz and sub-GHz bandwidths without resorting to sophisticated and costly fabrication techniques [13], [14]. Magnetostatic solutions, although they can operate at GHz frequencies, are similarly very lossy and band-limited [15]. Photonics-based solutions have comfortable access to broadband, low-loss dispersion, and although vastly liberating in terms of bandwidth, they are frequently expensive and difficult to integrate with electronic systems. This highlights an obvious problem: there exists no suitably low-loss and broadband dispersive device native to the UWB frequency range that is convenient for integration to perform the kinds of functions outlined above [6]-[12].

This thesis investigates a structure that is well-positioned to fill this gap: the chirped electromagnetic bandgap (CEBG) transmission line (Fig. 1.2). As frequencies increase to the range that makes SAW structures too small for basic lithographic techniques, the decreasing signal wavelength invites the use of the planar metallo-dielectric periodic constructs known as electromagnetic bandgap (EBG) structures. EBGs have recently attracted a lot of research interest (see Chapter 2), and with the first demonstration of a chirped implementation of an EBG [16], highly dispersive structures in the UWB frequency regime become possible having extremely large fractional bandwidths (125% was demonstrated in [16]) and manageable insertion losses (~2-3 dB with inclusion of directional coupling, see Chapter 2). Furthermore, CEBGs are very simple to fabricate in very mature technologies such as microstrip and stripline, with the primary

drawback being their necessary length, which (depending on choice of substrate, target bandwidth and chirp) is of the order of tens of cm with the possibility of meandering.

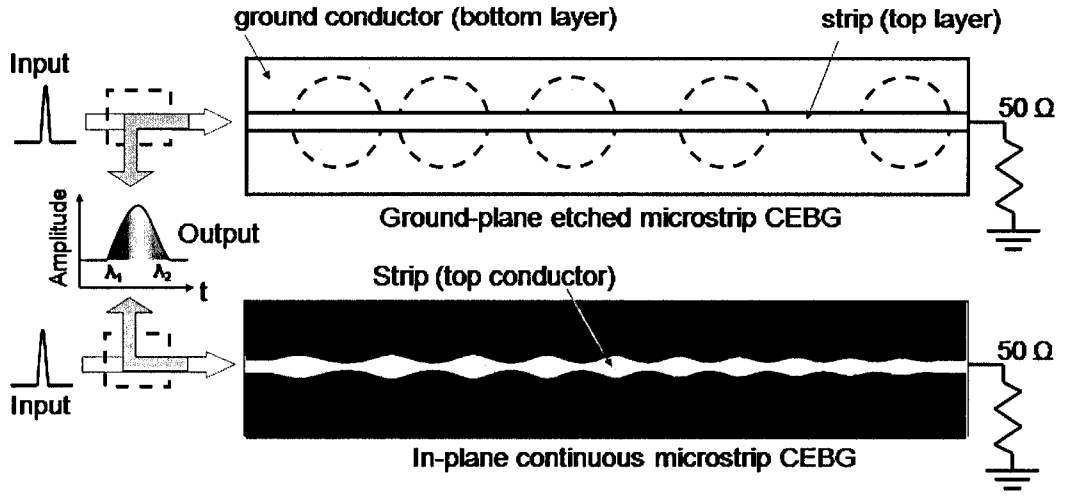

Fig. 1.2 Representations of two CEBG-type designs – using circles patterned in the ground plane underneath a microstrip (top) and the other with perturbations directly in the microstrip center conductor (below).

Table 1.1 helps to situate CEBG devices in comparison to other dispersive structures for different media and summarizes their overall capabilities. It becomes immediately evident in comparing CEBG structures to chirped-SAW designs (a highly popular radar component) that CEBGs represent a tradeoff in size (board-scale structures) and delay (nanosecond-scale instead of microseconds for SAW structures) for higher bandwidths and much lower losses. CEBGs yield a comparable delay performance to chirped FBGs and occupy similar sizes – although FBGs become difficult to fabricate at lengths exceeding 10 cm. One particular figure of merit in dispersive delay lines is the time-bandwidth product (TBP), a common measure of dispersive line performance that accounts for the fact that the total time-delay associated with a chirped line is customarily linked in a tradeoff with its bandwidth. For CEBGs, the TBP is small in comparison to acoustic/magnetic methods (since they lack the large delays) and optical chirped FBGs (since they span microwave and not optical bandwidths). Despite this drawback, we will demonstrate that CEBGs are, by virtue of their broad

microwave bandwidths and simple fabrication, an attractive alternative to these devices.

Table 1.1
Typical performance values for chirped dispersive structures

	Medium	Typ. Line Delay	Typ. Frequencies (Bandwidth)	TBP	Typ. Insertion Losses	Scale
Chirped SAW	Piezoelectric substrate	Tens of μs	<3 GHz (<1 GHz)	1000-10,000	>20 dB	**A few sq. mm**
Magneto-statics	Ferrite-layer stacks	100s of ns	2-12 GHz (<1 GHz)	~250	15-40 dB, frequency dependent	**A few cm**
Chirped FBG	Optical fiber	~1-2 ns	~100 THz (>500 GHz)	1,000	~ 2-3 dB[1]	**~1-15 cm**
CEBG	**Dielectric substrate**	**~1-4 ns**	**~10 GHz**	**~30**	**~ 2-3 dB[1]**	**Tens of cm**

[1] includes the required directional coupling

We will now briefly point to several key areas of research which motivated this work and in which the CEBG is poised to contribute.

1.1.1 Ultra-Wideband Systems

An emerging technology in the domain of wireless communication, UWB systems are popularly defined as those in which information is encoded in short-time pulses occupying more than 500 MHz or 20% instantaneous bandwidth, while being of sufficiently low power spectral density to not interfere with legacy (narrowband, carrier-based) systems. The popularity of this technology was spurred in 2002 when the Federal Communications Commission in the United States de-licensed the use of the frequency band 3.1-10.6 GHz for the purposes of UWB, stipulating that the equivalent isotropic radiated power (EIRP) of UWB signals must not exceed -41.3 dBm/MHz [17]. Pulse-based UWB microwave technologies, both with and without signal carriers (Fig. 1.3), are now being

targeted for a broad range of scientific, industrial and military applications with end-use markets that can roughly be assigned into two broad categories:

1) Short-distance low- and high-data-rate wireless applications such as wireless peripherals (e.g. monitors, DVD players) and data-transfers to/from mobile devices (e.g. audio players, digital cameras to printing equipment), in residential and industrial settings [17]-[20]. In this field, UWB systems are valued for having a high user capacity while being robust against multipath effects.
2) Vehicular, biomedical and military imaging systems and radars, featuring high-precision resolution and asset localization, immunity to interference and noise, and "see-through-wall" imaging capabilities [21]-[23].

Signal processing tools and sub-systems in (and beyond) the FCC-specified band are presently the subject of increased research, and low-loss structures that can accommodate UWB technology are in high demand. The overlap in bandwidths of UWB systems and typical EBG structures makes EBGs particularly attractive as broadband filters, pulse-shapers, and in the case of the CEBGs presented here, as practical sources of dispersion as well.

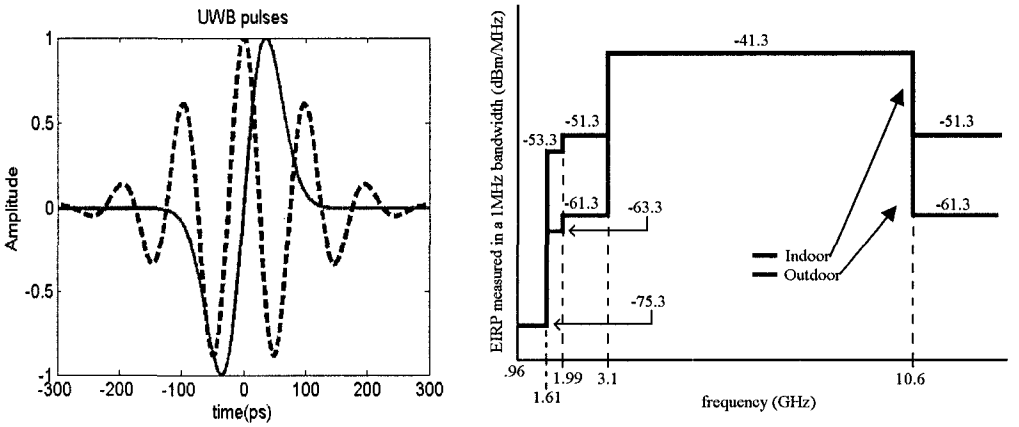

Fig. 1.3 (Left) Example UWB pulses: a baseband monocycle, the first derivative of a Gaussian pulse (solid) and an UWB Gaussian pulse on a carrier (dashed); (Right) FCC-specified EIRP spectral mask for UWB systems.

The applications in the following sections are all potential sub-systems of interest to UWB communication, but also stand on their own merits as signal processing tools enabled by dispersion.

1.1.2 Real-time Spectral Analysis

Real-time spectral analysis captures the essential functions of an oscilloscope and a spectrum analyzer in a single device by making one-shot measurements of time-varying frequency content. The most straightforward way to do this is to map an incident signal's spectral characteristics directly into the time-domain through a real-time Fourier transformation (RTFT), and thus the frequency content can be directly monitored and processed using time-domain methods.

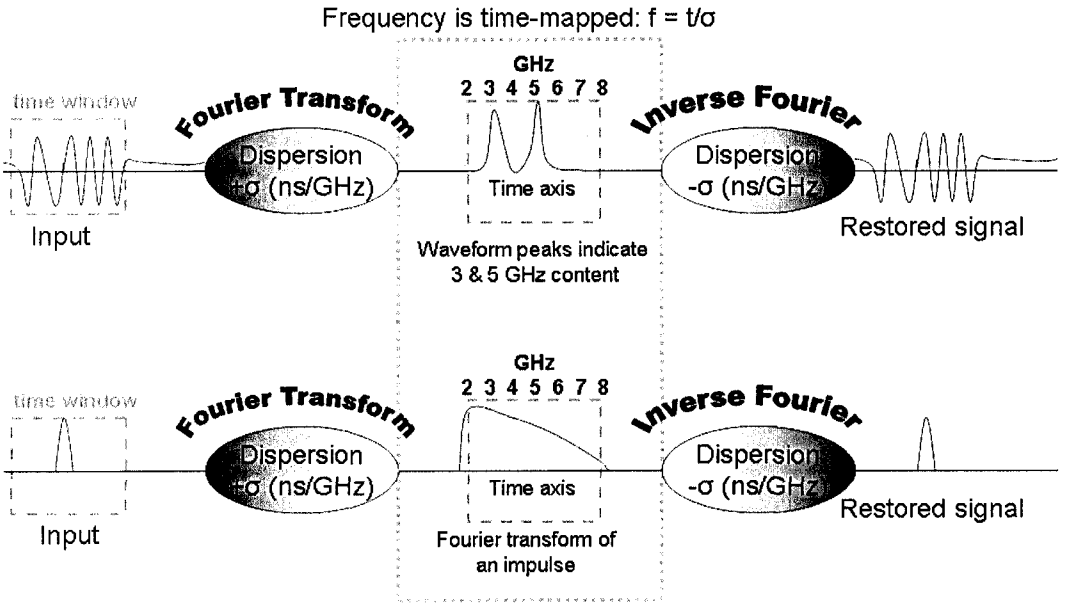

Fig. 1.4 Conceptual illustration of real-time Fourier transformation using dispersion, including restoring the signal via the inverse-Fourier transform. Note that the Fourier transforms shown are bandpass in nature (this will be the case for CEBGs).

If a transmission line is sufficiently dispersive, any time-windowed input signal passing through the line will be re-ordered in time according to its frequency content [24], with a straightforward one-to-one correspondence between each time point 't' and each represented frequency 'f', according to $f = t/\sigma$, where 'σ' is the group delay slope (s/Hz) (see Section 2.1.2 for more detailed discussion). The transformed signal can be detected and traced using an oscilloscope (spectral analysis), or else be otherwise processed in the time-domain according to its frequency content. Frequency filtering, convolution and correlation functions can all be carried out in the time domain, with the possibility

of performing an inverse-Fourier operation on the result using a transmission line having the opposite sign of dispersion to restore the signal (Fig. 1.4).

Dispersive structures for RTFT have been demonstrated in SAW and FBG technologies [25], [26]. Most of today's commercial spectral analyzers are based on digital processing and fast Fourier transform algorithms; state-of-the-art analyzers can display real-time instantaneous bandwidths in the hundreds of MHz (e.g. Tektronix RSA6100A) and are steadily improving. We will demonstrate in Chapter 2 that a CEBG transmission line can potentially perform very wide-bandwidth RTFTs of limited resolution in a passive, analog fashion, making them potentially interesting tools for broadband real-time spectral analysis systems.

1.1.3 Tunable Time-Delay Systems

Broadband adjustable time-delay stages are important components for the operation of phased-array antennas (PAAs) [27], as well as in wireless UWB communication, where they have use in modulation/demodulation schemes based on pulse-position, and in UWB receivers and radars, where they make possible the synchronization (and in cases such as noise radar [28], correlation) of received pulses with locally generated references. The nominal characteristics of a delay stage for a UWB receiver are: small-area, low-loss, wideband (FCC mask), with a continuously adjustable delay excursion of up to 1 ns [29]. Many existing electronic schemes (discussed in Chapter 3) meet with success in some categories, however it is in achieving nanosecond-scale delays that a significant technical challenge emerges. Photonics-assisted techniques have demonstrated very broadband nanosecond-scale delay ranges [30] but typically necessitate inconvenient optical hardware. In Chapter 3, we will demonstrate a simple, fully-electronic system using CEBGs for achieving a continuously tunable UWB delay on the order of nanoseconds.

1.1.4 Analog-to-Digital Conversion

Fast analog-to-digital conversion (ADC) is one of the cornerstone challenges in modern high-speed communication systems. In order to process analog signals using powerful digital signal processing techniques, the signal must first be

sampled in real-time at a sufficiently fast rate to capture the details of the input waveform, which becomes increasingly challenging as the bandwidth of the analog input enters the GHz range. Digital UWB radio applications can require ADC bandwidths on the order of 10 GHz, which is prohibitively difficult with conventional designs [31]. Aggressive modern ADC designs can push the input bandwidths with diminishing returns in resolution [32]. Parallel synchronous deployment of large numbers of ADCs is one strategy that has been adopted to compensate, although it becomes increasingly difficult to properly coordinate a large number of samplers [33].

The prospective role of dispersive devices in approaching this problem is evidenced by the possibility of time-stretching (temporally imaging) an analog waveform prior to the sampling phase (Fig 1.5). Time stretching effectively reduces the bandwidth of an input signal without introducing distortion, and has been proposed and demonstrated using dispersive photonic components for the purposes of ADC [34], [35]. In Chapter 4, we will propose and demonstrate, using CEBGs, the first fully-electronic implementation of such a time-stretching system in the GHz regime, with the potential for extension into a continuous system for cheaply and effectively increasing the effective sampling rate of ADC.

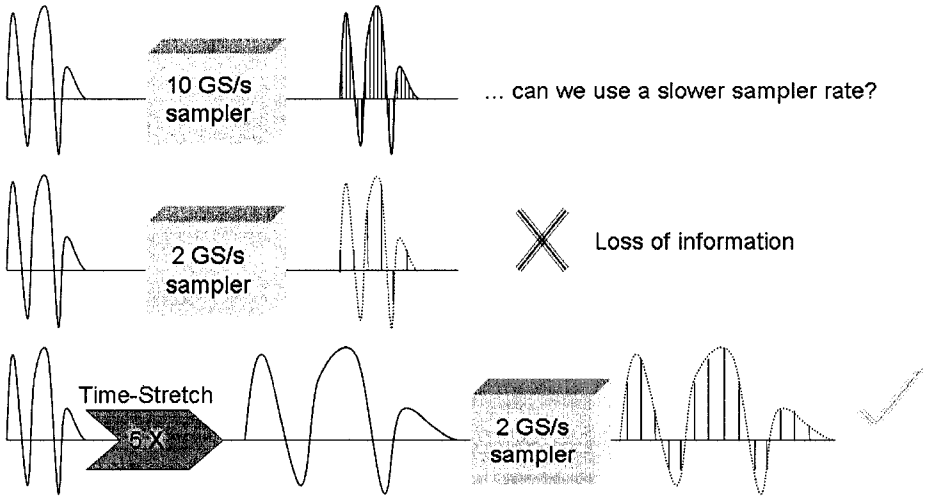

Fig. 1.5 Use of a time-stretch block in analog-to-digital conversion permits slower, simpler sampling modules to be used to capture the details of fast waveforms.

1.1.5 Arbitrary Waveform Generation

Another key challenge facing UWB communication lies in the generation of arbitrary user-specified UWB pulse-shapes [35]-[38]. Current commercial tools for electromagnetic arbitrary waveform generation (AWG) are limited to signal content up to 5 GHz (e.g. the Tektronix AWG7000); however, the development of practical, cost-effective techniques for the generation and processing of customized pulse-shapes with frequency content spanning the 3.1-10.6 GHz FCC mask for UWB communication is a crucial step for the deployment of pulse-based UWB systems. The optimal UWB pulse features are dictated by the targeted application and the impact of co-existence with other spectrum users. Specifically, orthogonal pulse-shapes are expected to generate a lot of interest. Numerous pulse designs for UWB applications have been proposed in the literature, each having unique advantages and ranges of application [36], [37].

Research in high-frequency pulse-shaping has focused on using photonics techniques where electrical UWB signals are processed in the optical domain using photonics components [38], [39]. Although this approach benefits from the extremely large bandwidths available in the optical domain, optical solutions are undesirable for microwave systems since they typically involve expensive and difficult-to-integrate optical hardware such as mode-locked laser sources, which are difficult to handle and operate. In Chapter 4, we will illustrate how a fully-electronic time-compression technique using CEBGs could be used to generate an arbitrarily-shaped pulse by compressing in time (expanding in bandwidth) an existing, lower-frequency waveform as generated by an AWG unit.

1.2 Thesis Objectives

The main objective of this thesis is to provide experimental proof of the viability of CEBG structures in sub-systems intended for the applications outlined above by demonstrating the use of their dispersive properties, many of which involve the translation of existing systems employing photonic components into fully-electronic implementations. Among the demonstrations targeted are:

1) the real-time Fourier transformation of an UWB signal

2) a continuously tunable time-delay system for UWB signals
3) time-magnification and time-compression of UWB signals
4) a multi-frequency resonant filter

Since the CEBG has only recently been realized, a secondary objective is to explore CEBG design and denote the practical limitations of these devices in terms of operating bandwidth, device size, attainable dispersion levels and undesirable characteristics such as response ripple. To this end, we have simulated and fabricated many CEBG structures, exploring options for reducing device size (through meandering, superposition, and stacking techniques), choice of substrate, choice of technology (e.g. microstrip, stripline, coplanar waveguide) and apodization techniques. We explore a number of these parameters in the course of this work.

Much of this work is conducted in an empirical manner since the EBG synthesis techniques developed in the literature focus predominantly on single-frequency EBG structures rather than chirped implementations, which cannot be reduced to a single repeating unit cell to be subjected to the traditional analysis of periodic structures. Recent work on a general EBG synthesis tool has yielded a promising result which may be of practical use in future CEBG designs [40].

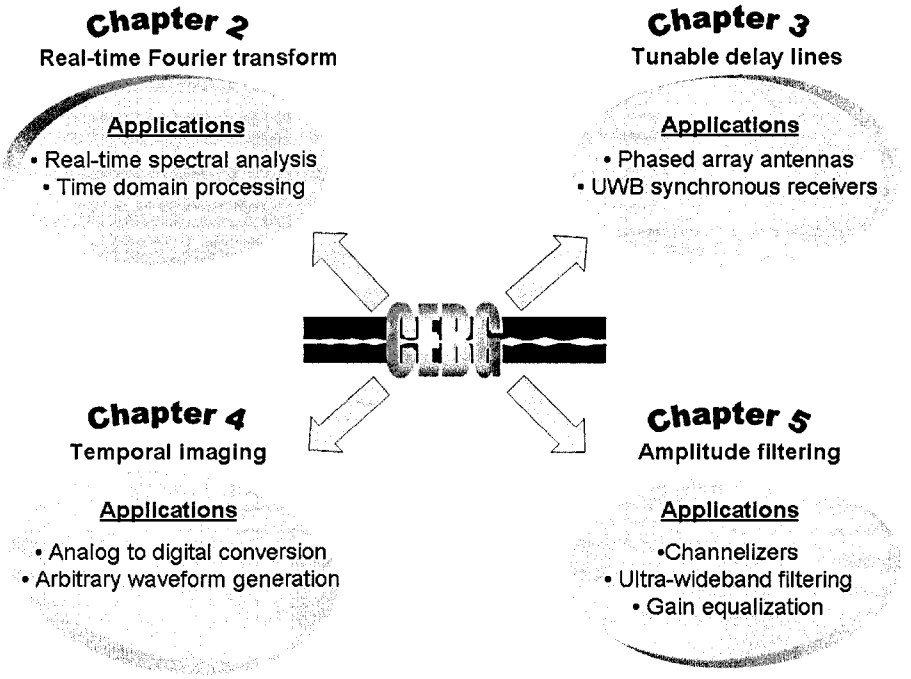

Fig. 1.6 Applications of chirped electromagnetic bandgap structures & relevant thesis chapters.

1.3 Thesis Organization

Each chapter in this thesis centers on a different application zone for CEBG structures (Fig. 1.6). The chapters begin by developing the application context for each area of research (with discussion of the relevant state-of-the-art and the literature), and then describe a relevant CEBG-implemented system demonstration.

In Chapter 2 we present a general review of the literature on EBG structures for microwave systems, including the first demonstrated CEBG structure [16]. In addition, we present an exploration of the main empirical CEBG design equation, and we describe our methodology for simulation, fabrication and test of the CEBG structures in this thesis. Finally, we present a prototype CEBG spanning the bandwidth of 4-8 GHz and demonstrate its use in performing a real-time Fourier transformation.

We describe in Chapter 3 the applications and design of tunable UWB time-delay systems, including a demonstration using CEBGs to achieve a continuously tunable nanosecond-scale delay excursion for a signal having 4 GHz bandwidth.

In Chapter 4, we briefly review the concept of temporal imaging in the context of the mathematical space-time duality, followed by a description of the areas of application of this technique. We describe and experimentally demonstrate an implementation of a fully-electronic system for the fivefold time-magnification of an incident 0.6 ns, 8 GHz bandwidth signal, and we also demonstrate how similar time-compression and time-reversal systems can be implemented using the same techniques.

In Chapter 5, we explore some alternative CEBG geometries, including special transmission-mode multi-frequency resonant filters created using superposition techniques. We also discuss and demonstrate stripline, coplanar waveguide, and other technology in which implementations of CEBGs are possible.

Finally, in Chapter 6 we discuss the future direction of this line of research, focusing on how to extend the system demonstrations of the previous chapters

through parallel processing, and possible miniaturization approaches using sub-wavelength structures and metamaterials.

1.4 Original Contributions

- First experimental demonstration of a real-time Fourier transformation using a CEBG [41], [42].
- First design and experimental demonstration of an ultra-wideband tunable time-delay system using CEBG structures [43], [44].
- First design and simulation of a fully-electronic time-compression and reversal system for signal in the GHz regime [45].
- First design and experimental demonstration of a fully-electronic time-magnification system for signals in the GHz regime [46], [47].
- Demonstration of the first chirped-Moiré EBG in microstrip and comparison with phase-shifted techniques for inserting transmission channels [48], [49].
- First demonstrations of continuous-topology CEBGs in stripline and coplanar waveguide technologies.

The journal articles and conference papers [41]-[49], including one Best Student Paper [46], that have resulted from this work show evidence of our original contributions to knowledge.

References

[1] C. Campbell, *Surface Acoustic Wave Devices and Their Signal Processing Applications*, Boston: Academic Press, 1989.

[2] J. Capmany, D. Pastor, B. Ortega, J. L. Cruz, M. V. Andres, "Applications of fiber Bragg gratings to microwave photonics," Fiber Integr. Opt., vol. 19, no. 4, pp. 483-94, 2000.

[3] D. D. Stancil, *Theory of Magnetostatic Waves*, New York: Springer-Verlag, 1993.

[4] U.-V. Koc, "Adaptive Electronic Dispersion Compensator for Chromatic and Polarization-Mode Dispersions in Optical Communication Systems," EURASIP J. Appl. Signal Process., vol.10, pp. 1584-92, Sept. 2005.

[5] H. C. H. Cheung, M. Holroyd, F. Huang, M. J. Lancaster, B. Aschermann, M. Getta, G. Müller and H. Schlick, "125% bandwidth superconducting chirp filters," IEEE Trans. Appl. Supercond., vol. 7, no. 2, pp. 2359-62, Jun. 1997.

[6] M. A. Jack, P. M. Grant and J. H. Collins, "The theory, design, and applications of surface acoustic wave Fourier-transform processors," Proc. IEEE, vol. 68, no. 4, pp. 450-468, Apr. 1980.

[7] J. Azaña, M. A. Muriel, "Real-time optical spectrum analysis based on the time-space duality in chirped fiber gratings," IEEE J. Quantum Electron., vol. 36, no. 5, pp. 517-526, May 2000.

[8] J. Azaña, L. R. Chen, M. A. Muriel and P. W. E. Smith, "Experimental demonstration of real-time Fourier transformation using linearly chirped fibre Bragg gratings," Electron. Lett., vol. 35, no. 25, pp. 2223-4, Dec. 1999.

[9] S. Xiao and A. M. Weiner, "Coherent Fourier transform electrical pulse shaping," Opt. Express, vol. 14, no. 7, pp. 3073-82, Apr. 2006.

[10] M. Chomiki, "SAW-based solutions for UWB communications," Proc. European Radar Conf. (EURAD), Paris, France, pp. 263-6, Oct. 2005.

[11] A. Springer, W. Gugler, M. Huemer, R. Koller, and R. Weigel, "A wireless spread-spectrum communication system using SAW chirped delay lines," IEEE Trans. Microwave Theory Tech., vol. 49, no. 4, pp. 754-60, April 2001.

[12] J. Azaña, N. K. Berger, B. Levit and B. Ficher, "Spectro-temporal imaging of optical pulses with a single time lens," IEEE Photon. Technol. Lett., vol. 16, no. 3, pp. 882-4, March 2004.

[13] L. Le Brizoual, F. Sarry, O. Elmazria, P. Almot, Th. Pastureaud, S. Ballandras and V. Laude, "GHz frequency ZnO/Si SAW device," IEEE Ultrasonics Symp., vol. 4, pp. 2174-7, Sept. 2005.

[14] K. Uehara, C.-M. Yang, T. Shibata, S.-K. Kim, S. Kameda, H. Nakase and K. Tsubouchi, "Fabrication of 5-GHz-band SAW filter with atomically-flat-surface AlN on sapphire," IEEE Ultrasonics Symp., vol. 1, pp. 203-6, Aug. 2004.

[15] M. R. Daniel, J. D. Adam and P. R. Emtage, "Dispersive delay at gigahertz frequencies using magnetostatic waves," Circ. Syst. Signal Process., vol. 4, no. 1-2, pp. 115-35, 1985.

[16] M. A. G. Laso, T. Lopetegi, M. J. Erro, D. Benito, M. J. Garde, M. A. Muriel, M. Sorolla, and M. Guglielmi, "Chirped delay lines in microstrip technology," IEEE Microwave Compon. Lett., vol. 11, pp. 486-488, Dec. 2001.

[17] FCC, "Revision of part 15 of the commission's rules regarding ultra-wideband transmission," ET-Docket 98-153, First Rep., Order, Apr. 2002.

[18] R. J. Fontana, "Recent system applications of short-pulse ultra-wideband (UWB) technology," IEEE Trans. Microwave Theory Tech., vol. 52, no. 9, pp. 2087-104, Sept. 2004.

[19] G. P. Hancke and B. Allen, "Ultrawideband as an industrial wireless solution," IEEE Pervasive Comput., vol. 5, no. 4, pp. 78-85, Oct/Dec. 2006.

[20] X. Gu and L. Taylor, "Ultra-wideband and its capabilities," BT Technol. J., vol. 21, no. 3, pp. 56-66, July 2003.

[21] I. Gresham *et al.*, "Ultra-wideband radar sensors for short-range vehicular applications," IEEE Trans. Microwave Theory Tech., vol. 52, no. 9, pp. 2105-2122, Sept. 2004.

[22] E. M. Staderini, "UWB radars in medicine," IEEE Aerosp. Electron. Syst. Mag., vol. 17, no. 1, pp. 13-18, Jan. 2002

[23] R. J. Fontana and S. J. Gunderson, "Ultra-wideband precision asset location system," IEEE Conf. Ultra Wideband Systems and Tech., pp. 147-50, May 2002.

[24] B. H. Kolner, "Space-time duality and the theory of temporal imaging," IEEE J. Quantum Electron., vol. 30, pp. 1951-1963, Aug. 1994.

[25] P. Tortoli and F. Andre, "Chirp Fourier transform based on a single SAW filter," Electron. Lett., vol. 22, no. 19, pp. 1017-19, Sept. 1986.

[26] M. A. Muriel, J. Azaña and A. Carballar, "Real-time Fourier transformer based on fiber gratings," Optics Lett., vol. 24, no. 1, pp. 1-3, Jan. 1999.

[27] H. J. Visser, *Array and Phased Array Antenna Basics*, Chichester: Wiley, 2005.

[28] B. M. Horton, "Noise-modulated distance measuring systems," Inst. Radio Engineers – Proc., vol. 47, no. 5, pp. 821-8, May 1959.

[29] L. Zhou, A. Safarian, and P. Heydari, "A CMOS analogue delay stage," Electron. Lett., vol. 42, no. 21, pp. 1213-15, Oct. 2006.

[30] D. Borg and D. B. Hunter, "Tunable microwave photonic passive delay line based on multichannel fibre grating matrix," Electron. Lett., vol. 41, no. 9, pp. 537-8, Apr. 2005.

[31] D. Petri and S. Rapuano, "Introduction to special issue on ADC modeling and testing," Comput. Stand. Interfaces, vol. 29, no. 1, pp. 3-4, Jan. 2007.

[32] B. Le, T. W. Rondeau, J. H. Reed and C. W. Bostian, "Analog-to-digital converters," IEEE Signal Process. Mag., vol. 22, no. 6, pp. 69-77, Nov. 2005.

[33] H.-J. Lee, D. S. Ha and H.-S. Lee, "Towards digital UWB radios: part I – frequency domain UWB receiver with 1 bit ADCs," Int. Workshop Ultra Wideband Syst. Joint Syst. Ultra Wideband Syst. Technol. (Joint UWBST IWUWBS), pp. 248-52, May 2004.

[34] Y. Han and B. Jalali, "Photonic time-stretched analog-to-digital converter: fundamental concepts and practical considerations," J. Lightwave Technol., vol. 21, no. 12, pp. 3085-103, Dec. 2003.

[35] G. C. Valley, G. A. Sefler, J. Chou and B. Jalali, "Continuous realization of time-stretch ADC," Int. Top. Meet. Microwave Photon., pp. 271-3, Oct. 2006.

[36] B. Allen, S. A. Ghorashi, and M. Ghavami, "A review of pulse design for impulse radio," IEE Conf. Publ., pp.93-7, Jul. 2004.

[37] J. A. Nay da Silva, M. L. R. de Campos, "Spectrally efficient UWB pulse shaping with application in orthogonal PSM," IEEE Trans. Commun., vol. 55, no. 2, pp. 313-22, Feb. 2007.

[38] I. S. Lin, J. D. McKinney and A. M. Weiner, "Photonic synthesis of broadband microwave arbitrary waveforms applicable to ultra-wideband communication," IEEE Microwave Compon. Lett., vol. 11, no. 4, pp. 486-8, Apr. 2005.

[39] J. Azaña, N. K. Berger, L. Boris and B. Fischer, "Broadband arbitrary waveform generation based on microwave frequency upshifting in optical fibers," J. Lightwave Technol., vol. 24, no. 7, Jul. 2006.

[40] I. Arnedo, M. A. G. Laso, F. Falcone, D. Benito and T. Lopetegi, "A series solution for the single mode synthesis problem based on the coupled mode theory," accepted for publication, IEEE Trans. Microw. Theory Tech., 2008.

[41] J. Schwartz, J. Azaña and D. V. Plant, "Real-time microwave signal processing using microstrip technology," IEEE MTT-S Int. Microwave Symp. Dig., San Francisco, CA, pp. 1991-4, Jun. 2006.

[42] J. Schwartz, J. Azaña and D. V. Plant, "Experimental demonstration of real-time spectrum analysis using dispersive microstrip," IEEE Microwave Compon. Lett., vol. 16, n. 4, pp. 215-217, Apr. 2006.

[43] J. Schwartz, J. Azaña and D. V. Plant, "Design of a tunable UWB delay-line with nanosecond excursions using chirped electromagnetic bandgap structures," Proc. 4th IASTED Int. Conf. Antennas, Radar and Wave Propagation, paper #566-814, Montréal, Canada, May 2007.

[44] J. Schwartz, I. Arnedo, M. A. G. Laso, T. Lopetegi, J. Azaña and D. V. Plant, "An electronic UWB continuously tunable time-delay system with nanosecond delays," submitted to IEEE Microwave Compon. Lett., Jul. 2007.

[45] J. Schwartz, J. Azaña and D. V. Plant, "An electronic temporal imaging system for compression and reversal of arbitrary UWB waveforms," submitted to IEEE Radio & Wireless Symp. (RWS 2008), Orlando, FL, Jan. 2008.

[46] J. Schwartz, J. Azaña and D. V. Plant, "A fully-electronic time-stretch system," **Best Student Paper**, 12th Int. Symp. Antenna Technology and Applied Electromagnetics (ANTEM/URSI), pp. 119-22, Jul. 2006.

[47] J. Schwartz, J. Azaña and D. V. Plant, "A fully-electronic system for the time magnification of GHz electrical signals," IEEE Trans. Microwave Theory Tech., v.55, n.2, pp. 327-334, Feb. 2007.

[48] J. Schwartz, Michael M. Guttman, J. Azaña and D. V. Plant, "Multi-Channel Filters Using Chirped Bandgap Structures in Microstrip Technology," IEEE Microwave Compon. Lett., v. 17, no. 8, pp. 577-9, Aug. 2007.

[49] J. Schwartz, M. Guttman, J. Azaña and D. V. Plant, "A multiple-frequency resonator in microstrip technology," 12th Int. Symp. Antenna Technol. and Appl. Electromagnetics (ANTEM/URSI), pp. 569-72, Jul. 2006.

CHAPTER 2

Chirped Electromagnetic Bandgap Structures

In this chapter, we review the key developments that have brought bandgap structures from the domain of photonics towards practical integrated microwave structures. We introduce and situate the concept of a CEBG structure and outline our general design procedure for the works produced in this thesis. We also detail our first prototype CEBG structure and describe its application as a passive mechanism for real-time Fourier transformation.

2.1 Review of the Literature

2.1.1 Electromagnetic Bandgap Structures

The origin of EBG structures is linked directly to the domain of photonics[1], where it has long been well-understood that a spatially periodic perturbation (period 'Λ') of the refractive index n of a material supporting a traveling electromagnetic wave will strongly inhibit the propagation of a wavelength λ_B complicit with the Bragg condition (assuming normal incidence as illustrated in Fig. 2.1) [1]:

$$\Lambda = \frac{\lambda_B}{2n} \tag{2.1}$$

The 'bandgap' terminology originates from the study of semiconductor crystals where it described forbidden electron energy states, and has been adopted to describe a range of wavelengths in which wave propagation is inhibited by a periodic lattice or layer-stack, while wavelengths outside the gap (excepting harmonics) remain essentially transparent to it (Fig. 2.1).

[1] For this reason it is still common to hear them described as photonic bandgap or "PBG" structures, even though the fundamental concept applies more generally to electromagnetic waves of any type.

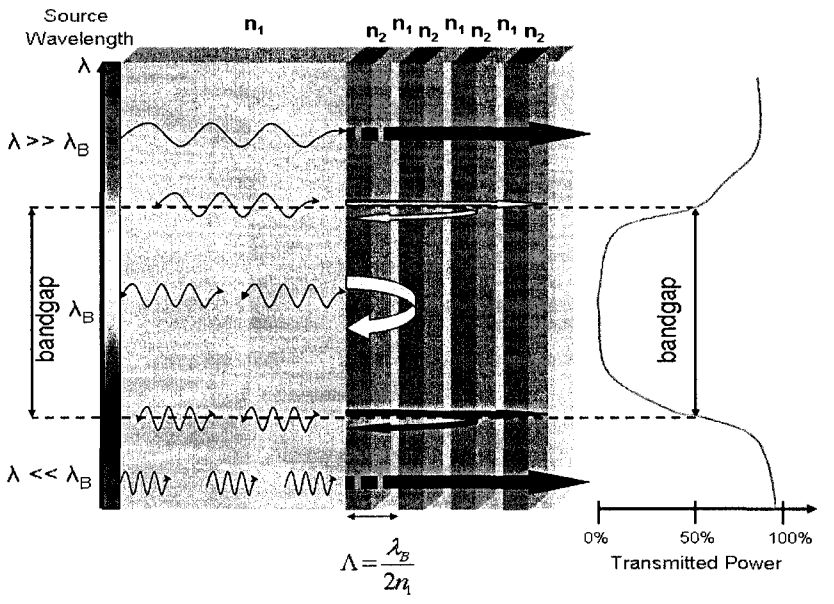

Fig. 2.1. Illustration of Bragg reflection and bandgap behavior for normal-incidence optical waves.

This phenomenon was first explored in solid-state periodic dielectric structures [2] and (since Maxwell's equations can be scaled) the concept was adapted from optical frequencies to yield electronic microwave and mm-wave structures with only a few important distinctions from their optical counterparts aside from the change in the charge carrier. One such distinction is that practical periodic microwave structures have a drastically reduced number of periods; a microstrip EBG might have only a few periods, while FBGs frequently have periods numbering in the ten thousands. This is of necessity due to size constraints: for example, a 10 GHz signal in a substrate (ε_r = 3.0) has a wavelength of about 1 cm, such that a periodic EBG would have to span several cm to be an effective reflector, making it "large" by electronics standards. However, even with relatively few periods, the reflectivities of EBG structures remain comparable to those of FBGs because they use strong impedance modulations[2] (e.g. ±10%), whereas the modulation of the refractive index in most fiber gratings is usually extremely slight (e.g. ±0.005%).

[2] When implementing a metallo-dielectric EBG structure, the modulation is described in terms of the characteristic impedance Z_o, generally about some standard value like 50 Ω, rather than the index of refraction as in optical structures. Refraction index and impedance are related through the concept of permittivity ε.

When it was recognized that bandgap structures could provide broader stop-bands in transmission line than traditional tuned-stub approaches, metallo-dielectric implementations of EBG structures emerged in 1-D, 2-D planar and 3-D configurations for a number of applications, including: suppressing undesired radiation in antennas [3]-[7], harmonic tuning in power amplifiers [8], ultra-broadband filtering [9], spurious passband suppression in coupled-line bandpass filters and periodically-loaded waveguides [10]-[12], improving the conversion efficiency of mm-wave frequency multipliers [13], and as a component beneath high-speed circuits to suppress parallel-plate noise [14].

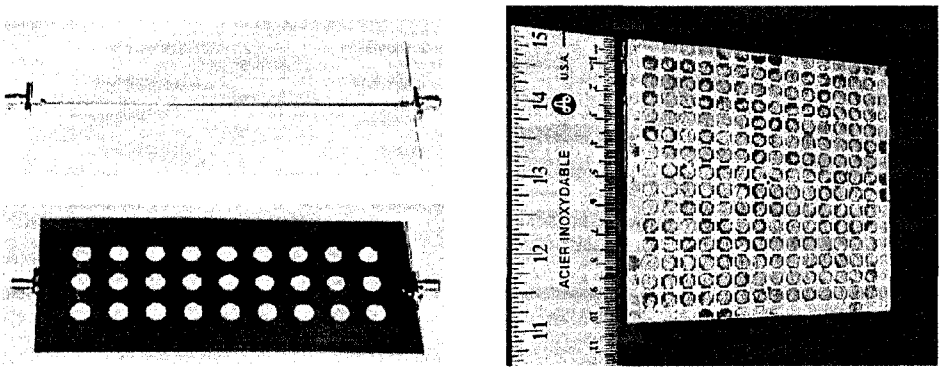

Fig. 2.2 Metallo-dielectric EBG structures. (Left) Microstrip with ground-plane EBG using etched circles (bottom: ground plane, top: center conductor), (right) ground plane of a 2-layer board used to demonstrate parallel-plate noise suppression in [14].

Microstrip lines, which support quasi-TEM modes in which some field components exist in air, are a desirable target technology for EBGs due to the ease with which they are designed, fabricated and integrated with other components on a printed circuit board (PCB). The first implementations of an EBG in a microstrip transmission line were carried out by drilling a pattern of micro-machined holes in the substrate [15], and thereafter the preferred method of simply etching circular holes in the conductive ground plane emerged (Fig. 2.3, left) [16], yielding deeper and wider stopbands than drilling methods and being much more well-suited to monolithic integration practices. Ground-plane etching does not occupy area on a main signal layer and can be introduced beneath existing circuits, including other filter structures [17].

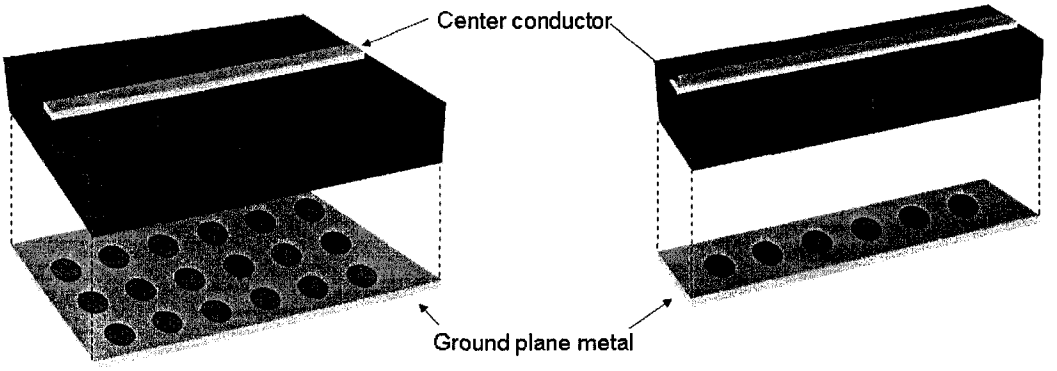

Fig. 2.3 Representations of microstrip EBGs created by etching the ground plane in 2-D or 1-D.

A large body of work developing EBGs was established predominantly by one group of researchers (Sorolla *et al.*, as summarized in [18]) beginning with the realization that EBG structures could be made effectively 1-D in microstrip with virtually no drop in effectiveness due to strong field confinement (Fig. 2.3, right) [19] and could be designed effectively using the established models for the design of optical FBGs [20]-[23]. Coupled mode theory [24] is a powerful tool for synthesizing reflective geometries in this instance – it describes how the coupling coefficient[3] $\kappa(z)$ is tied to the physical geometry of the line along the z-axis. For a TEM-type transmission-line of characteristic impedance $Z_o(z)$, a few simple approximations lead to [23]:

$$\kappa(z) = -\frac{1}{2 \cdot Z_O(z)} \cdot \frac{dZ_O(z)}{dz} \tag{2.2}$$

The coupling coefficient is directly tied to the frequency-response of any periodic structure. The relationship between physical geometry and frequency-response can be developed to yield effective synthesis techniques for EBG structures [25].

Research into optimizing EBG performance began with the addition of a tapering (apodization) window applied to the dimensions of the patterned circles (Fig. 2.4, left) [26]. The effect of tapering is to reduce the sidelobe levels in the frequency-response by suppressing undesirable long-path resonances of the Fabry-Perot type which arise from abrupt local impedance changes. In general,

[3] Coupling in this instance is restricted to the co- and counter-propagating fundamental modes (quasi-TEM) of the microstrip.

adding a tapering window will smooth the frequency response at the expense of diminishing the effective reflection bandwidth –unless more periods are added by making the structure longer to compensate. Detailed studies of the effect of various tapering functions on sidelobe levels, rejection, bandwidth and smoothness are presented in [27] and [28] which suggest that Kaiser windows are most effective at reducing sidelobe levels but require the greatest length compensation to preserve the bandwidth, whereas Gaussian windows require very little extra length to re-establish the 3-dB bandwidth and rejection level, but are not as effective at reducing sidelobe levels.

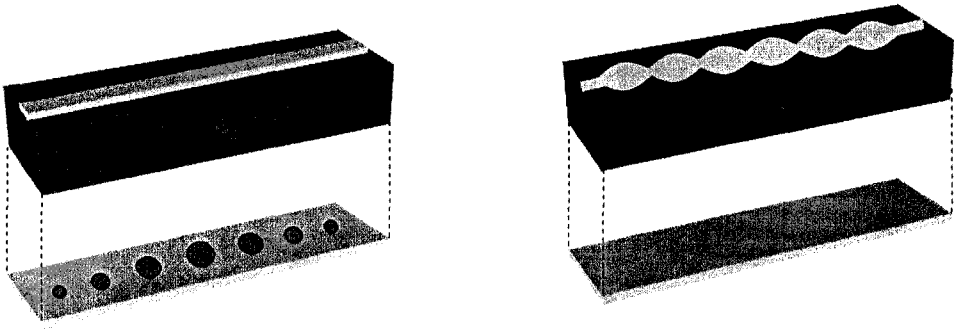

Fig. 2.4 Improved microstrip EBGs illustrating tapering (left) and center-strip modulation (right).

It was shown that microstrip EBGs could be made more compact through meandering geometries with minimal radiation and scattering loss effects [29], [30]. Instead of using discrete ground-plane circles, a more continuous "network-topology" geometry was then proposed whereby sinusoidal patterns were employed to form a distributed impedance perturbation [31], [32] which could also be implemented in the center strip conductor rather than the ground plane by varying the width of the strip directly [31] (Fig. 2.4, right), permitting two-sided EBG patterning (although sinusoidal microstrips had been investigated much earlier [33], the theoretical tools of the time were limited to step-impedance analysis and there was little insight into bandgap-design). Frequency-tunable EBGs have also been implemented by periodically loading the line with varactor diodes and applying control voltages [34].

Several superstructure concepts from optical FBGs migrated quickly down to microwave frequencies for application with EBGs (although there is at least one

instance of ideas flowing the other way - it has been suggested that microwave EBGs could make excellent and cost-effective prototypes for FBGs by scaling the frequency response [35]). Some ideas translated from the photonic regime include: cascading identical EBGs (leaving an unmodulated gap or 'defect' between them) to create a defect-resonator in microstrip or coplanar waveguide [36], [37] or a line-defect waveguide on a PCB [38]; and cascading two different-frequency EBGs to implement a bandpass filter between the two rejection stopbands [39]. It was subsequently demonstrated that with network-topology (continuous) EBGs the principle of superposition could be applied to co-locate two different EBGs in the same length of microstrip [40]. We will return to both defect-resonator and superimposed structures in Chapter 5.

2.1.2 The Chirped EBG (CEBG)

Prior to the introduction of chirp, most of the targeted applications of EBG structures were concerned with their amplitude response [3]-[13] with far less research interest being generated by their phase characteristics, which were shown to exhibit the same characteristic behaviors as optical FBGs: namely, a narrowband region of high dispersion near the band-edge and the (strictly theoretical) curiosity of exhibiting a "superluminal" phase velocity in the forbidden bandgap [41]. By contrast, a CEBG is a structure designed to achieve a particular dispersion for the reflected signal in its entire bandgap region.

We must first define our terms as regards discussion of dispersion. We will restrict our discussion to structures designed to introduce first-order dispersion, which can be described mathematically as the imparting on a signal of a quadratic-phase (linear-frequency) characteristic in the frequency domain.

In considering the S-parameters characterizing the frequency response of a 2-port structure (such as a transmission line), the S_{11} response effectively describes the reflective behavior at the input port versus frequency, and consists of a magnitude $|S_{11}(\omega)|$ and a phase term $\theta(\omega)$. We define the group delay $\tau_g(\omega)$ and its derivative $\Phi(\omega)$:

$$\tau_g(\omega) = -\frac{d\theta(\omega)}{d\omega} \qquad \Phi(\omega) = -\frac{d^2\theta(\omega)}{d\omega^2} \tag{2.3}$$

Here, $\Phi(\omega)$ represents the rate of change of group delay with respect to frequency. As we restrict discussion to treating first-order dispersion and therefore structures exhibiting linear group delay ($\Phi(\omega) \rightarrow \Phi$), and to facilitate a discussion of frequencies in Hertz, we will frequently make reference to the group delay slope: $\sigma = 2\pi\Phi$ in units of s/Hz. This metric permits easy and intuitive understanding in the frequency vs. time plotting we will favor.

A linearly-chirped EBG can be created by linearly varying the perturbation period Λ as $\Lambda(z)$ along the length of line, resulting in a continuum of spatially distributed "local bandgaps": each location along the line corresponds to a uniquely reflecting Bragg wavelength. The result is a reflection-mode first-order dispersion in which each frequency travels a different distance down the line before reflecting.

The first demonstration of a 1-D microstrip structure with such a non-uniform periodicity was implemented using ground-plane circle-etching [42] and subsequently in a network-topology using chirped sinusoidal modulation of the strip-width of the center conductor (Fig. 2.5) [43].

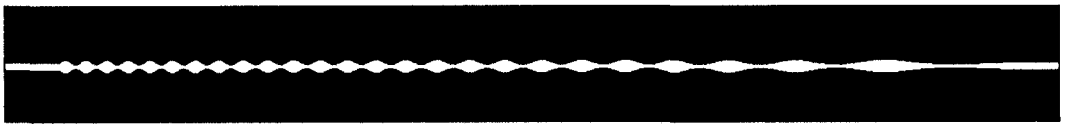

Fig. 2.5. Illustration of a network-topology linearly chirped EBG in microstrip line.

Focusing on the latter demonstration, we turn now to the empirical design formula for the modulated line impedance $Z_o(z)$ proposed in [43], and subsequently employed for most of the designs in this work:

$$Z_o(z) = 50 \cdot \exp\left[A \cdot W(z) \cdot \sin\left(\frac{2\pi \cdot z}{a_o} + C \cdot z^2 - C \cdot \left(\frac{L}{2} \right)^2 \right) \right] \tag{2.4}$$

We must now dedicate some space to provide insight into (2.4). The general form of the expression (that of an exponentially-raised sinusoid) can be understood in reference to the coupling-coefficient equation (2.2): it is chosen to yield a purely

sinusoidal κ(z), which minimizes the presence of higher harmonics of the main resonant Bragg frequency in the spectral response in accordance with the coupled-mode theory [23]. The modulated section of line is of length '*L*' from $z = -L/2$ to $z = +L/2$, beyond which a 50-Ω line termination is assumed. The period 'a_o' corresponds to the angular frequency ω_o at the midpoint along the line (z = 0), according to:

$$a_o = \frac{c \cdot \pi}{\omega_o \cdot \sqrt{\varepsilon_{eff}}} \tag{2.5}$$

where ε_{eff} is the effective permittivity of the transmission line. Typically, *L* should be made an integer multiple of a_o to guarantee that the line terminates at $z = \pm L/2$ with 50-Ω impedance, thus preventing a local step-discontinuity at the endpoints (note that the added constant term $-C(L/2)^2$ in the sinusoid ensures this proper matching at the ends of the line). It should be noted that since EBG designs can be made well into the GHz range, we have found that using a low-frequency effective permittivity ε_{eff_DC} for microstrip as in [43] is not always suitable in light of material dispersion. In this work, we employ the Kirschning-Jansen formula [44] to determine a dispersion-compensated design value for ε_{eff} at the center design frequency ω_o based on a comparative study of dispersion formulae [45] and the moderate-valued substrate permittivities of our designs.

Continuing to detail (2.4), the chirp parameter '*C*' (m^{-2}) is a scalar chosen such that the locally reflected angular frequency (Bragg resonance) along the length of the line occurs linearly in *z* and can be described by [43]:

$$\omega_{refl}(z) = \frac{c}{2 \cdot \sqrt{\varepsilon_{eff}}} \cdot \left(\frac{2\pi}{a_o} + 2Cz\right) \tag{2.6}$$

The chirp parameter dictates the amount of dispersion introduced by the line and is related directly to the linear group delay slope σ (s/Hz) according to:

$$\sigma = \frac{4\pi\varepsilon_{eff}}{C \cdot c^2} \tag{2.7}$$

The chirp is intimately related with the ultimate bandwidth and length of the final device – a higher, "faster" chirp parameter will, for a fixed length *L*, yield a device covering a broader bandwidth defined as $|\omega(-L/2)-\omega(L/2)|$ or, equivalently:

$$\Delta\omega = \frac{c \cdot |C| \cdot L}{\sqrt{\varepsilon_{eff}}} \tag{2.8}$$

The realized 3-dB bandwidth of the lines may be greater or smaller than this value, depending on tapering and modulation depth applied in (2.4) as described below. There exists a natural limit in selecting large chirp values (and therefore large bandwidths) assuming a fixed device length, since increasing the magnitude of the chirp will reduce the number of realized periodic perturbations for each frequency point, ergo reducing the reflectivity (by way of the coupling coefficient). Chirp can be made to be positively (up-chirp) or negatively (down-chirp) valued. Most of the designs in this work feature negative chirp values – this is desirable in lossy substrates, since it results in higher (and, by extension, lossier) frequencies to reflect first before they can significantly attenuate in the microstrip[4]. For the same reason, a negative chirp can also reduce mode-dispersion effects.

The windowing function W(z) in (2.4) describes the apodization of the structure and determines, along with the scalar modifier '*A*', the depth of the impedance modulation along the line. The choice of these parameters influences both the final 3-dB bandwidth of the bandgap structure as well as the sidelobe levels and group-delay ripple. In figures 2.6-2.7, we present simulation results obtained with Agilent's "method of moments" solver *Momentum* (see section 2.2.1) for a CEBG having the following parameters: L = 94 mm, substrate ε_r = 9.41, substrate height = 1.27mm, a_o = L/22 = 4.27 mm, ω_o = 12.9 GHz, ε_{eff} = 7.357, C = -2000m^{-2}. We employ a Gaussian windowing function as follows:

$$W(z) = e^{-G(\frac{z-a}{L})^2} \qquad -\frac{L}{2} \le z \le +\frac{L}{2} \tag{2.9}$$

where '*G*' controls the 'abruptness' of the window, and the '*a*' parameter is introduced to create asymmetry (this practice is useful to help support with greater reflectivities those frequencies towards the rear of the line, which have undergone more round-trip losses). We simulate with *Momentum* the frequency response of a

[4] Recall that both dielectric and conductor losses in a typical transmission line mode increase with frequency, although in these ranges the conductor losses are generally more important.

structure designed by equation (2.4) using A = 0.14 and beginning with a symmetric (a = 0) window having different window abruptness G = [0, 3, 6], serving to illustrate the effect of the tapering window on the frequency response. As shown in Fig. 2.6, apodization improves the linearity of the group delay and reduces the sidelobe levels of the S_{11} response at the expense of the 3-dB bandwidth. In Fig. 2.7, we remove the Gaussian window entirely (G = 0) and vary the '*A*' parameter (depth of modulation), which can also be used to smooth the group-delay response but at the expense of decreasing the reflectivity of the overall structure.

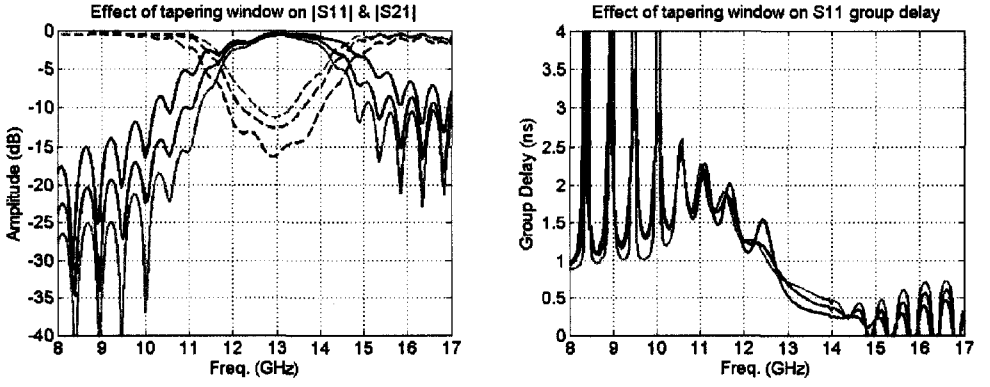

Fig. 2.6. Effect of adding a Gaussian apodization window on |S11| (left, solid), |S21| (left, dash) and group delay (right) in a CEBG. Traces are for G=0 (blue), G=3 (green) and G=6 (red).

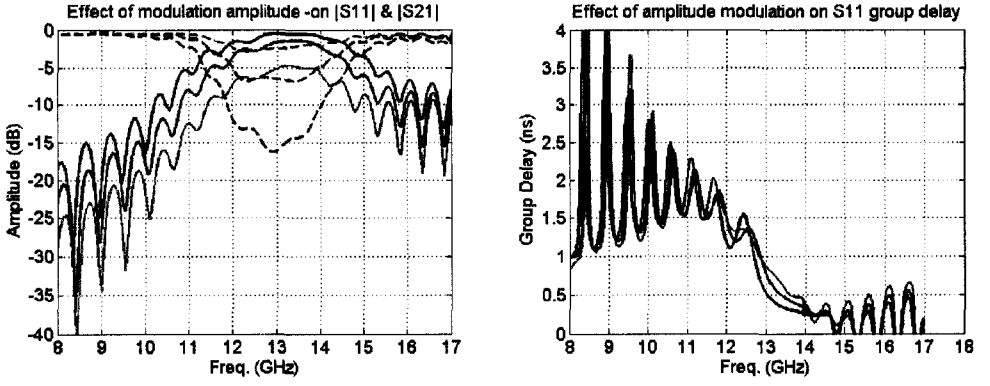

Fig. 2.7. Effect of changing the depth of modulation on |S11| (left, solid), |S21| (left, dash) and group delay (right) in a CEBG. Traces are for A=0.14 (blue), A=0.09 (green) and A=0.05 (red), which represent impedance modulations (about 50 Ω) of 15%, 9.4% and 5.1%, respectively.

Once the impedance modulation $Z_o(z)$ is established using (2.4), creating an actual microstrip is a matter of using traditional microstrip synthesis equations [46] which, for width '*w(z)*' to substrate thickness '*t*' ratios of less than 2, is:

$$w(z) = \frac{8te^B}{e^{2B}-2}\ ;\ B = \frac{Z_o(z)}{60}\sqrt{\frac{\varepsilon_r+1}{2}} + \frac{\varepsilon_r-1}{\varepsilon_r+1}\left(0.23+\frac{0.11}{\varepsilon_r}\right);\quad \frac{w(z)}{t} < 2 \qquad (2.10)$$

It is worth noting that when varying the strip-width one must ensure that the width never exceeds the region in which the synthesis equation is valid, and furthermore, does not become wide enough to potentially excite undesirable lateral modes. Also, while these equations suggest a fundamentally empirical design strategy, more rigorous synthesis equations are presently in development which can also be used to produce chirped EBGs with potentially optimized responses [25].

2.2 Methodology & Prototype Design

2.2.1 Simulation Tools

Simulations in this work were generally carried out using Agilent's *Momentum* software, which uses a "method of moments" (MoM) procedure to solve 2.5-D field problems (i.e. those consisting only of plane-layer stacks and vias). The MoM is a discretization process designed to break a complex surface down into a mesh of simpler geometries in order to produce and solve a matrix of equations for unknown surface currents under a chosen field excitation [47]. It is widely known to be faster than the more rigorous full-3D field solvers, such as Ansoft's *HFSS* (which was also trialed for our purposes). Despite this, simulation was occasionally a limiting factor in this work – meshing structures at high frequencies yields a prohibitive number of unknowns, and as a result long structures with frequencies above 20 GHz were generally avoided due to excessive simulation times and computer memory demands.

2.2.2 Fabrication

A prototype board (Fig. 2.8, left) was fabricated on a 96% alumina substrate supplied by Coorstek (1.27mm-thick ADS-96R, $\varepsilon_r = 9.41$ & $\tan\delta = 7\text{x}10^{-4}$ at 10

GHz) and fully metallized on the back face with a gold-alloy while the top was etched with three traces – a 50-Ω line, a single-frequency EBG tuned to 6 GHz and a CEBG covering the range of 4 to 8 GHz. The CEBG structure was designed using (2.4) and (2.10) with A = 0.4, L = 9.22 cm, a_o = 9.22 mm, C = -2600 m^{-2} (for a group delay slope of σ = -0.366 ns/GHz using a frequency-corrected ε_{eff} of 6.81) and a Gaussian window. The boards were mounted on customized aluminum baseplates using conductive epoxy and edge-connectorized by soldering to sub-miniature 'A' (SMA) connectors.

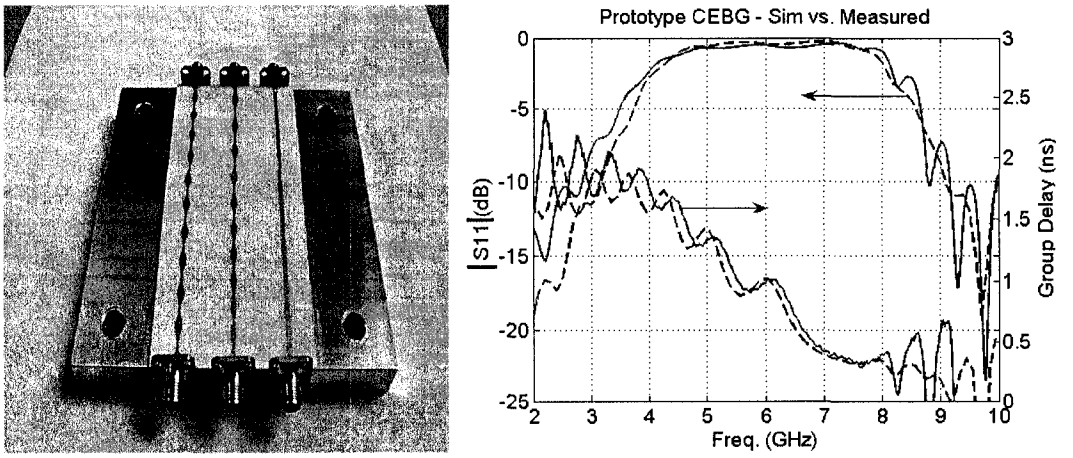

Fig. 2.8. (Left) Photograph of the prototype board with three traces – the center trace is the CEBG. (Right) Simulated (dash) and measured (solid) data for the prototype, indicating $|S_{11}|$ (left axis) and group delay (right axis) data which closely correlate.

2.2.3 Characterization

Finished designs were characterized using vector network analysis (VNA) equipment (Agilent's 20 GHz model 8720ES) and the results compared to simulation (Fig. 2.8, right). When the group delay is linearized in the target bandgap region by using MatLAB, the slope obtained is approximately -0.381 ns/GHz in the bandgap region, which (if one goes by the -3-dB points) exists between 3.8 GHz and 8.2 GHz. Group delay compares favorably to the simulation target with the expected level of ripple present due to long-path resonances. The insertion loss[5] of the device is measured at about 0.5 dB in the bandgap region

[5] In this work, since we are dealing with reflection-mode devices, the term "insertion loss" here takes on the meaning of accounting for all power that is not reflected, including transmission and resistive/radiative losses.

(although this does not include the external directional coupler which will be necessary to operate the device).

2.3 Real-Time Fourier Transformation

2.3.1 Background and Application

As discussed in section 1.1.2, spectral analysis techniques built for measuring repetitive signal inputs can become inadequate when it comes to measuring time-varying signals with instantaneous bandwidths in the GHz range. For this, one requires a real-time system in which the signal can be observed on a single-shot basis. This can be achieved by directly mapping a signal's frequency content into the time-domain in real-time – this is a real-time Fourier transformation (RTFT). This mapping operation is readily achieved by any filter having both the appropriate bandwidth and a sufficiently steep linear group delay slope to temporally order the frequency components of a signal. RTFT has been a familiar application zone for chirped SAW devices for some time [48], [49] with typical SAW-based RTFTs easily reaching bandwidths of hundreds of MHz [50] but having to resort to complex sub-micron fabrication techniques when reaching into the GHz range [51]. Chirped SAW devices also tend to have extremely high insertion losses, sometimes exceeding 25 dB [52], and do not have the capacity for smoothly varying impedance changes, being limited to one impedance step per half-wavelength, which has the effect of limiting their fractional bandwidth as well due to undesirable harmonic responses. Therefore, a niche frequency range exists for which the dispersive CEBG is well-suited.

The mechanism behind RTFT can be understood according to the well-documented duality between the concepts of spatial diffraction and temporal dispersion, which are governed by a similar set of parabolic differential equations [53], [54] resulting from a set of approximations to the general wave equation. In the spatial case of Fourier imaging, it is assumed that one has (i) a monochromatic beam that is (ii) initially paraxially-confined. In the temporal case, the assumptions require (i) a plane-wave ("monochromatic" in a spatial sense) that is (ii) spectrally-confined (band-limited); these sets of assumptions are

complementary [54]. The theory suggests that a sufficiently dispersive element can perform an RTFT on a time-windowed input signal in much the same manner as sufficient diffraction makes possible a spatial far-field Fourier image of a space-aperture 'Δx' a distance 'd' away, as illustrated in Fig. 2.9. The time-window of the signal to be transformed must satisfy (corrected with the author's approval from [55], where a factor of 2 was accidentally omitted by the author):

$$\left|\frac{\Delta t^2}{4\sigma}\right| << 1 \tag{2.11}$$

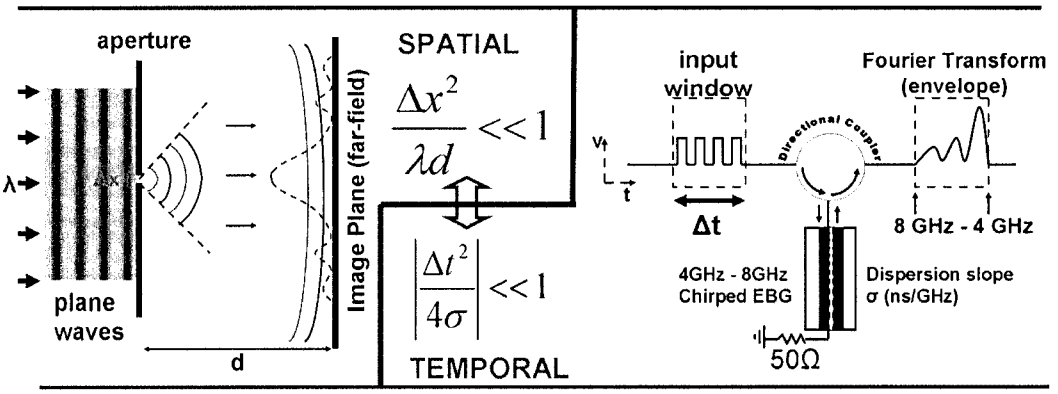

Fig. 2.9. Representation of space-time duality in Fourier imaging (spatial and temporal domains)

If satisfied, there is sufficiently strong dispersion such that each time-point in the dispersed signal is associated with only one frequency, and it can be shown [55] that for the time-windowed input signal $s_i(t)$ convolved with the dispersive device response, the output $s_o(t)$ is proportional to the Fourier transform (FT) of the input, scaled into the time domain:

$$s_o(t) \propto \left|FT(s_i(t))\right|_{\omega=\frac{2\pi \cdot t}{\sigma}} \tag{2.12}$$

Only the magnitude can be recovered from the technique presented here (the output is phase-modulated by the CEBG), and it must be extracted from the envelope of the output signal (which is effectively a chirped signal). The frequency resolution of such an RTFT device can be approximated as the square root of the ratio of CEBG bandwidth to its total delay range [56], thus if the bandwidth must remain fixed and the resolution improved, a device must either be made longer or 'slower' (i.e. by raising the permittivity).

2.3.2 Demonstration

The use of CEBG structures as passive RTFT tools was first proposed by Laso *et al.* [56], in which several simulations were presented to support the idea and a prototype was manufactured and characterized, although no direct RTFTs were observed experimentally. To completely demonstrate this idea, we applied a test signal which contained frequency content in the 4-8 GHz bandgap of our fabricated CEBG prototype [57], [58]. According to (2.11), a time-window of $\Delta t << 1.2$ ns satisfies the requirement for RTFT, although this restriction can be relaxed somewhat [55] and a time-window of ~0.6 ns was deemed appropriate.

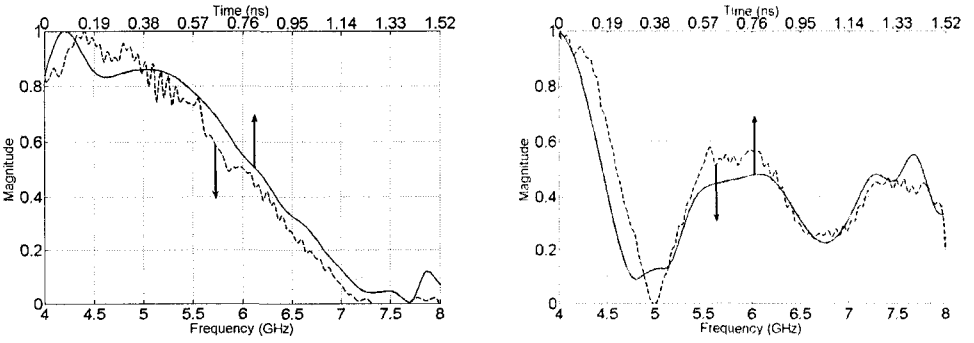

Fig. 2.10. RTFT Example #1 - The spectra of 6-bit signals '010100' (left) and '100111' (right) as measured using a spectrum analyzer (dashed, frequency domain) and a CEBG microstrip (solid, time-domain). Results have been normalized in magnitude for clarity.

At first, digital bit-signaling[6] was chosen using a 12.5 Gbps Anritsu Pulse Pattern Generator (MP163B) to produce a pattern of 6 bits within the required time-window. The dispersed signals, of about 1.5 ns in length, contained only a few periods of signal content (a 4 – 8 GHz chirped signal) from which an envelope was extracted using interpolation in MatLAB[7]. The results are presented in Fig. 2.10, in which the time-domain envelopes are compared directly to measurements taken with a spectrum analyzer (Anritsu's MS2668C). Even with

[6] The RTFT process is not limited to digital signals, but they were convenient for two reasons: (i) time-gating was simple to implement using long strings of zeros, and (ii) it was complicit with the limited system bandwidth and resolution.

[7] Such interpolation can be seen as a non-real-time "cheat", but in actual practice the advised procedure would be to perform peak-detection using a simple RC network, or else down-conversion mixing using an appropriate linear frequency sweep to recover the envelope in real-time.

poor system resolution (our design does not easily resolve elements spaced closer than 1 GHz), it can clearly be seen that the recovered temporal waveform closely follows the frequency content of the signal.

Later measurements were taken using a longer CEBG design at somewhat higher frequencies (for an application in Chapter 3). This design was a meandered microstrip of 22 cm (see photo in Fig. 3.8) with a 3-dB measured bandwidth between 8 and 16 GHz and an approximately linear group delay slope of σ = -0.393 ns/GHz. We chose to test this line's RTFT response with a customized 4-GHz-bandwidth pulse generated using a conventional impulse generator (the Picosecond Pulse Labs 3600D, which produces a periodic train of -7.5V, 70 ps impulses), and an EBG synthesis algorithm [25] which creates an EBG microstrip for a target impulse response[8]. The result was a pulse of about 0.6 ns occupying the frequency band between 3 and 7 GHz (Fig. 2.11), which we then upconverted by difference-frequency mixing (using a commercial, triple-balanced diode mixer) with a tunable local oscillator (LO) to produce a broadband signal falling within the bandgap of the CEBG design. In Fig. 2.12, we compare the (normalized) signal envelope as obtained in the time-domain (using the envelope function of the oscilloscope) with what a conventional spectrum analyzer yields (the response of the analyzer in the figure is consistent with the fact that this was a periodic input). As we tune the LO and vary the frequency content, it can be seen that there is a corresponding time-shift in the RTFT.

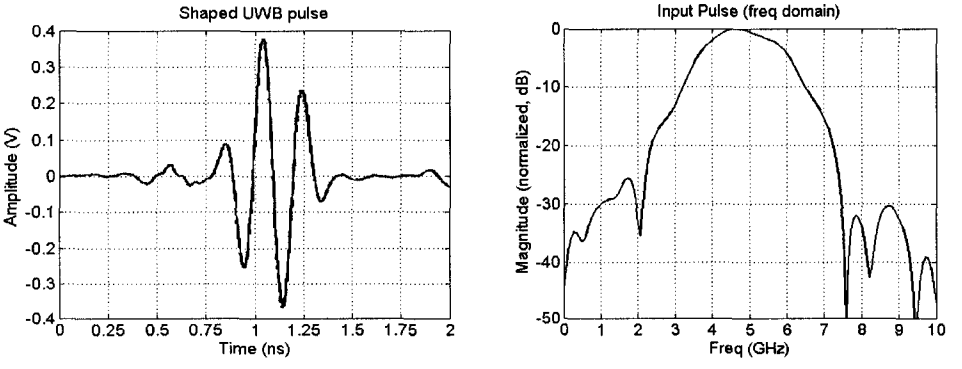

Fig. 2.11. (Left) A synthesized pulse used to demonstrate RTFT. This pulse was then mixed (up-conversion) to situate its response in the bandgap of an 8-16 GHz CEBG. (Right) The frequency content of the pulse obtained using MatLAB.

[8] In collaboration with I. Arnedo *et al.*

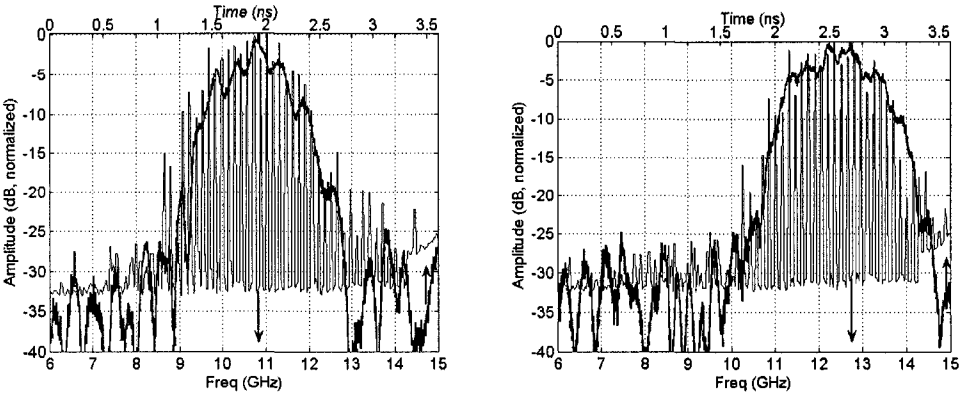

Fig. 2.12. RTFT example #2 – RTFT of a 4-GHz bandwidth signal (Fig. 2.11), upconverted using an LO of 15.5 GHz (left) and 17.2 GHz (right). The difference-frequency product is presented. Time domain measurements (top axis, darker trace) of a CEBG-based RTFT using an oscilloscope's envelope-detection function are compared to actual spectrum analyzer results (bottom axis, lighter trace).

2.3.3 Conclusions

In this chapter we reviewed the development of bandgap structures in microstrip and discussed an empirical design procedure for the CEBG. A prototype was fabricated which served both to verify the accuracy of our simulations and measurement and also as a demonstrator unit for RTFT. We provided the first direct experimental demonstration of the RTFT capabilities of these structures as first proposed in [56].

Real-time processing for signals having bandwidths extending to 10 GHz and beyond remains a challenge for most commercial devices. The passive RTFT process shown here has the potential to be deployed in parallel (for a segmented, interleaved signal) to handle continuous-time operation as a spectrum analyzer, a facet which we hope to see explored further in future works and which we will return to in Chapter 6.

References

[1] G. Keiser, *Optical Fiber Communications*, McGraw-Hill, 2000.

[2] E. Yablonovitch, "Inhibited spontaneous emission in solid-state physics and electronics," Phys. Rev. Lett., vol. 58, no. 20, pp. 2059-62, May 1987.

[3] M. P. Kesler, J. G. Maloney, B. L. Shirley, "Antenna design with the use of photonic band-gap materials as all-dielectric planar reflectors," Microwave Opt. Technol. Lett., vol. 11, no. 4, pp. 169-74, March 1996.

[4] T. J. Ellis and G. M. Rebeiz, "MM-wave, tapered slot antennas on micromachined photonic bandgap dielectrics," IEEE Int. Microwave Symp. Dig., vol. 2, pp. 1157-60, June 1996.

[5] P. K. Kelly, L. Diaz, M. Piket-Mey and I. Rumsey, "Investigation of scan blindness mitigation using photonic bandgap structure in phased arrays," Proc. SPIE Int. Soc. Opt. Eng., San Diego, CA, pp.239-48, July 1998.

[6] R. Gonzalo, P. de Maagt and M. Sorolla, "Enhanced patch-antenna performance by suppressing surface waves using photonic-bandgap substrates," IEEE Trans. Microwave Theory Tech., vol. 47, no. 11, pp. 2131-8, Nov. 1999.

[7] A. Gonzalez, T. Lopetegi, M. A. G. Laso, F. Falcone and M. Sorolla, "Active antenna with intrinsic harmonic rejection by using a photonic crystal," Proc. 27th Int. Conf. Infrared and Millimeter Waves, San Diego, CA, pp. 353-4, Sept. 2002.

[8] V. Radisic, Y. Qian, R. Coccioli and T. Itoh, "Broad-band power amplifier using dielectric photonic bandgap structure," IEEE Microw. Guid. Wave Lett., vol. 8, no. 1, pp. 13-14, Jan 1998.

[9] I. Rumsey, M. Pikey-May and P. K. Kelly, "Photonic bandgap structures used as filters in microstrip circuits," IEEE Microw. Guid. Wave Lett., vol. 8, no. 10, pp. 336-8, Oct. 1998.

[10] T. Lopetegi, M. A. G. Laso, J. Hernández, M. Bacaicoa, D. Benito, M. J. Garde, M. Sorolla and M. Gugliemi, "New microstrip 'wiggly-line' filters with spurious passband suppression," IEEE Trans. Microw. Theory Tech., vol. 49, no. 9, pp. 1593-8, Sept. 2001.

[11] T. Lopetegi, M. A. G. Laso, F. Falcone, F. Martin, J. Bonache, J. Garcia, L. Pérez-Cuevas, M. Sorolla and M. Gugliemi, "Microstrip 'wiggly-line'

bandpass filters with multispurious rejection," IEEE Microwave Compon. Lett., vol. 14, no. 11, pp. 531-3, Nov. 2004.

[12] F. Martin, F. Falcone, J. Bonache, T. Lopetegi, M. A. G. Laso, M. Coderch and M. Sorolla, "Periodic-loaded sinusoidal patterned electromagnetic bandgap coplanar waveguides," Microwave Opt. Technol. Lett., vol. 36, no. 3, pp. 181-4, Feb. 2003.

[13] F. Martín, F. Falcone, J. Bonache, T. Lopetegi, M. A. G. Laso and M. Sorolla, "New PBG nonlinear distributed structures: application to the optimization of millimeter wave frequency multipliers," Proc. 27th Int. Conf. Infrared and Millimeter Waves, San Diego, CA, pp. 59-60, Sept. 2002.

[14] R. Abhari and G. Eleftheriades, "Metallo-dielectric electromagnetic bandgap structures for suppression and isolation of the parallel-plate noise in high-speed circuits," IEEE Trans. Microwave Theory Tech., vol. 51, no. 6, pp. 1629-1639, June 2003.

[15] Y. Qian, V. Radisic and T. Itoh, "Simulation and experiment of photonic band-gap structures for microstrip circuits," Proc. Asia-Pacific Microwave Conf., Hong Kong, pp. 585-8, Dec. 1997.

[16] V. Radisic, Y. Qian, R. Coccioli and T. Itoh, "Novel 2-D photonic bandgap structure for microstrip lines," IEEE Microwave Guid. Wave Lett., vol. 8, no. 2, pp. 69-71, Feb. 1998.

[17] T. Akalin, M. A. G. Laso, T. Lopetegi, O. Vanbéslen, M. Sorolla and D. Lippens, "PBG-type microstrip filters with one- and two-sided patterns," Microwave Opt. Technol. Lett., vol. 30, no. 1, pp. 69-72, July 2001.

[18] T. Lopetegi, M. A. G. Laso, R. Gonzalo, M. J. Erro, F. Falcone, D. Benito, M. J. Garde, P. de Maagt and M. Sorolla, "Electromagnetic crystals in microstrip technology," Optical and Quantum Electron., vol. 34, no. 1-3, pp. 279-95, Jan/Mar. 2002.

[19] F. Falcone, T. Lopetegi and M. Sorolla, "1-D and 2-D photonic bandgap microstrip structures," Microwave Opt. Technol. Lett., vol. 22, no. 6, pp. 411-2, Sept. 1999.

[20] M. A. G. Laso, M. J. Erro, D. Benito, M. J. Garde, T. Lopetegi, F. Falcone and M. Sorolla, "Analysis and design of 1-D photonic bandgap microstrip structures using a fiber grating model," Microwave Opt. Technol. Lett., Vol. 22, no. 4, pp. 223-6, Aug. 1999.

[21] M. J. Erro, M. A. G. Laso, D. Benito, M. J. Garde, T. Lopetegi, F. Falcone and M. Sorolla, "Extended model based on the coupled-mode theory in fiber gratings for the analysis and design of 1D photonic bandgap devices in microstrip technology," Proc. SPIE - THz and GHz Photonics, pp. 166-75, July 1999.

[22] M. J. Erro, M. A. G. Laso, T. Lopetegi, D. Benito, M. J. Garde and M. Sorolla, "Analysis and design of electromagnetic crystals in microstrip technology using a fibre grating model," Optical and Quantum Electron., vol. 34, no. 1-3, pp. 297-309, Jan/Mar. 2002.

[23] T. Lopetegi, M. A. G. Laso, M. J. Erro, M. Sorolla and M. Thumm, "Analysis and design of periodic structures for microstrip lines by using the coupled-mode theory," IEEE Microwave Compon. Lett., vol. 12, no. 11, pp. 441-3, Nov. 2002.

[24] E. Peral, J. Capmany and J. Marti, "Iterative solution to the Gel' Fand-Levitan-Marchenko coupled equations and application to synthesis of fiber gratings," IEEE J. Quantum Electron., vol. 32, pp. 2078-84, Dec. 1996.

[25] I. Arnedo, M. A. G. Laso, D. Benito and T. Lopetegi, "A series solution for the synthesis problem in microwaves based on the coupled-mode theory," accepted for publication, IEEE Trans. Microw. Theory Tech., 2008.

[26] T. Lopetegi, F. Falcone, B. Martínez, R. Gonzalo and M. Sorolla, "Improved 2-D photonic bandgap structures in microstrip technology," Microwave Opt. Technol. Lett., vol. 22, no. 3, pp.207-11, Aug. 1999.

[27] M. A. G. Laso, M. J. Erro, T. Lopetegi, D. Benito, M. J. Garde and M. Sorolla, "Optimization of tapered Bragg reflectors in microstrip technology," Int. J. Infrared and Millimeter Waves, vol. 21, no. 2, pp. 231-45, Feb. 2000.

[28] M. J. Erro, M. A. G. Laso, T. Lopetegi, M. J. Garde, D. Benito and M. Sorolla, "A comparison of the performance of different tapers in continuous microstrip electromagnetic crystals," IEEE Microwave Opt. Technol. Lett., vol. 36, no. 1, pp. 37-40, Jan. 2003.

[29] F. Falcone, T. Lopetegi, M. Irisarri, M. A. G. Laso, M. J. Erro and M. Sorolla, "Compact photonic bandgap microstrip structures," IEEE Microwave Opt. Technol. Lett., vol. 23, no. 4, pp. 233-6, Nov. 1999.

[30] T. Lopetegi, M. A. G. Laso, M. Irisarri, M. J. Erro, F. Falcone and M. Sorolla, "Optimization of compact photonic bandgap microstrip structures," IEEE Microwave Opt. Technol. Lett., vol. 26, no. 4, pp. 211-6, Aug. 2000.

[31] T. Lopetegi, M. A. G. Laso, M. J. Erro, D. Benito, M. J. Garde, F. Falcone and M. Sorolla, "Novel photonic bandgap microstrip structures using network topology," IEEE Microwave Opt. Technol. Lett., vol. 25, no. 1, pp. 33-6, Apr. 2000.

[32] T. Lopetegi, M. A. G. Laso, D. Benito, M. J. Garde, F. Falcone, and M. Sorolla, "Microstrip continuous gratings (MCGs)", Proc. 7th Int. Symp. Recent Adv. Microwave Technol., Malaga, Spain, pp. 601-4, Dec. 1999.

[33] N. V. Nair and A. K. Mallick, "An analysis of a width-modulated microstrip periodic structure," IEEE Trans. Microwave Theory Tech., vol. 32, no. 2, pp. 200-4, Feb. 1984.

[34] F. Martin, J. L. Carreras, J. Bonache, F. Falcone, T. Lopetegi, M. A. G. Laso and M. Sorolla, "Frequency tuning in electromagnetic bandgap nonlinear transmission lines," Electron. Lett., vol. 39, no. 5, pp. 440-2, March 2003.

[35] M. J. Erro, M. A. G. Laso, T. Lopetegi, D. Benito, M. J. Garde and M. Sorolla, "Modeling and testing of uniform fiber Bragg gratings using 1-D photonic bandgap structures in microstrip technology," Fiber Integ. Opt., vol. 19, no. 4, pp. 311-25, 2000.

[36] F. Falcone, F. Martin, J. Bonache, T. Lopetegi, M. A. G. Laso and M. Sorolla, "PBG resonator in coplanar waveguide technology," Proc. 27th Int. Conf. Infrared and Millimeter Waves, San Diego, CA, pp. 355-6, Sept. 2002.

[37] T. Lopetegi, F. Falcone and M. Sorolla, "Bragg reflectors and resonators in microstrip technology based on electromagnetic crystal structures," Int. J. Infrared and Millimeter Waves, vol. 20, no. 6, pp. 1091-102, June 1999.

[38] F. Falcone, T. Lopetegi, M. A. G. Laso and M. Sorolla, "Novel photonic crystal waveguide in microwave printed-circuit technology," IEEE Microwave Opt. Technol. Lett., vol. 34, no. 6, pp. 462-6, Sept. 2002.

[39] T. Lopetegi, M. A. G. Laso, M. J. Erro, F. Falcone and M. Sorolla, "Bandpass filter in microstrip technology using photonic bandgap reflectors," Proc. 29th European Microw. Conf., Munich, Germany, pp. 337-40, Oct. 1999.

[40] M. A. G. Laso, T. Lopetegi, M. J. Erro, D. Benito, M. J. Garde and M. Sorolla, "Multiple-frequency-tuned photonic bandgap microstrip structures," IEEE Microwave Guid. Wave Lett., vol. 10, no. 6, pp. 220-2, June 2000.

[41] J. Tirapu, T. Lopetegi, M. A. G. Laso, M. J. Erro, F. Falcone and M. Sorolla, "Study of the delay characteristics of 1-D photonic bandgap microstrip structures," IEEE Microwave Opt. Technol. Lett., vol. 23, no. 6, pp. 346-9, Dec. 1999.

[42] M. A. G. Laso, T. Lopetegi, M. J. Erro, D. Benito, M. J. Garde and M. Sorolla, "Novel wideband photonic bandgap microstrip structures," IEEE Microwave Opt. Technol. Lett., vol. 24, no. 5, pp. 357-60, Mar. 2000.

[43] M. A. G. Laso, T. Lopetegi, M. J. Erro, D. Benito, M. J. Garde, M. A. Muriel, M. Sorolla and M. Gugliemi, "Chirped delay lines in microstrip technology," IEEE Microwave Compon.. Lett., vol. 11, no. 12, pp. 486-8, Dec. 2001.

[44] M. Kirschning and R. H. Jansen, "Accurate model for effective dielectric constant with validity up to millimeter-wave frequencies," Electron. Lett., vol. 18, no. 6, pp. 272-3, Jan. 1982.

[45] M. N. O. Sadiku, S. M. Musa and R. S. Nelatury, "Comparison of dispersion formulas for microstrip lines," Proc. IEEE SoutheastCon, pp. 378-82, March 2004.

[46] D. M. Pozar, *Microwave Engineering*, 3rd ed., John Wiley & Sons, 2004.

[47] B. M. Kolundzija, and A. R. Djordević, *Electromagnetic Modeling of Composite Metallic and Dielectric Structures,* Artech House Publishers, Oct. 2002.

[48] H. M. Gerard and O. W. Otto, "Chirp transforms open new processing possibilities [SAW filters]", Microw. Syst. News, vol. 7, no. 10, pp. 85-92, Oct. 1977.

[49] M. A. Jack, P. M. Grant and J. H. Collins, "The theory, design and applications of surface acoustic-wave Fourier-transform processors," Proc. IEEE, vol. 68, pp. 450-68, Apr. 1980.

[50] C. C. W. Ruppel and L. Reindl, "SAW devices for spread-spectrum applications," Proc. IEEE Int. Symp. Spread-Spectrum Tech. Appl., Mainz, Germany, pp. 713-9, 1996.

[51] C. C. W. Ruppel, L. Reindl and R. Weigel, "SAW devices and their wireless communications applications," IEEE Microw. Mag., vol. 3, pp. 65-71, June 2002.

[52] W. G. Lyons, D. R. Arsenault, A. C. Anderson, T. C. L. C. Sollner, P. G. Murphy, M. M. Seaver, R. R. Boisvert, R. L. Slattery and R. W. Ralston, "High temperature superconductive wideband compressive receivers," IEEE Trans. Microw. Theory Tech., vol. 44, pp. 1258-77, July 1996.

[53] A. Papoulis, *Systems and Transforms with Applications in Optics*, New York: McGraw-Hill, 1968.

[54] B. H. Kolner, "Space-time duality and the theory of temporal imaging," IEEE J. Quantum Electron., vol. 30, pp. 1951-63, Aug. 1994.

[55] J. Azaña and M. A. Muriel, "Real-time optical spectrum analysis based on the time-space duality in chirped fiber gratings," IEEE J. Quantum Electron., vol. 36, pp. 517-26, May 2000.

[56] M. A. G. Laso, T. Lopetegi, M. J. Erro, D. Benito, M. J. Garde, M. A. Muriel, M. Sorolla and M. Gugliemi, "Real-time spectrum analysis in microstrip technology," IEEE Trans. Microwave Theory Tech., vol. 51, no. 3, Mar. 2003.

[57] J. Schwartz, J. Azaña and D. V. Plant, "Experimental demonstration of real-time spectral analysis using dispersive microstrip," IEEE Microwave Compon.. Lett., vol.16, n.4, pp.215-217, Apr. 2006.

[58] J. Schwartz, J. Azaña and D. V. Plant, "Real-time microwave signal processing using microstrip technology," Proc. IEEE MTT-S Int. Microw. Symp. Dig., San Francisco, CA, pp. 1991-4, June 2006.

CHAPTER 3

Tunable Time-Delay Systems

In this chapter, we explore the potential role CEBG structures can play in achieving tunable time-delay for UWB microwave systems. We experimentally demonstrate how CEBG structures can be configured to yield continuously tunable delays of up to several nanoseconds for signals spanning several GHz of bandwidth. Such delays are greater than those achieved by many recently reported UWB electronic techniques, and the technique does not require inconvenient and/or expensive optical hardware, large banks of switched delay lines, or lossy acoustic/magnetostatic structures.

3.1 Introduction

3.1.1 Areas of Application

Controllable time-delays are an essential component for a number of communications systems and are generally deployed wherever synchronous or time-sensitive transmission/detection schemes are necessary. For example, there is the traditional problem of using a phase-shifter to synchronize a local clock signal with an incoming data stream, a practice with a rich and varied history unto itself [1]. Here, however, we will differentiate this kind of simple phase-shifting of a periodic signal from our goal of "true time-delay" (TTD), which can be defined as 'distortionless time-delay for broadband signals'. The most basic TTD system is in fact just a standard length of transmission line, which (if properly designed for a given frequency regime) subjects an input signal to a fixed travel-time regardless of the transmitting frequency. There exist many applications, as we will describe, for which a tunable TTD is highly desirable. We define an ideal, tunable TTD system as an all-pass, linear-phase device where the phase is

externally controlled by applied voltage (Fig. 3.1). Since it is intuitive that changing a length of coaxial cable or microstrip 'on-the-fly' is not practical, techniques for adjusting the delay of an UWB signal, nominally in a continuous fashion, are especially noteworthy.

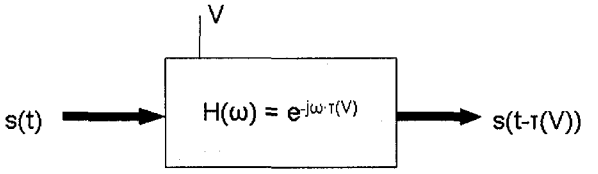

Fig. 3.1. An ideal voltage-controlled TTD line.

One of the primary motivators behind modern research into tunable TTD systems is in the field of phased-array antennas (PAA), in which closely-spaced antenna elements are fed by a common signal arriving with each element's input at some set phase-shift relative to its neighbor. The aggregate result of having many such elements is that the output beam can be directed out at a tunable "scan angle" because of constructive interference in direction of desired propagation and destructive interference elsewhere (Fig. 3.2, left) [2]. Tunability of the output direction is achieved by changing the relative phases of the signal for each antenna element. It is easily shown that ordinary phase-shifting is insufficient for PAA operation when the input signals vary in frequency, since the beam-direction is sensitive to input frequency, a phenomenon commonly referred to as "beam-squinting". Research into tunable TTD schemes was spurred in large part by the goal of creating PAA systems with frequency-independent, configurable scan angles.

Considering the growing interest in UWB communication (as discussed in Section 1.1.1) and broadband high-resolution radar, tunable UWB TTD systems have also been targeted for receiver synchronization and correlation-type operations. For example, the transmit-reference scheme proposed in [3] suggests that UWB pulses can be transmitted in pairs with a predefined delay between the first pulse and second. The first pulse acts as a reference, while the second is modulated. A UWB receiver would therefore need to correlate the second pulse

with a delayed copy of the first (reference) pulse to extract the data. As was observed in [4], the principal challenge associated with this (and other) design architecture is the need for a continuous-time UWB delay line.

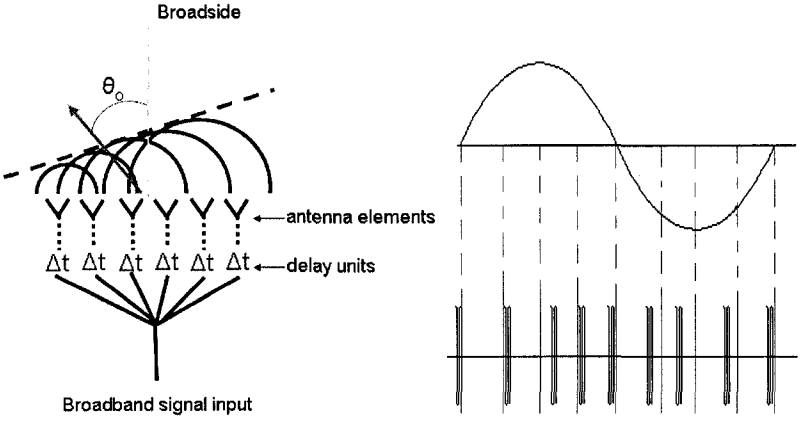

Fig. 3.2. (Left) Conceptual illustrations of a phased-array antenna. (Right) A pulse-position modulation encoded sequence featuring eight frames of data.

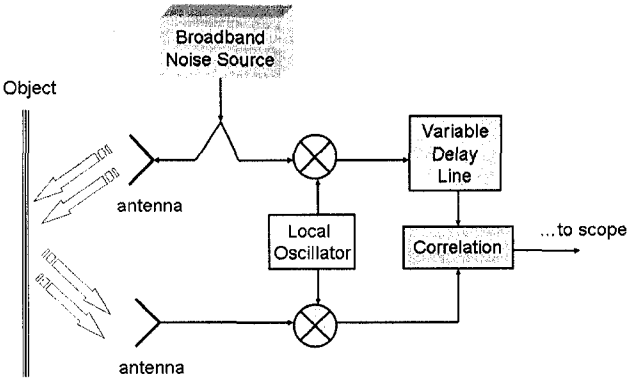

Fig. 3.3. Schematic of a noise-based radar, which correlates a wide bandwidth of noise with a reflected response from a nearby object.

Ideally, a delay stage intended for UWB receivers should offer continuously-tunable delays of up to 1 ns without significant loss [5]. Adjustable delay, assuming it can be switched quickly enough, is also of potential use in UWB encoding schemes such as pulse-position modulation (Fig. 3.2, right), in which information is encoded in a series of pulses (together forming a data symbol) by varying the location of each pulse within a designated time frame [6]. Tunable time-delay systems also attract interest in certain broadband radar systems, since received reflections can sometimes only be properly correlated with a delayed

copy of the transmitted signal (e.g. the noise-based radar of Fig. 3.3 [7]) in a synchronized process in which the local copy must be properly timed.

3.1.2 Existing Techniques

Even when we restrict discussion to signals having GHz-order bandwidths, tunable electrical delay is, in principle, an easy thing to introduce. The most basic technique for variable TTD employs nothing more than a few switches and transmission lines of varying lengths, routing the signal through them as necessary (Fig. 3.4, left). This yields discrete values for system delay and usually consumes a large area. Alternatively, fine control for UWB delays on a single line has been established using non-linear transmission line (NLTL) techniques in which the capacitance of the line is adjusted by inserting voltage-controlled non-linear elements (e.g. varactor diodes) [8]-[10]. These two strategies have also been combined in series to produce systems with large adjustable delays [11].

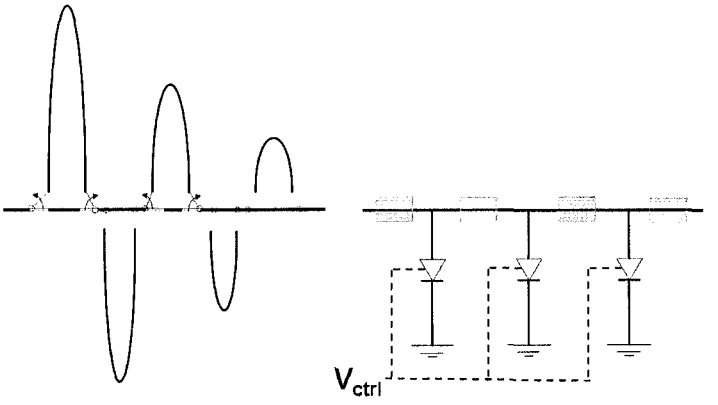

Fig. 3.4. Depictions of switched-delay lines (left) and an NLDL delay scheme (right).

Recent demonstrations of ultra-broadband tunable time-delay fall into a number of categories: There exist integrated circuit designs with both digital (quantized) [4] and analog [5] approaches; NLTL techniques based on varactors [8]-[11]; metamaterials [12]; and a wide-variety of photonics-assisted techniques [13]-[19]. A brief summary of the reported capabilities of these systems is presented in table 3.1. Photonics techniques have been investigated in detail for PAA use because they are lightweight, resistant to EM-interference, and can easily accommodate any RF bandwidth of interest. Unfortunately, optical

solutions tend to involve expensive or difficult-to-integrate hardware: tunable laser sources, chirped fiber Bragg gratings and bandpass filters. Conversely, integrated solutions [4], [5] are very valuable for not consuming much area, but they provide only discretely tunable, short delays in the tens of picoseconds. NLTL techniques show promising performance, but are somewhat encumbered by thermal sensitivity and the requirement for relatively large applied voltages (~20V). An approach using composite right/left-handed (CRLH) transmission lines was recently demonstrated [12] which in fact used the very same strategy as our CEBG implementation (see next section), but was much more limited in operating bandwidth and featured delay-sensitive distortion that is not simple to correct.

Table 3.1
Comparison of existing tunable UWB TTD strategies

Approach	Device Scale	Adjustable Excursion	Bandwidth	Challenges
Switched Lines	Board-level (2-D)	Discrete, ns-scale delay if long board-traces used	Dictated by transmission line	Large planar area, discrete delays
Photonic Components [13]-[19]	Bulk Components	Continuous, ns-scale	> 20 GHz reported	Optical hardware – tough to integrate, costly
Bipolar/CMOS Delay stages [4], [5]	Integrated Circuit	60ps stages reported	~ 10 GHz reported	Small, discrete delay values
NLTL approaches [8]-[11]	A few mm^2	~100 ps reported	~20 GHz reported	Temperature sensitive, large applied voltages
Metamaterials (CRLH) [12]	Board-level (1-D)	Continuous, ~3 ns	<1 GHz	Non-linear distortion difficult to correct. Very long traces.
CEBG (this work)	Board-level (1-D)	Continuous, 1-2 ns	~ 10 GHz	Long traces, broadband mixers & VCO required

3.2 Tunable TTD System

3.2.1 Proposed Design

The tunable TTD system we investigated is presented in Fig. 3.5 and is modeled on an earlier system in which the dispersive elements were chirped SAW structures [20][1]. In the first step, an UWB input signal of bandwidth $\Delta\omega_{RF} = \omega_2 - \omega_1$ (ω_2 & ω_1 are the extreme frequencies of the signal) is mixed with the output of a broadband voltage-controlled oscillator (VCO), hereafter referred to as the local oscillator (LO), of an adjustable frequency $\omega_{LO} \pm \Delta\omega_{LO}/2$. We then consider the difference-frequency mixing product, centered at an intermediate frequency (IF) $\omega_{IF} = \omega_{LO} - (\omega_2+\omega_1)/2$, which is passed to the first dispersive transmission line (CEBG1). Because CEBGs are operated in reflection, broadband directional couplers are used to circulate the signal (we used commercially available broadband 4-port directional couplers from Pulsar Microwave, which exhibited 6-8 dB coupling across very broad bandwidths). In the CEBG line, the signal reflects after traveling a distance down the line determined by ω_{IF}, which is controlled by adjusting the VCO. The round-trip time of the signal as it passes down and back up the CEBG line is therefore determined exclusively by the setting of ω_{LO} and the group delay slope of the line. The full tunable range of delay (the 'delay excursion') finally depends on the bandwidth of the VCO and the group delay slope of the dispersive line, according to:

$$\Delta t = \left| \sigma \cdot \frac{\Delta\omega_{LO}}{2\pi} \right| \tag{3.1}$$

The reflected signal can then be reconverted to its original bandwidth through another mixing operation with the same LO and using appropriate filtering. At this point, we must examine what has become of the signal after reflection in CEBG1 (point **'A'** in Fig. 3.5). The signal being delayed is broadband, so naturally, it will be dispersed when exposed to the broadband dispersive line, CEBG1, and thus it does not resemble the original signal.

1 The referenced work achieved 30 μs delays for 10 MHz bandwidth signals.

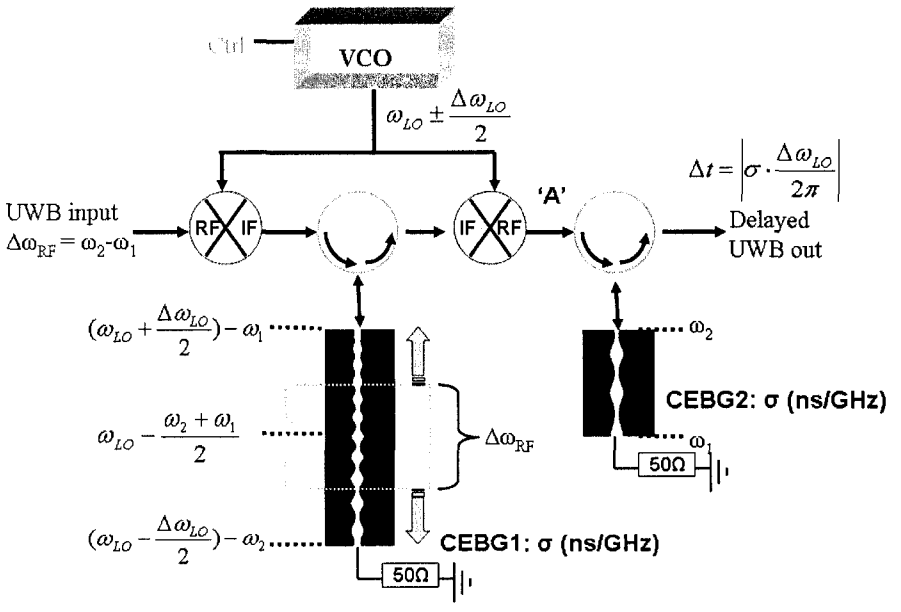

Fig. 3.5. Schematic of the demonstrated tunable time-delay system.

In an early experiment we (somewhat naïvely) assumed that to avoid having our signal distorted by the dispersion of the line, this technique was suitable only for narrowband signals (in which the bandwidth of the signal was much smaller than that of the CEBG) [21]. The data we obtained from a "simplified" system, where the output is evaluated at point 'A' in Fig. 3.5, is presented in Fig. 3.6 because it is informative: a narrowband signal (a 2-ns long nearly sinusoidal pulse of 4 GHz) was mixed with an LO tuned between 7.5-12 GHz and delayed using the prototype CEBG described in Section 2.2.2. In observing the results, it becomes clear that as the LO is tuned the relative delay of the signal (see Fig. 3.6, right) is clearly experiencing the significant group-delay ripple of the prototype (Fig. 2.8) as a result of it being narrowband. A similar effect is observed in the metamaterial-based demonstration of [12], which used the same configuration but a composite left/right-handed transmission line which has a non-linear dispersion characteristic and is lacking in any dispersion-compensation (moreover, the transmission line of [12] was about 60 cm in length, approximately twice the size of the CEBG used here).

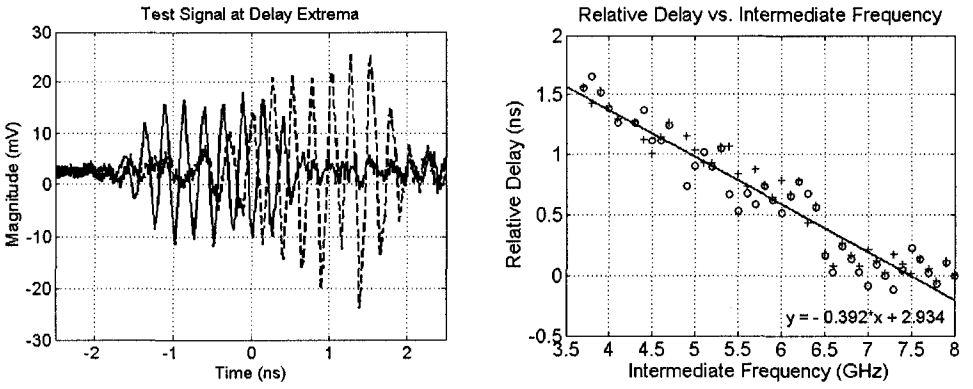

Fig. 3.6. Experimentally measured results for a simple "time-windowed sinusoid", considered as a narrowband input signal, for the "simplified" tunable time-delay system without dispersion compensation. (Left) Time-domain oscilloscope measurements at the delay extremes (solid and dashed) which show rather poor amplitude variation in the response. (Right) Plotted points of system delay vs. intermediate frequency, show strong group-delay ripple for two identical CEBG boards (+ and o symbols from different measurements) with a 'linearized' average slope (solid trace) of -0.39 ns/GHz.

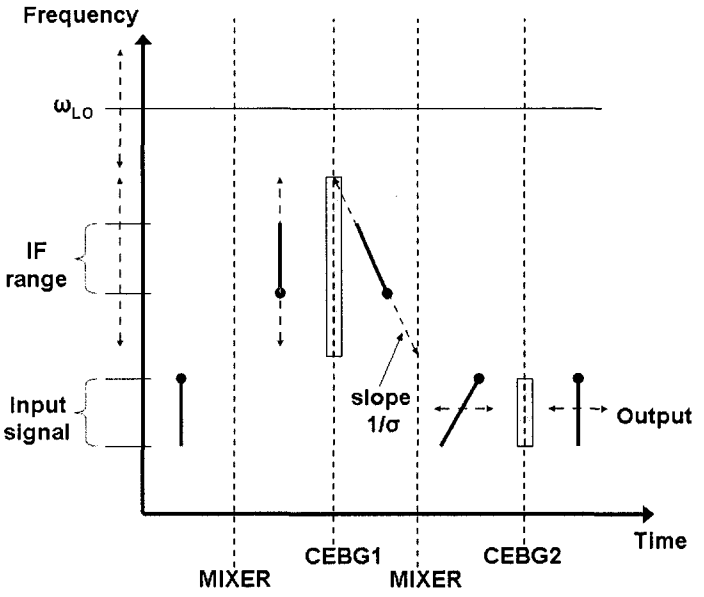

Fig. 3.7. Conceptual diagram of each step of the TTD system in the frequency and time domains. Each section of the x-axis represents a step between the components of the system, and the signal is given an orientation (solid ball) to show how difference-frequency mixing inverts the spectral components. The dashed arrows illustrate what happens as the local oscillator ω_{LO} is varied. After dispersion in CEBG1, the signal is spectrally ordered in time according to the group delay slope σ, the accompanying translation in time has occured depending on the value of ω_{LO}. The down-converted output signal, in the original bandwidth, must be "compressed" to remove the dispersion introduced by the first CEBG.

In order to have truly broadband TTD operation, the dispersion introduced by CEBG1 must be compensated. Fortunately, a second CEBG structure configured for the original signal bandwidth can be used for this operation by designing it with the exact same group delay slope as the first line. To see how this is so, we recall that the output mixing step causes an inversion of the chirp direction of the signal (i.e. a down-chirped signal becomes up-chirped when difference-frequency mixed against a sinusoid). A step-by-step illustration of this process in a frequency-vs.-time representation of the system is presented in Fig. 3.7, showing how the adjustment of LO in the frequency domain eventually results in a shift in the time-domain because of the frequency-ordering properties of the CEBG. The figure is broken down to show the signal distribution at five stages (input, after the first mixer, after CEBG1, after the second mixer, output of CEBG2).

3.2.2 Simulation & Measurement Results

In our demonstration of a tunable TTD system using CEBGs [22], [23], we selected the frequency range for the input as 3 to 7 GHz, and a large LO range from 14 to 18 GHz – resulting in a possible range of intermediate difference frequencies from 7 GHz (14-7) to 15 GHz (18-3). The choice of these frequencies was bounded by the simulation time required on the high-end and the reflectivity levels of the CEBGs on the low-end (below 3 GHz there would be very insufficient periods for good reflectivity). Two CEBG structures were designed on alumina substrate (1.27 mm thick, $\varepsilon_r = 9.5$, $\tan\delta = 0.0007$) diced to 10x5 cm and having a target group delay slope of $\sigma = -0.4$ ns/GHz. According to (3.1) this should yield adjustable time-delays of up to 1.6 ns.

The 'CEBG1' structure was 21.6 cm in length and spanned 7 to 16 GHz (see Fig. 3.8 for a photograph), while the "baseband UWB" line 'CEBG2' was 14.8 cm and spanned 3 to 7 GHz. Measured $|S_{11}|$ and group delay responses are presented in Fig. 3.9 using a 20 GHz Agilent VNA (8703B) and the results compare favorably, with measured group delay slopes of -0.39 ns/GHz

(linearized) in both cases and only some slight added attenuation and delay in CEBG1, suspected to be caused by connectorization mismatch (Fig. 3.9).

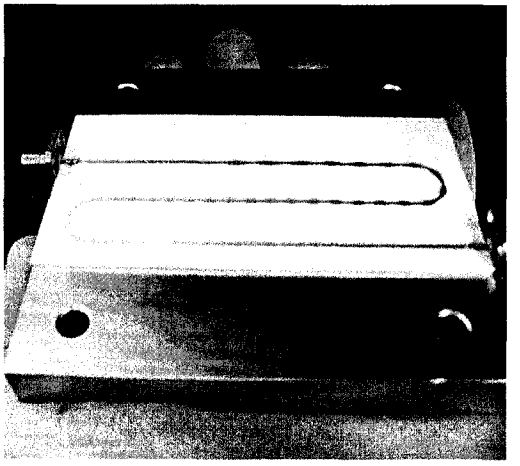

Fig. 3.8. (Left) Photograph of CEBG1.

A test signal was generated using a 500 mV, 3 Gbps 13-bit train of pulses '1010000010101' generated by an Anritsu Pulse Pattern Generator (MP1763B, having a rise time of 30 ps) run through a commercial broadband mixer (LO = 5 GHz) to simulate an UWB waveform with frequency content concentrated between 3 and 7 GHz. The mixer additionally shaped the input signal (due to its bandpass response) – the measured system input is presented in Fig. 3.10 in envelope only (due to the mixing process having a random phase with respect to the digital sampling of the oscilloscope, which was timed according to the pulses and not the LO).

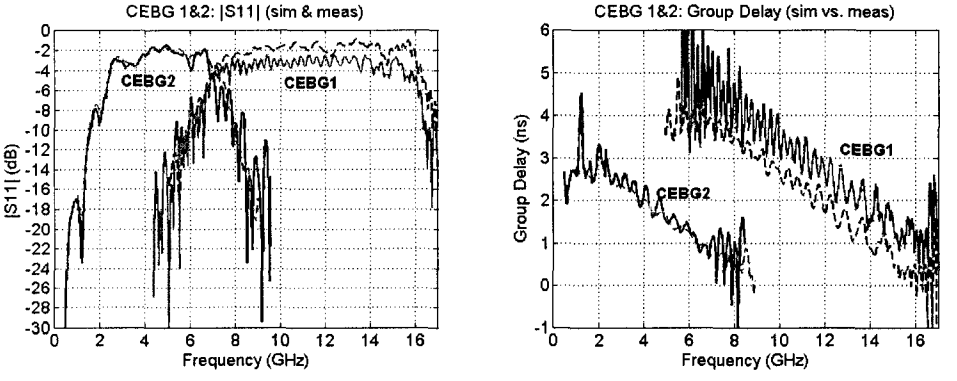

Fig. 3.9. Comparison of simulated and measured |S11| (left) and group delay (right) for both CEBG structures in the tunable TTD experiment. CEBG1 (solid –measured, dash – simulation)

experienced slightly increased attenuation and delay levels, whereas that data for CEBG2 (solid – measured, dash – simulation) agrees well.

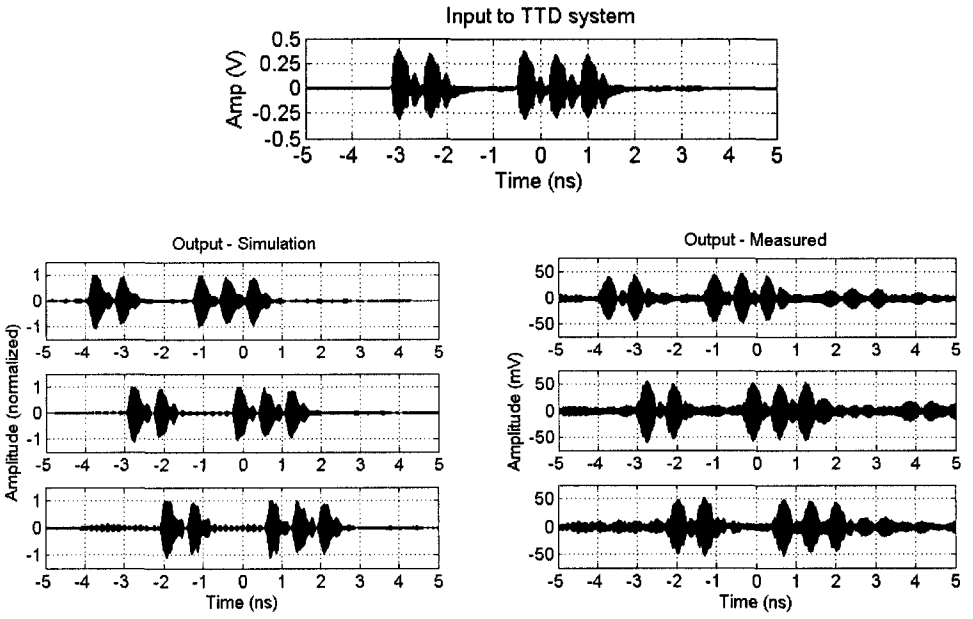

Fig. 3.10. (Top) Measured input signal with 3-7 GHz content (envelope only). (Left) Simulation results assuming lossless quadratic-phase bandpass filters and ideal mixing. Three LO frequencies are used: 18.3 GHz (upper), 15.9 GHz (middle) and 13.8 GHz (lower). (Right) Measured results for the same LO frequencies using the realized CEBGs and commercial mixers/couplers.

This signal was up- and down-converted using further commercial mixers and an LO generated by a local signal synthesizer was tuned by hand in the range from 13.8 to 18.3 GHz ($\Delta\omega_{LO} = 2\pi \cdot 4.5$ Grad/s), emulating the broadband VCO that the system would otherwise require (see Fig. 3.5). It was noted that frequencies above 18.3 GHz suffered from too much attenuation due to the limits of SMA connectors. A pair of 15-GHz-bandwidth, 15 dB amplifiers (Picosecond Pulse Labs #5867) was employed to compensate for losses incurred in mixing and directional coupling through an 8 and 6 dB coupler (for the first and second CEBG lines, respectively). The signal was detected with a high-frequency electrical sampling module (Tektronix 80E03) and the results are displayed in Fig. 3.10 for three LO values including the extremes of delay. As can be seen, despite some elevated noise (as would be expected through two mixers), the UWB pulses are well preserved and the results compare favorably with simulations using ideal quadratic-phase filters and mixers (Fig. 3.10, left), although the measurements

show some additional noise contribution and LO leakage which can be attributed to the behavior of the mixers. The continuously tunable nature of the delay is stressed in Fig. 3.11, in which we slowly vary the LO and record the location of the first pulse to plot the delay, which matches extremely well with prediction. This close agreement is in stark contrast to Fig. 3.6, in which a narrowband signal was used – and confirms that the group delay ripple does not significantly hamper system performance provided the signal is sufficiently broadband.

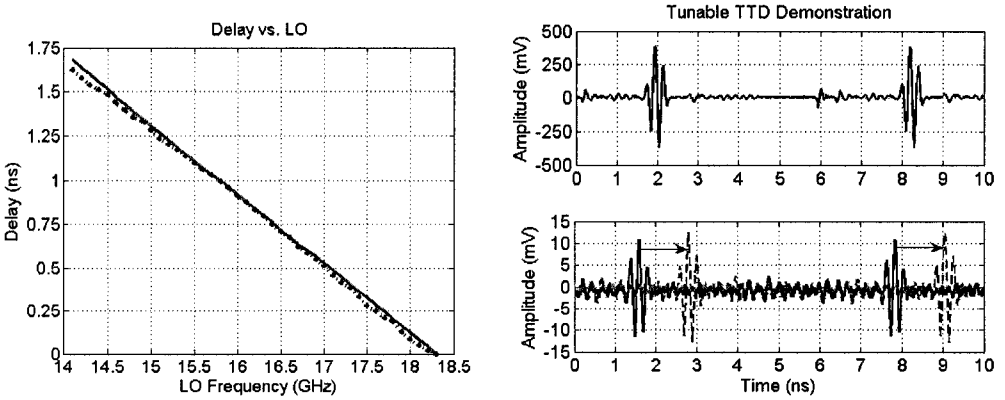

Fig. 3.11 (Left) Simulated (solid) & measured (dash) tuned time delay, based on location of first pulse as the LO frequency is adjusted. The measured result is nearly linear with an average slope of -0.393 ns/GHz and shows excellent agreement with simulated data. (Right): (upper) A train of two test UWB impulses generated using an EBG synthesis tool and (lower) the corresponding measured time-delayed responses for LO = 17.5 GHz (solid) and 14.3 GHz (dash).

A second UWB test signal was designed to allow its phase-information to be directly observed with the oscilloscope – it consisted of a shaped impulse with content in the 3-7 GHz range. This signal was generated by passing a -7.5 volt, 70 ps impulse (generated by a Picosecond Pulse Labs 3600D) through a specially synthesized EBG microstrip designed using a recently-proposed synthesis algorithm for creating customized UWB pulse shapes [24]. The original signal and time-delayed outputs are presented (Fig. 3.11, right) for two LO frequency points (17.5 GHz and 14.3 GHz). 10-point averaging was used in the oscilloscope for clarity and to distinguish from some mixer LO-leakage in the down-conversion step.

3.2.3 Conclusions

We have demonstrated a working all-electronic continuously-tunable time-delay system with a 1.6 ns delay excursion and a 4 GHz bandwidth. This is the first demonstration to use dispersive bandgap structures in microstrip for this purpose. In comparison to other aforementioned electronic techniques for UWB delay [4], [5], [8]-[11], the chirped bandgap method provides larger, more continuous delays at the expense of long board traces and the power required to drive a local broadband oscillator. It is evident that any arrayed application of the system (e.g. for a PAA) would unfortunately require multiple CEBG lines (large area) and significant power consumption. On the other hand, deployment as part of a UWB base-station receiver or in a radar system would be straightforward. Optimizing this system for deployment would depend on the application being targeted, but some preliminary points can be made here. Solutions to potentially help reduce overall system size include: (i) recent demonstrations of very compact (~ 2 cm^2) UWB 3-dB directional couplers in microstrip technology [25], or integrated into the CEBG itself; (ii) the possibility of superimposing the two CEBG structures to conserve space [26]; and (iii) stripline-based CEBGs with higher ε_{eff}, resulting in shorter structures. As regards signal level, an integrated UWB coupler could be significantly better than the commercial 6-dB and 8-dB couplers purchased for this demonstration, and active broadband mixers could be employed instead of simple diode-mixing to make amplifiers unnecessary. The authors suspect that the principal challenge associated with the deployment of this system would be the design of a broadband VCO with sufficient power to drive a pair of mixers, since the bandwidth of such a VCO is a determining factor of system delay based on (3.1). Ultra-broadband, high-power VCOs are seldom employed but have existed for some time –for example, a 9-to-18 GHz, 12 dBm VCO was demonstrated in [27] that would be suited for such an application.

References

[1] B. Razavi, *Monolithic Phase-locked Loops and Clock Recovery Circuits: Theory and Design*, New York: IEEE Press, 1996.

[2] H. J. Visser, *Array and Phased Array Antenna Basics*, Chichester: Wiley, 2005.

[3] R. T. Hoctor and H. W. Tomlinson, "Delay-hopped transmitted reference RF communications," Proc. IEEE Conf. Ultra-Wideband Syst. Tech., pp. 265-70, May 2002.

[4] S. Bagga, L. Zhang, W. A. Serdijn, J. R. Long and E. B. Busking, "A quantized analog delay for an ir-uwb quadrature downconversion autocorrelation receiver," Proc. IEEE Conf. Ultra-Wideband Syst. Tech., pp. 328-32, Sept. 2005.

[5] L. Zhou, A. Safarian and P. Heydari, "A CMOS wideband analogue delay stage," Electron. Lett., vol. 42, no. 21, pp. 1213-5, Oct. 2006.

[6] C. F. Liang, S. T. Liu, S. I. Liu, "A calibrated pulse generator for impulse-radio UWB applications," IEEE J. Solid-State Circ., vol. 41, no. 11, pp. 2401-7, Nov. 2006.

[7] B. M. Horton, "Noise-modulated distance measuring systems," Proc. Inst. Radio Engrs, vol. 47, no. 5, pp. 821-8, May 1959.

[8] D. Kuylenstierna, A. Vorobiev, P. Linner, and S. Gevorgian, "Ultrawide-band tunable true-time delay lines using ferroelectric varactors," IEEE Trans. Microwave Theory Tech., vol. 53, no. 6, pp. 2164-70, Jun. 2005.

[9] C. C. Chang, C. Liang, R. Hsia, C. W. Domier, and N. C. Luhmann, "True time phased array system based on nonlinear delay line technology," Proc. Asia-Pacific Microw. Conf., Taipei, Taiwan, R.O.C., pp. 795-9, Nov. 2001.

[10] W. M. Zhang, R. P. Hsia, C. Liang, G. Song, C. W. Domier and N. C. Luhmann Jr., "Novel low-loss delay line for broadband phased antenna array applications." IEEE Microwave Guid. Wave Lett., vol. 6, no. 11, pp. 395-7, Nov. 1996.

[11] P. Abele, R. Stephan, D. Behammer, H. Kibbel, A. Trasser, K. B. Schad, E. Sommez, and H. Schumacher, "An electrically tunable true-time-delay line on Si for a broadband noise radar," Top. Meet. Silicon Monolithic Integrated Circ., Grainau, Germany, pp. 130-3, Apr. 2003.

[12] S. Abielmona, S. Gupta and C. Caloz, "Experimental demonstration and characterization of a tunable CRLH delay line system for impulse/continuous wave," IEEE Microw. Wireless Compon. Lett., vol. 17, no. 12, pp. 864-6, Dec. 2007.

[13] B. Howley, X. Wang, M. Chen and R. T. Chen, "Reconfigurable delay time polymer planar lightwave circuit for an X-band phased-array antenna demonstration," J. Lightwave Tech., vol. 25, no. 3, pp. 883-90, Mar. 2007.

[14] Z. Liu, X. Zheng, H. Zhang, Y. Guo and B. Zhou, "X-band continuously variable true-time delay lines using air-guiding photonic bandgap fibers and a broadband light source," Optics Lett., vol. 31, no. 18, pp. 2789-91, Sept. 2006.

[15] D. Borg and D. B. Hunter, "Tunable microwave photonic passive delay line based on multichannel fibre grating matrix," Electron. Lett., vol. 41, no. 9, pp. 537-8, Apr. 2005.

[16] S. S. Lee, Y. H. Oh, S. Y. Shin, "Photonic microwave true-time delay based on a tapered fiber Bragg grating with resistive coating," IEEE Photon. Tech. Lett., vol. 16, no. 10, pp. 2335-7, Oct. 2004.

[17] J. L. Corral, J. Marti, J. M. Fuste rand R. I. Laming, "True time-delay scheme for feeding optically controlled phased-array antennas using chirped-fiber gratings," IEEE Photon. Tech. Lett., vol. 9, no. 11, Nov. 1997.

[18] Y. G. Han, J. H. Lee and S. B. Lee, "Continuously tunable photonic microwave true-time delay based on tunable chirped fibre Bragg grating," Electron. Lett., vol. 42, no. 14, pp. 811-2, Jul. 2006.

[19] Z. Shi, Y. Jiang, B. Howley, Y. Chen, F. Zhao and R. T. Chen, "Continuously delay-time tunable-waveguide hologram module for X-band phased-array antenna," IEEE Photon. Tech. Lett., vol. 15, no. 7, Jul. 2003.

[20] V. S. Dolat and R. C. Williamson, "A continuously variable delay-line system," Proc. Ultrasonics Symp., New York, NY, pp. 419-23, Sept.1976.

[21] J. Schwartz, J. Azaña and D. V. Plant, "Real-time microwave signal processing using microstrip technology," IEEE MTT-S Int. Microw. Symp. Dig., San Francisco, CA, pp. 1991-4, Jun. 2006.

[22] J. Schwartz, J. Azaña and D. V. Plant, "Design of a tunable UWB delay-line with nanosecond excursions using chirped electromagnetic bandgap structures," 4th IASTED Int. Conf. Antennas, Radar and Wave Propagation (ARP 2007), Montreal, Canada, May 2007.

[23] J. Schwartz, I. Arnedo, M. A. G. Laso, T. Lopetegi, J. Azaña and D. V. Plant, "An electronic UWB continuously tunable time-delay system with nanosecond delays," accepted for publication, IEEE Microwave Compon. Lett., Feb. 2008.

[24] I. Arnedo, M. A. G. Laso, D. Benito and T. Lopetegi, "A series solution for the synthesis problem in microwaves based on the coupled mode theory," accepted for publication, IEEE Trans. Microw. Theory Tech., 2008.

[25] A. M. Abbosh and M. E. Bialkowski, "Design of compact directional couplers for UWB applications," IEEE Trans. Microwave Theory Tech., vol. 55, no. 2, pp. 184-194, Feb. 2007.

[26] M. A. G. Laso, T. Lopetegi, M. J. Erro, D. Benito, M. J. Garde and M. Sorolla, "Multiple-frequency tuned photonic bandgap microstrip structures," IEEE Microwave Guid. Wave Lett., vol. 10, no. 6, pp. 220-222, June 2000.

[27] M. Kimishima and Y. Ito, "A 9 to 18 GHz small-size hybrid broadband VCO using active match circuits," Proc. 20th European Microwave Conf., pp. 322-327, Sept. 1990.

CHAPTER 4

Temporal Imaging Systems

In this chapter, we describe an electronic system for the distortionless temporal imaging (magnification, compression, reversal) of microwave signals based on an analogy to spatial lens-based imaging systems. We compare current state-of-the-art temporal imaging systems employing photonics to one demonstrated for the first time here, a fully-electronic UWB time-stretching system, which makes use of CEBGs to provide the required broadband dispersion. We experimentally demonstrate a 5X time-magnification on a 0.6 ns time-windowed signal having up to 8 GHz of bandwidth. We also present simulation data for similarly designed time-compression and time-reversal systems, and we discuss the practical limits of fully-electronic temporal imaging as compared to their optically-assisted counterparts.

4.1 Introduction

4.1.1 Definition and Applications

Temporal imaging is an umbrella term used to describe a system in which an arbitrary time-limited signal is magnified, compressed and/or reversed in the time-domain without any distortion of the signal envelope, only a corresponding increase or decrease in amplitude in keeping with the conservation of energy (e.g. a magnified pulse which is longer in time will have correspondingly less amplitude). This operation can be understood as a bandwidth-converting step (not to be confused with single frequency-conversion operation of conventional mixing). Depictions of the three main application regimes of temporal imaging are presented in Fig. 4.1.

Although many possible clever uses for temporal imaging (TI) systems exist, such as for desensitizing optical transmission systems to fiber dispersion [1], the most common TI application zone is for overcoming the bandwidth or frequency-limitations of existing signal generation and detection technology. Typically, either a received signal is too fast for existing detection equipment and needs to be slowed down, or else it is required to generate some signal waveform having frequency content exceeding the capabilities of existing waveform synthesizers, whether optical or microwave.

The former application for signal detection motivates the need for "time-magnification" systems to slow down fast incoming signal waveforms. TI strategies have yielded several all-optical time-magnification systems for such tasks as observing fast optical events [2] and for optical header preprocessing [3]. For microwave signals, one motivational goal for this technique is to perform high-data-rate analog-to-digital conversion (ADC) [4]. As discussed in Section 1.1.4 (see references therein), modern digital sampling units struggle to keep up with signals spanning the kinds of bandwidths defined for UWB communication. Time-magnification can be deployed to convert a time-windowed input waveform into a range for which the sampler can satisfy the sampling criteria. The extension of the TI method for the ADC of continuous signals is also possible (see Chapter 6).

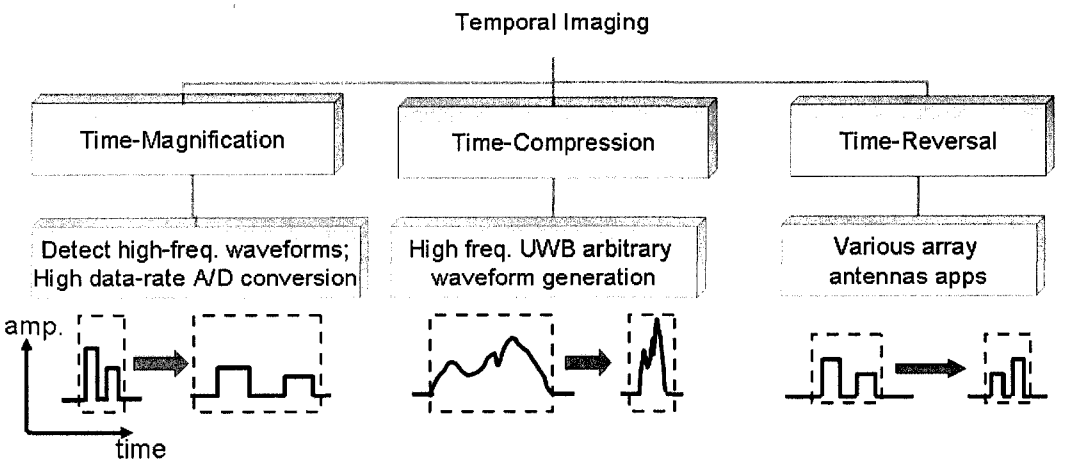

Fig. 4.1 Forms and applications of temporal imaging, along with examples of each (depicted for both digital pulse-based and analog waveforms)

Time-compression systems have generated some interest in the optical community for use in active optical pulse-compression schemes [5]. In the microwave regime, a time-compression stage could be added to the output of an arbitrary waveform generator (AWG) to compress the output and produce customized waveforms with frequency content beyond the capabilities of modern commercial AWG equipment (currently limited to about 5 GHz), as discussed in Section 1.1.5 (see references therein). This has important implications for creating the kinds of customized, orthogonal pulse-shapes expected to be targeted by UWB communication schemes for operation in high-traffic environments [6], [7].

Finally, the potential implementation of a time-reversal system for signals is perhaps less intuitively useful, but does have demonstrable applications in array antennas, acoustics and sonar, specifically for retroreflectors [8], and this function can be performed concurrently with either compression or magnification.

We now provide some insight into the theory behind temporal imaging before describing system implementations.

4.1.2 Theory of Temporal Imaging

As mentioned in Section 2.3, there exists a well-documented duality between the spatial diffraction of a beam of light and the temporal dispersion of a pulse, [9], [10]. Through a series of complementary assumptions applied to the wave equation (monochromatic, paraxial rays in the spatial case and band-limited plane-waves in the temporal case), both can be described by a set of complex parabolic differential equations that are reminiscent of diffusion equations, as discussed in the seminal work of Kolner [11]. This similarity between diffraction and dispersion invites analogous diffraction-based systems from the spatial domain to be translated into the temporal domain, and vice-versa. One example already discussed in Chapter 2 is the real-time Fourier transformation.

As recognized by Papoulis [10] and later developed by Kolner and Nazarathy [12] there exists the possibility of a time-domain dual to the common spatial lens, making possible the kinds of imaging systems in the time-domain that are fundamental to the field of optics. The action of this so-called 'time-lens' is the

dual of that of a thin lens in space – which is to say that since a spatial lens applies (to a first-order approximation) a quadratic-phase modulation in space to an incident wave (proportional to x^2+y^2 if one considers propagation in the z direction), a time-lens consists of an equivalent quadratic-phase modulation in time. For the space and time cases, the action of a lens is to multiply the incident wave by the phase factors $e^{j\varphi(x,y)}$ or $e^{j\varphi(t)}$, respectively for space and time, where the phase terms are defined as:

$$\phi(x,y) = \frac{k(x^2+y^2)}{2f} \quad \phi(t) = \frac{\omega_o \cdot t^2}{2f_t} \tag{4.1}$$

For the traditional spatial thin lens, the customary focal length f and spatial frequency k, which have analogues in the time-domain, being the "focal time" f_t and angular carrier frequency ω_o. The work of Kolner [11] provides a detailed one-to-one correspondence of terms such as focal length/time, f/#, imaging condition and magnification factor for the case of spatial and temporal imaging systems. Further analogies between spatial and temporal lens-based systems were investigated by Lohmann and Mendlovic, who proposed temporal filtering for convolution/correlation functions using 4-f imaging systems [13], and later Naulleau and Leith, who described incoherent temporal imaging [14]. Time lenses have been explored independently for a variety of applications in the optical domain [15].

We now turn to the basic problem of imaging an object, portrayed for both space and time in Fig. 4.2. In the spatial case, a conventional imaging system arrangement consists of an object at a distance d_o away from a lens. The presence of a diffractive medium (e.g. air), followed by the lens, and further diffraction, yields a focused exact image at some distance d_i according to the well-known imaging condition $1/f = 1/d_o + 1/d_i$, where f, the focal length of the lens, depends on its index of refraction and radii of curvature. The image formed experiences some magnification factor M that is the negative ratio of image and object distances: $M = -d_i/d_o$ (the image is thus inverted for the convex lens pictured in Fig. 4.2) [16].

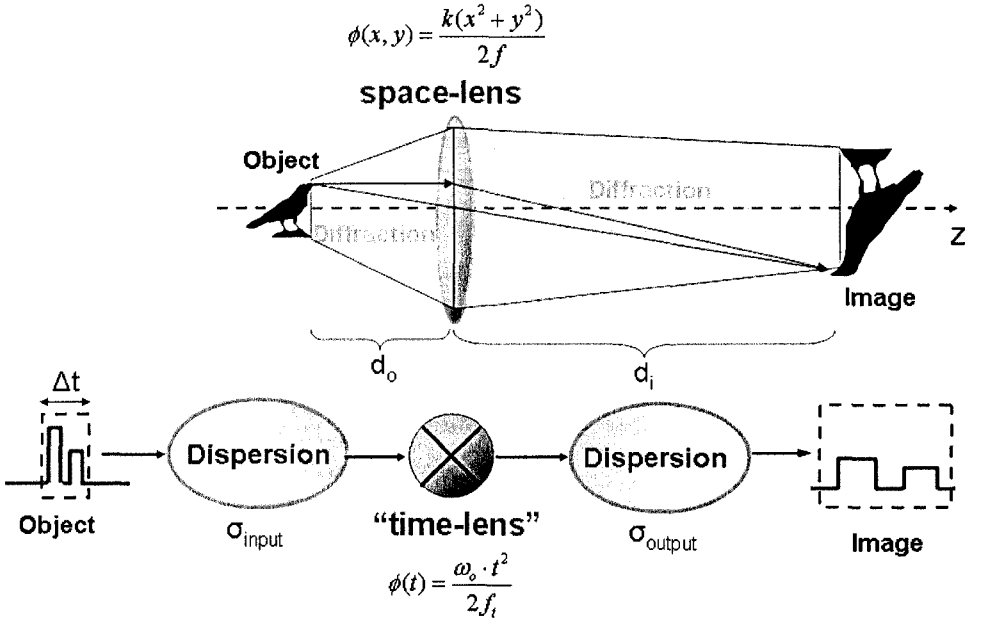

Fig. 4.2. Illustration of spatial (top) and temporal (bottom) magnification systems. In the spatial system, d_o and d_i are the object and image distances, respectively. Note: the spatial (x,y) object shown has no actual z-depth (2-D image), it is shown as an illustration.

In the temporal case, we find the analogous imaging system to be the cascade of a dispersive line, followed by a time lens, and further dispersion. Provided a condition is satisfied (the 'temporal imaging condition', which we will discuss in a moment), a magnification factor M is realized that can be shown [11] to be the "ratio of output dispersion to input dispersion", where such amounts are the product of a dispersive medium's dispersion coefficient $d^2\beta/d\omega^2$ with the signal's path-length ξ through the medium. This can be translated into our preferred units of group delay slope (σ in ns/GHz) for our discussion of CEBG structures as $M = -\sigma_{out}/\sigma_{input}$ (see Appendix A for closed-form analysis yielding this result closely following the derivation of Caputi [17], although it is recommended to read section 4.1.3 beforehand). In this context, $|M| > 1$ indicates time-magnification while $|M| < 1$ is time-compression, and $M < 0$ indicates a time-reversal which may be concurrent with either magnification or compression. As will be demonstrated in the next section, the condition for temporal imaging is defined, using our notation, as:

$$\frac{1}{\sigma_{TL}} = \frac{1}{\sigma_{output}} + \frac{1}{\sigma_{input}} \tag{4.2}$$

where σ_{TL} is the rate of the linear-frequency (quadratic-phase) sweep (hereafter referred to as the "reference frequency sweep") used for the time lens of the system (this term is equivalent to $-\omega_o/f_T$ in Kolner's notation... our preference is to restrict discussion to group delay slopes as opposed to focal times and dispersion coefficients favored by Kolner) It is evident that the magnification and imaging conditions of both time and space imaging systems are duals.

Just as a magnifying glass can only reveal the contents of a local spatial aperture over which it is centered, a temporal imaging system is limited to operating on a particular time-window Δt. This aperture is significant for several reasons. Firstly, the time-window serves to limit the input signal to the range of times over which the modulator comprising the time lens is principally quadratic [11], which depends on the mechanism chosen to generate the reference frequency sweep. Secondly, we must consider the limited frequency range of the output dispersion element (which, for large magnifications, must have a much steeper group delay slope than the input element and can be very bandwidth-limited in a microwave implementation). Supposing a component of the input signal at some moment in time t is temporally in proper focus, a later sample of the input signal at $t + \Delta t$ would be shifted to a different output frequency by the time lens process (a shift in time on a signal entering a time-lens becomes a corresponding shift in frequency). As a result, signal content outside some limited focusing aperture will appear attenuated and distorted, and if far enough outside the temporal window it will not appear at the output at all. We will return to these points with a measurement demonstration in Section 4.2.4.

Temporal imaging systems are also subject to aberrations, much like spatial imaging systems. The treatment of dispersion revolves around a Taylor series expansion of the propagation constant (specifically, the second-order term $d^2\beta/d\omega^2$) and assumes that higher-order terms are negligible, when in reality these terms contribute to aberrations. Similarly, the time-lens assumes an ideal quadratic phase modulation, and deviations from this will result in image

distortions. A detailed treatment of temporal imaging aberrations is presented in [18].

There is also the issue of temporal resolution for TI systems. Kolner [11] derives the minimum time feature that can be resolved in relation to the input temporal window, in which he demonstrates that the system output is actually a magnified/compressed replica of the input waveform convolved with the Fourier transform (in time) of the temporal aperture. It was shown that if a rectangular time-window of length τ is assumed and the first zero of the corresponding output temporal sinc function (Fourier of a rectangular time-window) is taken as a marker, a conservative estimate for the system input resolution is approximately:

$$\delta\tau_{in} = \frac{|\sigma_{in}|}{\tau} \tag{4.3}$$

We will show later in demonstration that realized systems can perform better than this conservative estimate. We will now briefly explore the literature of temporal imaging demonstrations.

4.1.3 Review of Existing Techniques

Several simulated and experimental demonstrations of temporal imaging exist in the literature, and are categorized in Table 4.1 according to the nature of the input signal (optical, microwave) and the signal domains involved (electronic, photonic) in the implementation of the imaging system.

Table 4.1
Demonstrations of temporal imaging

Reference	Input Signal	Implementation
[1] Sakano **[2],[19] Bennett** **[3] Han** **[20],[21] Azaña**	Optical	Photonics
[4], [8], [22] Coppinger	Microwave	Microwave-Photonic
[17] Caputi **[this work] Schwartz**	Microwave	Microwave

In the broadest sense, only two elements are necessary for temporal imaging: (i) a broadband dispersive medium, and (ii) a time lens. We have already

introduced a mechanism for dispersion for broadband electronic signals – the CEBG. What remains is to describe how to implement a broadband, electronic time lens (quadratic-phase modulation in time). The most obvious implementation is to mix the input signal with a flat-amplitude linear frequency sweep. The questions of how to generate a sufficiently broadband, fast frequency sweep, and the manner in which it should be mixed with the signal, represent two key implementation decisions for an UWB electronic temporal imaging system.

Reviewing the literature briefly, the first experimental demonstration of time-magnification is generally credited to the work of Caputi [17] in 1970 and was (until this work, and to the best of the author's knowledge) effectively the only all-electronic demonstration to ever be published. Caputi's simple demonstration of a 2X time-magnification system based on the principles of chirp radar unconsciously mirrored the configuration of a spatial imaging system (prior to a full understanding of time-lensing), a fact which went largely unnoticed at the time. Caputi's so-called "time-stretch" system is illustrated in a simplified, schematic form in Fig. 4.3. He used the limited dispersive networks of his day (333 kHz bandwidth, with group delay slopes of 50 μs/MHz) and a simple electronic time lens: a conventional mixer and a VCO driven by a video saw-tooth generator, with a low-pass filter to isolate the difference-frequency product output.

An input signal of carrier frequency f_o, bandwidth Δf_1, and constrained to time-window Δt_1 is passed through a dispersive element with linear group-delay of slope σ_1 (ns/GHz). If this dispersion is sufficient to satisfy (2.11) then it is effectively a frequency-to-time mapping as in the case of RTFTs (see Section 2.3) and we can represent this signal as approximately a straight line in a frequency vs. time graph.

The dispersed input signal is difference-frequency[1] mixed against a linear frequency sweep (group-delay slope σ_2) centered at frequency f_{LO}. The sweep can

[1] It is possible to perform time-stretching using the sum-frequencies instead. It must be recognized that, unlike conventional modulation, modulation between two chirped signals yields very different upper- and lower-sidebands with very different group delay slopes and bandwidths. The

be generated by either an active (as in the experimental demonstration provided by Caputi) or passive process (as illustrated in Fig. 4.3, where the frequency sweep is generated by sending an impulse through a dispersive network, illustrated in the dashed bounding box). The passive mechanism for generating a reference sweep is a practical alternative to frequency-sweep generation if there are no active means of tuning an oscillator quickly enough or across a broad enough bandwidth -we shall choose this implementation strategy in the next section.

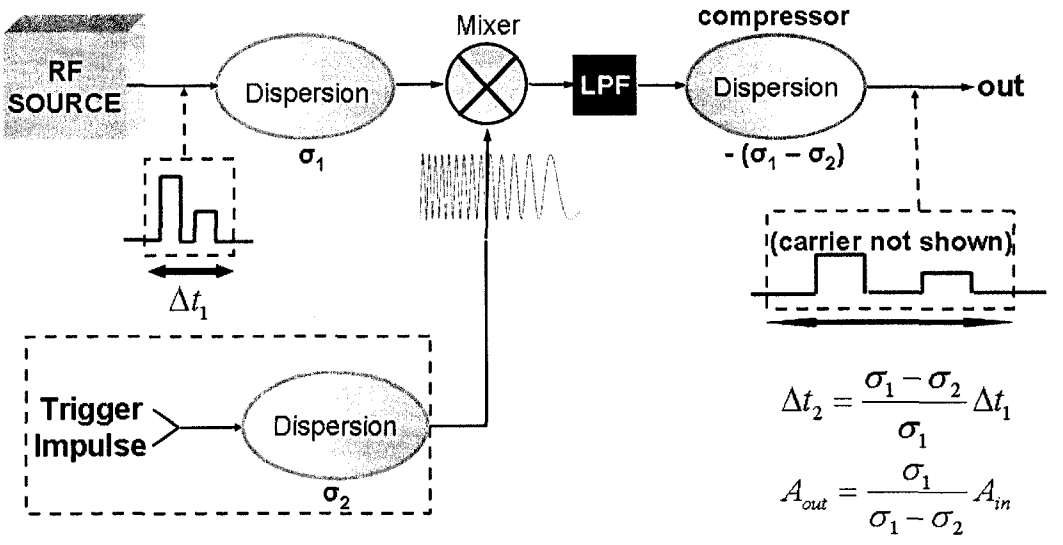

Fig. 4.3 A simplified presentation of the time-stretching system realized by Caputi [17]. Digital bit pulses are shown as input and output samples with carriers hidden for illustrative purposes. Also shown is how the amplitude of the output (A_{out}) has been correspondingly reduced in the magnification.

The time lens output has a reduced central frequency $f_{out} = f_o - f_{LO}$, and a new group-delay slope $(\sigma_1^{-1} - \sigma_2^{-1})^{-1}$. The signal bandwidth is effectively reduced in this step while the signal remains the same duration in time (Fig. 4.4). If the product signal is then compressed (i.e. dispersed by a CEBG with group delay slope $\sigma_3 = -(\sigma_1^{-1} - \sigma_2^{-1})^{-1}$), the original input signal can be recovered from the signal envelope, stretched temporally by the magnification factor $M = -\sigma_3/\sigma_1$ and

decision of which to design for rests upon the available operation bandwidth of the output dispersive network, as well as the choice of a magnifying or compressing system [32].

reduced in amplitude by the same factor, respecting conservation of energy (assuming lossless mixing and dispersion operations). For design purposes, this means that for a given magnification ratio, the reference linear frequency sweep must satisfy the temporal imaging condition of (4.2):

$$\frac{1}{\sigma_2} = \frac{1}{\sigma_1} + \frac{1}{\sigma_3} \tag{4.4}$$

This equality produces an exact, *focused* image. It should be noted that the output signal is effectively an amplitude-modulation on a chirped carrier corresponding to the difference-frequency band created in the mixing process (this is shown explicitly in the derivation of Appendix A). The desired signal must therefore be envelope-detected at the output – a process that is straightforward for optical implementations of temporal imaging, since the act of photo-detection is sufficient to remove the optical carrier frequencies while retaining a microwave signal envelope (one of the several advantages of photonic implementations). For an electronic implementation, it must either be peak-detected (easy) or demodulated with a second chirped modulator (somewhat more involved).

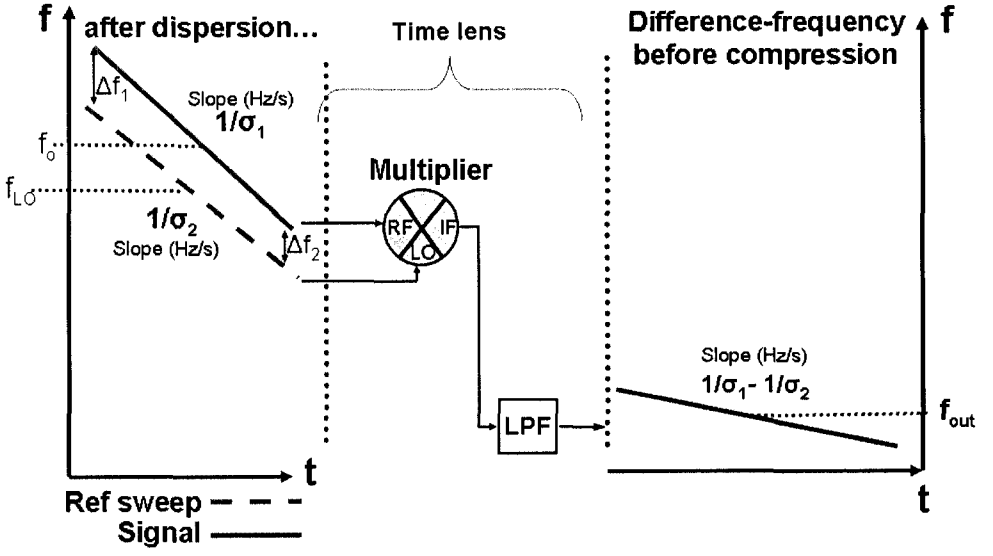

Fig. 4.4 A frequency vs. time representation of the time-lensing operation (as implemented by Caputi [17] and also in this work). The slopes illustrated on the left represent the signal (after dispersion) and reference frequency sweep, which are difference-frequency mixed, producing the output at the right.

Since Caputi's demonstration, the majority of time-lens and temporal imaging demonstrations (whether for signals that are optical in origin, or for microwave signals converted to the optical domain) have involved photonics [1]-[5], [8], [19]-[24]. The primary motivation for this is bandwidth, since optical systems enjoy significant advantages by having carrier frequencies many orders of magnitude greater than those of the microwave signal (see section 4.2.4), however at the time of this work it was the standard assumption that no sufficiently broadband dispersive electrical network even existed in the microwave regime to even enable UWB temporal imaging [22], [24].

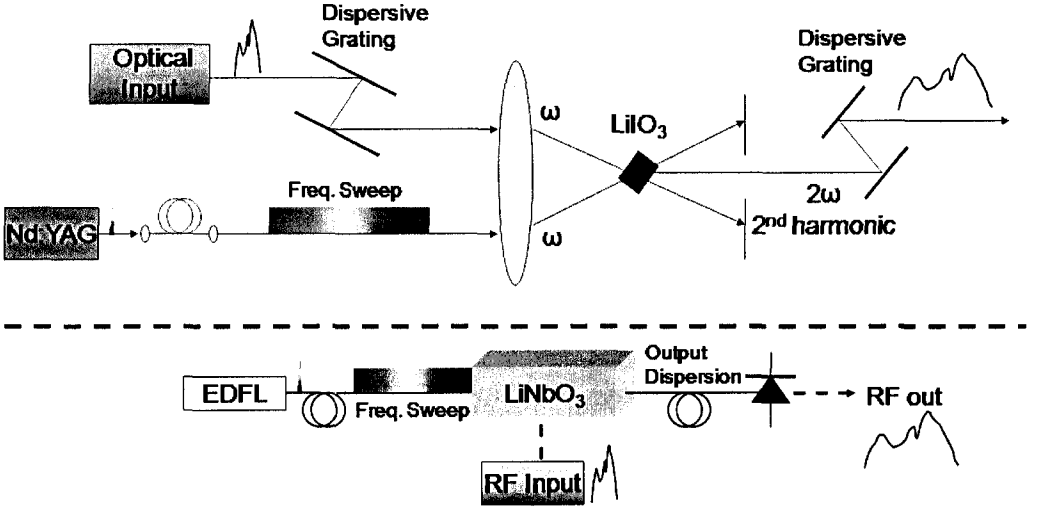

Fig. 4.5 Two optical approaches to temporal imaging. (Top) A purely photonic implementation [19]. A mode-locked Nd:YAG laser pump output is dispersed to yield the reference optical frequency sweep, while diffraction grating pairs are used on the optical input signal. Time lens mixing uses a nonlinear $LiIO_3$ crystal designed for 2^{nd} harmonic generation. (Bottom) A microwave-photonic TI system (microwave traces are dashed) [22]. Time-lens mixing of the RF input and frequency sweep (generated by dispersing the output of a mode-locked erbium-doped fiber laser –EDFL) An electro-optic $LiNbO_3$ modulator. The microwave signal input is not pre-dispersed in this implementation.

An all-optical arrangement (with optical inputs) for temporal imaging by Bennett [19] used optical diffraction grating pairs to introduce the necessary dispersion, and a nonlinear crystal to mix the signal (a 100 Gb/s optical word) with a linearly chirped pump pulse (Fig. 4.5, top) to both time-reverse and slow the signal down to 8.55Gb/s. The use of electro-optical (E-O) modulators as time-

lenses was demonstrated in operation by using $LiNbO_3$ Mach-Zender phase modulators both to generate [5] and to measure [25] picosecond optical pulses. A microwave-input temporal imaging system was subsequently demonstrated by Coppinger [22] in which spools of fiber provided the dispersion and a 12 GHz bandwidth Mach-Zender E-O modulator was used to obtain a magnification factor of 3.25. Coppinger made use of a mode-locked erbium-doped fiber laser to generate the chirped reference and spools containing several km of optical fiber for dispersion (Fig. 4.5, bottom). These electro-optic demonstrations of temporal imaging are noteworthy because they do not feature any dispersion applied to the input waveform – a fact which would normally bring about distortion were it not for the fact that the bandwidth of the chirped reference sweep is much greater than the signal bandwidth [21], [22]. We will elaborate on this specific advantage of photonics in temporal imaging systems in discussion in section 4.2.4. Table 4.2 summarizes some of the experimental demonstrations of temporal imaging in the literature.

Table 4.2
Demonstrations of temporal imaging

Ref	Input Signal	Dispersion	Time Lens; Ref. Sweep Source	Demonstrated Magnification
[17] Caputi	10μs, microwave	Cascaded all-pass networks	Electronic mixer; VCO	2
[21] Azaña	150 ps, optical	Input: none. output: Dispersive optical fiber	$LiNbO_3$ E-O modulator; RF sinusoidal drive	11.45
[2], [19] Bennett	5.7 ps and 40 ps, optical	Diffraction grating pairs	Nonlinear crystal; dispersed impulse	103 and -11.7
[8], [22] Coppinger	3.7 ns and 1 ns, microwave	Input: none. Output: Dispersive optical fiber	E-O modulator; dispersed impulse	-1.85 and 3.25
[26], [27] this work	**1 ns, microwave**	**CEBG microstrips**	**Analog multiplier; dispersed impulse**	**5**

Optical solutions present a considerable challenge from an integration standpoint. Signal conversion to and from the optical domain necessitates electro-optic modulation of some kind, and the referenced works frequently require large spools of optical fiber or costly and difficult-to-operate mode-locked laser sources. Naturally, a fully-electronic and easily integrated system that surpasses these obstacles is desirable.

4.2 An Electronic Time-Magnification System

4.2.1 Dispersion Elements

We began our investigation into electronic TI with the design and demonstration of a 5X electronic time-magnification system [26], [27]. Our work closely followed the scheme proposed and demonstrated by Caputi (Fig. 4.3), and our main task was to make appropriate substitutions to bring this technique into the frequency range of UWB systems.

We employed microstrip CEBG structures to achieve broadband dispersion networks at the signal input and output, which also required equally broadband directional couplers to collect the reflected signals. The choice of microstrip CEBGs gave us implicit frequency boundaries, since structures for reflection below 1 GHz become excessively long (requiring at least a few periods) and frequencies exceeding 20 GHz demanded too much computation time from our simulation software due to the complexity of the mesh used in analysis. Our input signal frequency range was ultimately selected as 2 to 10 GHz (coincidentally similar to the FCC spectral mask for UWB). The choice of 10 GHz as the upper frequency was closely tied to our chosen mechanism for generating the reference chirped frequency sweep: we purchased a -7.5 Volt, 70 ps impulse generator (the Picosecond Pulse Labs 3600, having usable frequency content out to 10 GHz) to be dispersed in a corresponding CEBG line, passively creating a local frequency sweep to be mixed with the input signal in the manner of Fig 4.3. Since this sweep featured a declining amplitude (the natural roll-off of an impulse's frequency content), it was expected to cause some distortion at the system output, however

since this represents an *a priori* source of distortion it was anticipated that this could easily be corrected for in post-processing.

Since our target magnification factor was 5X, the 8 GHz input bandwidth would be reduced to about 1.5 GHz bandwidth at the output, and it would be at a lower center frequency –we set this frequency range to be 1 to 2.5 GHz. It was required to choose the group delay slope of the input CEBG judiciously, due to the necessary tradeoff between the final, realized lengths of the CEBG lines and the time-window over which the system magnification is effective. At the input, a choice of σ_1 = -0.4 ns/GHz with a target magnification factor of $M = -\sigma_3/\sigma_1 = 5$ forces the output dispersion CEBG to be designed for σ_3 = +2 ns/GHz^2. From (4.4) we must set the group delay slope for the reference frequency sweep to be σ_2 = -0.5 ns/GHz – thus, an 8 GHz frequency sweep should occupy about 4 ns in time. The input signal, when dispersed, must be no longer than this reference sweep at most. Since the input group delay slope is -0.4 ns/GHz, we impose a time-window of about 1 ns on the system input. Note that according to the conservative estimate of (4.3) this already imposes a severe limit on the output resolution of the system, which will now at best resolve only a few time-elements (this, in turn, influenced our decision to use digital test inputs).

Our designs for the input and reference-sweep microstrips both operated in the 2-10 GHz band and were 28 cm (meandered) in length, while the output compressive network was designed for operation for the difference frequencies 1-2.5 GHz and was 38 cm in order to have enough periods at these low frequencies to sustain some reflectivity. We fabricated these CEBG designs on Coorstek's ADS-96R alumina substrate (1.27 mm thickness, ε_r = 9.41, tan δ = 0.0007 at 10 GHz), mounted them on custom aluminum baseplates and end-connectorized them to SMA cables. In addition, each was paired with a commercial 6-dB directional coupler of the required bandwidth. Simulated and measured S11-responses (magnitude and group delay) for each CEBG are presented in Fig. 4.6,

[2] This value is very steep for a CEBG and would normally require an extremely long structure. Fortunately, the bandwidth at this output is small (1.5 GHz) and so the structure remains a manageable length: 38 cm.

which were generally found to be in good agreement despite increased ripple in the measured responses (attributable in at least some part to end-connectorization impedance mismatching and fabrication tolerances).

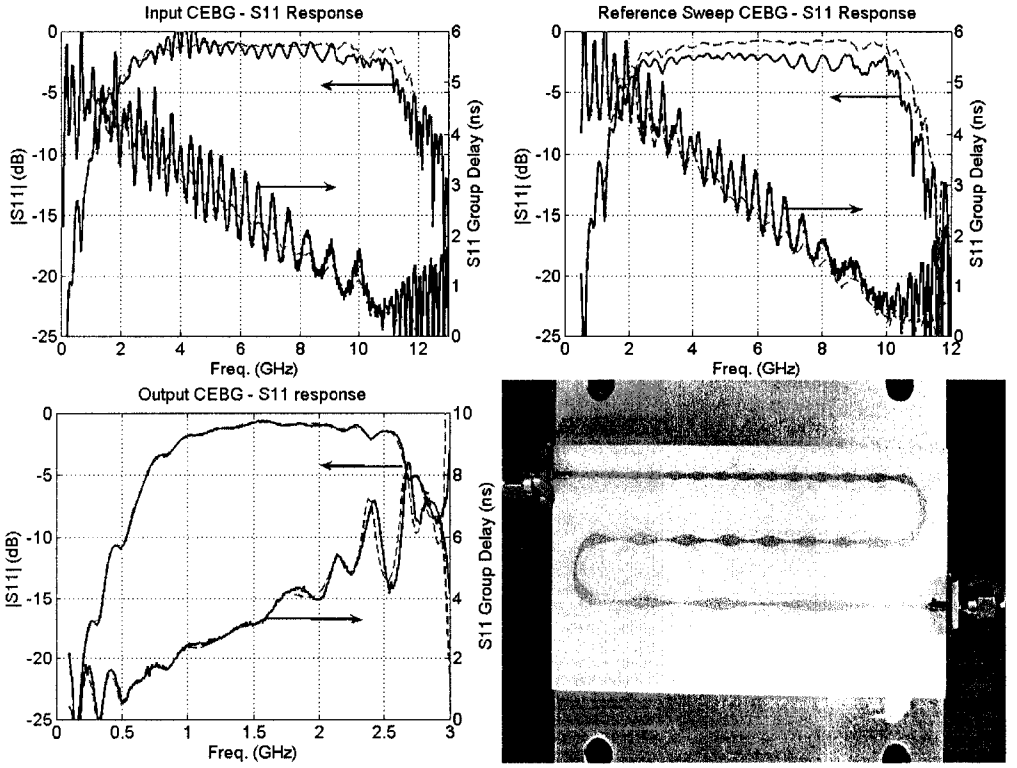

Fig. 4.6. Simulated (dash) and measured (solid) S11 and group delay (reflected port) for each of the CEBG designs in the time-magnification demonstration: (Top-left) the input CEBG; (top-right) the reference frequency-sweep CEBG and (bottom-left) the output compressive CEBG. In general, group-delay ripple and loss are somewhat higher in measurement due to end-connectorization impedance mismatching. (Bottom-right) A photograph of the meandered CEBG for the reference frequency sweep.

With the CEBGs fixed, we turn to the matter of the time-lens: the electronic mixing of the reference frequency sweep with the dispersed input signal.

4.2.2 Electronic Time-Lens

There are several options for performing mixing operations in the electronic domain, ranging from straightforward mixing with a single diode[3] to complex,

[3] One potentially interesting time lens strategy involves using the dispersive network intended for the input signal to also generate the frequency sweep. This requires a slight pre-dispersion of

application-specific multiplier designs. The mechanism for the electronic time lens should reflect the nature of the reference frequency sweep, which we will refer to here for brevity as the local oscillator (LO) even though it is by no means the conventional, single-frequency high-power tone that is traditionally anticipated for this role in a conventional mixer. Our LO was a dispersed impulse taking the form of a low-power (~100mV), short-time (4 ns), chirped frequency sweep from 2 to 10 GHz (of diminishing amplitude towards the higher end), to be mixed with the input dispersed signal in the same frequency range. The output was expected to be in the range of 1 to 2.5 GHz, which partly overlaps the input range, indicating that feed-through of the inputs should be minimized as much as possible. Furthermore, the amplitude of the input signal after several directional coupling operations was a concern and it was desired to provide some amplification. To combine the benefits of an amplifier, mixer and difference-frequency filter in one device, we opted to design our own custom broadband analog multiplier for this purpose. Although it is not the focus of this work and does not represent a novel design, we briefly summarize our design approach in Appendix B and here we present only the bare details.

Our analog multiplier was designed in 0.5-micron SiGe BiCMOS technology and employed a differential Gilbert-cell architecture with predistortion circuitry, following recent broadband analog multiplier designs [28], [29]. A differential topology was chosen for the signal inputs for improved noise immunity and conversion gain. Input signals were brought on-chip using high-frequency probes from Cascade Microtech's Infinity™ series, while a difference-frequency, single-ended output of 1-2.5 GHz was passed off-chip via wirebond through the test board. The design used a +3.3V supply and simple resistive input networks for broadband impedance matching since power consumption was not a concern for this proof-of-concept demonstration (LC ladder networks for broadband

the input impulse, since σ_1 and σ_2 differ only slightly in value for large magnifications according to (4.4). The reference can simply be summed with the signal and passed to a detector diode to perform the mixing. This has the added benefit of partially canceling some of the group delay ripple of the dispersive network [17].

impedance matching would be recommended for a more optimized design). We realized a conversion gain of about +3dB with some gain roll-off for higher difference-frequency products. The output bondpad/wirebond, package and printed circuit board formed a low-pass filter (3-dB cutoff at about 3 GHz) to isolate the difference-frequency (the sum frequencies ranged from 4.5-20 GHz).

4.2.3 Simulation and Measurement Results

The final experimental setup is illustrated in Fig. 4.7. An external 15-dB broadband amplifier at the output of the multiplier stage assisted in compensating for the losses associated with directional coupling and the time-magnification process itself.

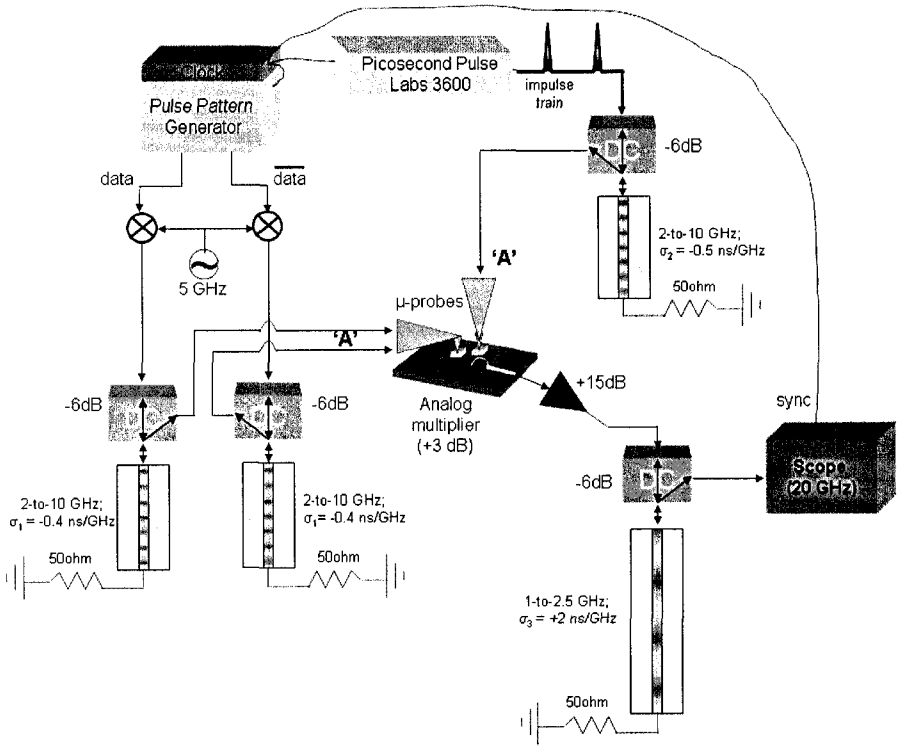

Fig. 4.7 Experimental setup for 5X time-magnification demonstration. Inputs to the analog multiplier are marked with 'A' and displayed in Fig. 4.8.

For test inputs, we chose to work with digital bit-signaling for the ease with which time-windowing could be applied using strings of zeros, and since this is complicit with our system's strict resolution limitations (see section 4.2.1). For example, a simple three-bit sequence '101' at 5 Gbps and 2-Volt amplitude,

generated differentially by our Anritsu MP1763B Pulse Pattern Generator (PPG), fit within the target time-window at 0.6 ns and was upconverted on a 5 GHz carrier using off-shelf diode mixers (most of the upconverted signal's bandwidth fell in a 5 GHz range, or about 100% fractional bandwidth). Differential bit-sequences were padded with zeros to 64-bit length and were sent through a pair of identical microstrip CEBGs and couplers. The signal input and the reference impulse, after dispersion in their respective CEBGs, are shown in Fig. 4.8 as they were passed to the analog multiplier. We observe here that the amplitude of the dispersed reference impulse is nearly flat within the bandwidth of the input signal because only a portion of the full bandwidth was used in this example.

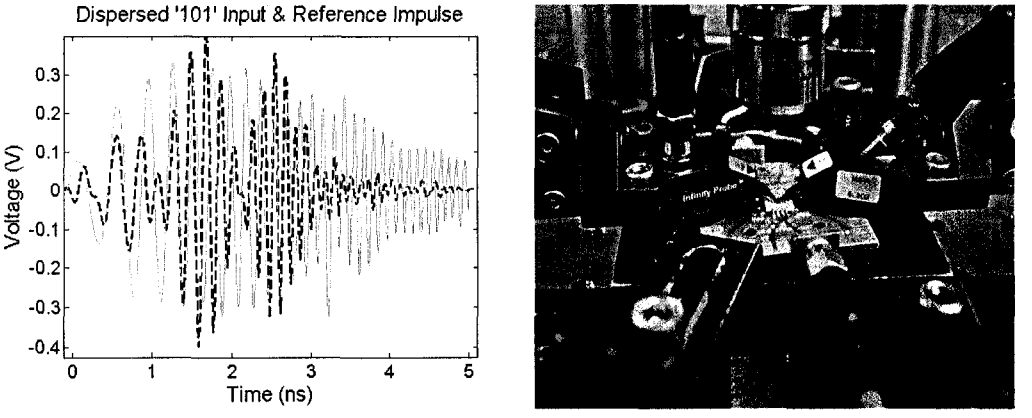

Fig. 4.8. (Left) After being dispersed in their respective CEBG microstrips, this is a snapshot in time of both inputs to the analog multiplier (at point 'A' in Fig. 4.7): a digital '101' test input signal centered at 5 GHz (dash, black) and the impulse (solid, gray). These are the inputs to the multiplier; their timing with respect to each other determines the output frequency difference. (Right) Photograph of the packaged analog multiplier and microprobes.

The impulse was triggered on a 1/64 clock output from the PPG. To ensure that the signal data and reference impulse arrived at the multiplier inputs properly synchronized, coarse timing adjustments were made by looking at the multiplier output for a non-zero product as different bits in the 64-bit stream were toggled. This method of synchronization was coarse (i.e. with a resolution of one bit or 200 ps) but sufficient to demonstrate the temporal imaging principle in operation.

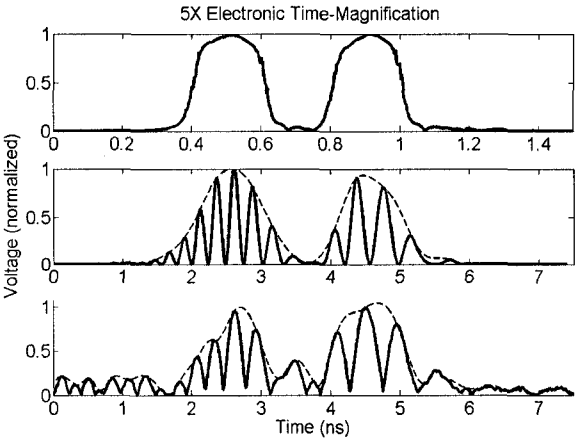

Fig. 4.9. A three-bit '101' test input at 5 Gbps (top, shown from measurement before carrier modulation) and time-magnified outputs from simulation of the microstrips (middle) and from measurement (bottom) with a fivefold change in the x-axis scale. Outputs are normalized absolute values and have envelopes highlighted for visualization purposes

The multiplier product was compressed by the final CEBG microstrip and measured using a Tektronix CSA8000 scope with a 20 GHz electrical sampling module. The measured system output is illustrated in Fig. 4.9 in comparison to the base-band '101' input, as well as simulated results obtained using MatLAB, the extracted microstrip S-parameters (using Agilent's *Momentum*) and ideal multiplication. No post-processing was applied to the measured signal, and the envelope is shown by interpolation (in MatLAB) for illustration purposes. A time-scale factor of 5 has been applied to the time-axis of the normalized outputs to facilitate comparison with the input, and the '101' bit pattern is clearly distinguishable. The measured output amplitude was 140 mV. It is clear that some distortion has taken place which can be attributed to several sources, including the microstrip group-delay ripple, the non-flat frequency responses of the analog multiplier and reference impulse, contributions from mixer/multiplier noise (measurement only), and the effect of using single-sideband processing (i.e. difference-frequency only). Despite none of these elements being optimized, the result is a proof of principle that electronic temporal imaging is feasible in the GHz regime.

It is important in a time-stretch system that the dispersed input signal arrives at the multiplier input at the same time as the reference frequency sweep to obtain

the correct difference-frequency. If part of the input signal is time-shifted away from the ideal timing scenario suggested by Fig. 4.4, two problems occur: a) there may be no component of the reference frequency sweep at the mixer input, or b) the mixer product will be frequency-shifted and fall outside the passband of the subsequent dispersive device. By keeping the reference pulse at a fixed time while advancing the input bit sequence in time, the demonstration system (0.6 ns window, '101' sequence) tolerates approximately 150 ps of temporal misalignment outside this window before one of the input '1' bits becomes about 50% attenuated, as shown in Fig. 4.10 by using MatLAB and measured S-parameter data of the CEBGs to simulate time-delayed inputs. In an experimental observation of the same effect, we present in Fig. 4.10 a measured oscilloscope response to a 6 Gbps bit-pattern of '10101', which is 0.82 ns in length and is just outside the system's temporal aperture. As a result, one of the bits is out of focus, becoming broader and attenuated as a result.

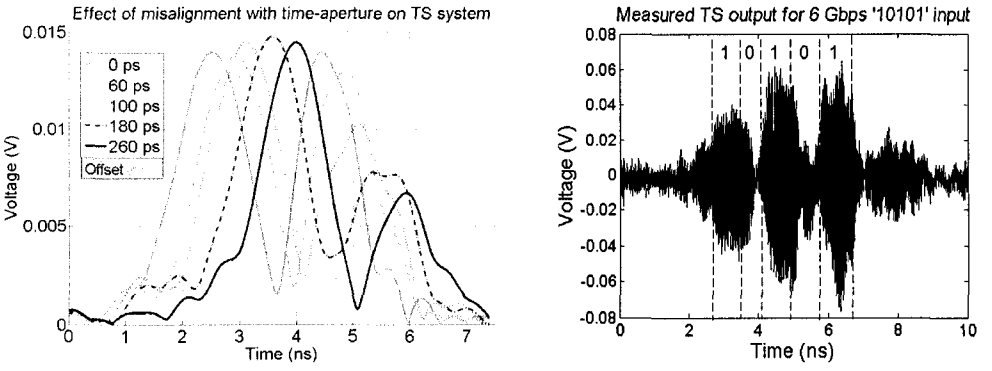

Fig. 4.10 (Left) Temporal misalignment with the time-aperture results in degraded quality of signal envelope. A 150 ps misalignment outside of the 600 ps aperture results in degradation of detected bit-amplitude by over 50%. (Right) Measured system output for a 6 Gbps '10101' bit pattern of 0.82 ns.

4.2.4 Discussion

Here we will discuss several challenges associated with implementing this system entirely in the electrical domain, particularly when contrasted with optical implementations. Photonic systems enjoy several advantages owing to the fact that the optical carrier frequencies are several orders of magnitude greater than the

RF input signal. As mentioned previously, this makes envelope detection at the output extremely simple since the act of photo-detection itself will remove the optical carrier.

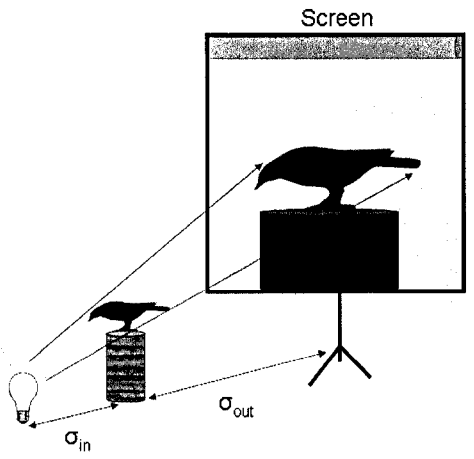

Fig. 4.11 Illustration of the "shadow-casting" analogy for a simplified temporal imaging system

Of significant note is the capacity of a microwave-photonic implementation to be more easily configured for what is referred to in the literature as "simplified" temporal imaging or, alternatively, "photonic time-stretch" [22]-[24]. This refers to system in which the input dispersion is eliminated altogether, which is the equivalent (in imaging terms) of reducing to zero the distance between the object and the lens (i.e. no input diffraction), resulting in a non-focused image at the output. It has been shown that the distortion is negligible if, as described by Azaña *et al.*, the bandwidth of the pulse at the output of the time lens is much larger than the input pulse bandwidth [21]. One popular interpretation of this configuration is "shadow-casting", as depicted in Fig. 4.11.

In a response to our work [27], Conway *et al.* published a reply to elaborate on the distinction between the two situations, although his reply insisted that the simplified imaging system "does not employ phase-modulation or lensing of any kind" [30]. A studied glance at the two systems, presented in Fig. 4.12, shows that in fact the "simplified" system is performing the same kind of mixing of an input waveform against a linear-frequency chirp as the conventional system (i.e. quadratic phase-modulation). This is effectively the action of a time-lens.

What is perhaps non-intuitive, given the "shadow-casting" analogy of Fig. 4.11, is "what has happened to the (analogue of the) lens?" As we responded in our reply to Conway [31], the 'lens-like' property of quadratic-phase modulation is evident in the spherical wavefronts (quadratic phase in the $x^2 + y^2$ sense) emanating from the point source in Fig. 4.11 to illuminate the object, making the

situation analogous to that of a plane-wave input where the object is co-located with a lens.

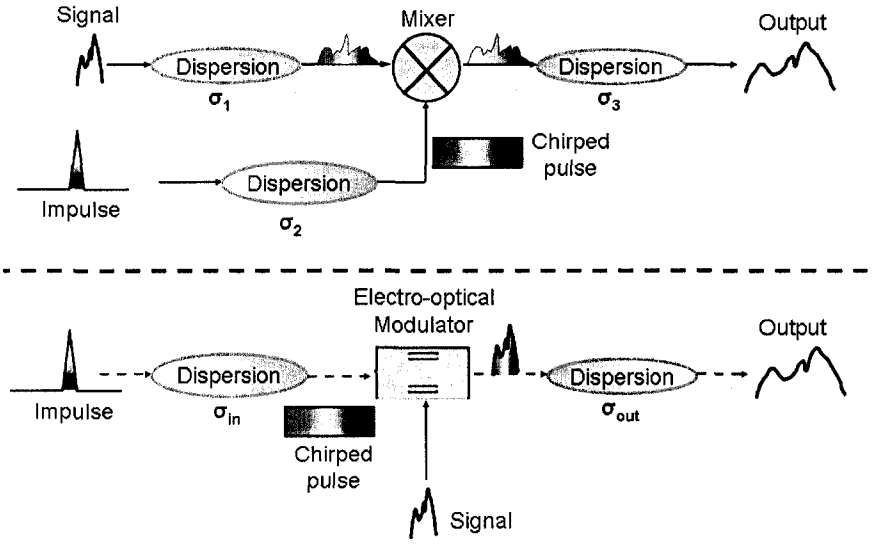

Fig. 4.12 An illustrated comparison of a conventional (top) and "simplified" (bottom) temporal imaging systems (optical traces are dashed). Both systems employ a quadratic-phase modulation in time, but in the simplified case the input has not been pre-dispersed.

The simplified configuration of temporal imaging produces a less restrictive condition for imaging [21]: rather than having to balance an equality of three group delay slope values as in (4.4), the simplified system need only be designed such that:

$$\ddot{\phi}_t >> \frac{\Delta\omega^2}{8\pi} \tag{4.5}$$

where $\Delta\omega$ is the bandwidth of the input signal and $\ddot{\phi}_t$ describes the chirp of the time lens assuming it is a quadratic-phase modulation of the form:

$$m(t) = \exp(j\frac{\ddot{\phi}_t}{2}t^2) \tag{4.6}$$

The temporal resolutions attainable by the simplified and regular implementations are also different, although which approach provides better resolution is largely a function of the target magnification and time window [21].

The problem with this simplified approach for *electronic* implementations is the requirement that the output bandwidth of the time-lens should be at least an

order of magnitude greater than the input bandwidth – which is not a very practical request, since even our demonstrated 8 GHz time-magnification system would necessitate an electronic analog multiplier (to say nothing of an impulse generator) capable of nearly 100 GHz of usable output bandwidth.

As a final point of discussion, we would note that although our demonstration sufficed to show the concept at work, it would be desirable to improve both the time window and the system resolution. This is possible by increasing in magnitude the CEBG group delay slopes (ns/GHz), which in turn requires longer structures for a fixed bandwidth. A method of fine delay control for synchronizing the quadratic phase modulation would also be useful in "focusing" the system output. Also, considering the limitations of having only a few carrier periods both in the input and output, operation at higher frequencies (or using sum-frequencies in mixing) would make it easier to distinguish between the signal envelope and the carrier at the system output.

4.3 Electronic Time-Compression and Reversal Systems

4.3.1 Time-Compression

Despite several recent microwave-photonic demonstrations of the "simplified" temporal imaging (i.e. no input dispersion) system for time-compression [5], [8], [20], there have been as of this writing no experimental demonstrations, in either the microwave or optical regime, of time-compression using the full dispersion-lens-dispersion architecture. Time-compression would be an asset in arbitrary waveform generation (AWG) for broadband signals spanning several GHz, which can be useful in UWB communication schemes. As with the time-magnification system, the drawbacks of this process include a limited resolution, time-window, and an output signal that is modulated on a chirped carrier –although this last point may not be a drawback at all in the context of UWB communication in a dense environment: a correlating receiver could theoretically be designed to scan using a particular chirp to decode transmitted information.

Let us consider as an example a system designed using CEBG tools and assuming that local impulse-generating equipment is limited to 10 GHz. Here,

because we seek a magnification factor of $0 < M < 1$, we observe two things: σ_1 and σ_3 must have the opposite sign (we seek a non-reversed image as before) and now also we require $|\sigma_3| < |\sigma_1|$. According to (4.4), we see that σ_2 must therefore have the opposite sign as σ_1 (i.e. the reference frequency sweep is a down-chirp if the input has been up-chirped) if we are to target the difference-frequency product of the time lens. However, for the sake of curiosity, let us consider a sum-frequency system this time: this has the advantage of a system output with a high carrier frequency, making it easier to discriminate the envelope from the carrier. The switch to sum-frequencies has as a corollary in spatial imaging a switch in the curvature of the lens, resulting in a negative focal length/time – although as Kolner observes in [11] this does not imply the existence of a "virtual temporal image", but rather, a real image being formed by a negative lens: a situation that is not possible with physical lenses since there can be no available change in sign for the process of spatial diffraction. A detailed discussion of sum-frequency vs. difference-frequency temporal imaging is available in [32]. We express the temporal imaging condition for such a system by changing the sign of dispersion in the reference sweep:

$$-\frac{1}{\sigma_2} = \frac{1}{\sigma_1} + \frac{1}{\sigma_3} \tag{4.7}$$

Beginning with a 1.45 ns base-band waveform (we use the pulsed '101' signal again as our test signal) which has approximately 1.5 GHz single-sided bandwidth (SSB), we seek a compressed waveform of 0.48 ns (a compression factor of 3 by setting $M = 0.333$). We will modulate the input on a carrier, which in turn means we will be handling a 3 GHz double-sided bandwidth (DSB) and converting this to a total 9 GHz bandwidth at the output. If we set $\sigma_1 = -1$ ns/GHz, this means our dispersed input will occupy approximately (1.4 ns + 3 GHz · σ_1) = 4.4 ns in the time-domain. This also sets the other CEBG group delay slopes to $\sigma_2 = -0.5$ ns/GHz (recall: in a sum-frequency compression system, σ_2 must share a sign with σ_1), and $\sigma_3 = +0.333$ ns/GHz. We propose the frequency scheme of Fig. 4.13, which establishes that the input RF signal is to be between 12 and 15 GHz to be compressed and upconverted to fit in the 16-to-25 GHz range. The difference

frequencies (5 to 8 GHz) are easily filtered with a high-pass network, and the CEBGs are all reasonable lengths (16.4 cm for the input and output networks, assuming a substrate ε_{eff} of about 7.5).

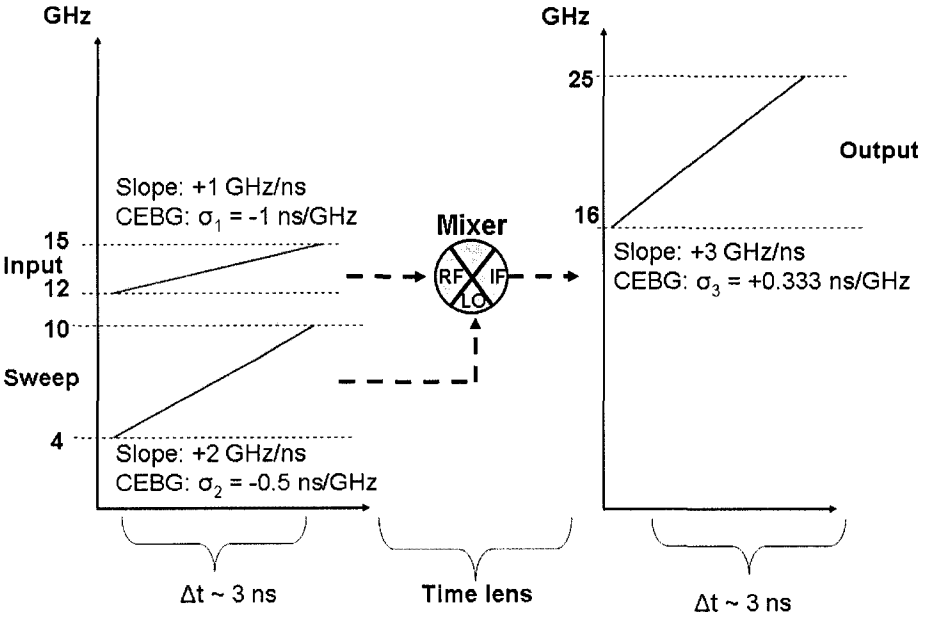

Fig. 4.13 Frequency vs. time representations of the signals in a practical 3X time-compression system, converting a 1.4 ns (1.5 GHz) input waveform into a 9 GHz (double-sideband) output.

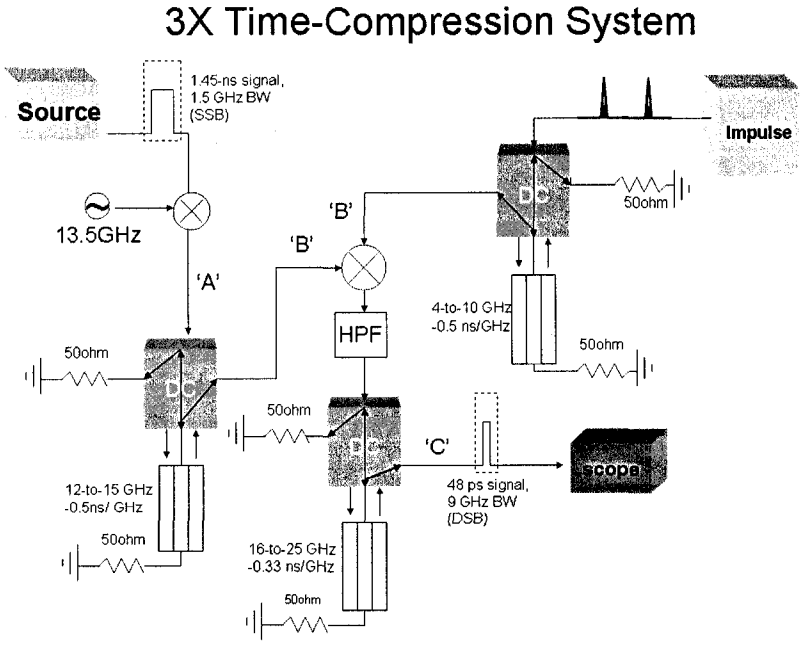

Fig. 4.14. Schematic of the proposed 3X time-compression system, converting a 1.45 ns (1.5 GHz) input waveform into a 9 GHz (double-sideband) output.

The experimental setup for the proposed system takes the form of Fig. 4.14. Although not yet implemented experimentally, we have used MatLAB to predict the expected results of the system [33], showing the signals at each of the labeled points ('A', 'B' and 'C') and assuming ideal quadratic-phase CEBGs and mixing operations, as well as a flat-amplitude reference frequency sweep (DC-to-15 GHz) generated by applying dispersion to a sinc function, thus avoiding the frequency roll-off of a practical impulse for purposes of illustrating the concept.

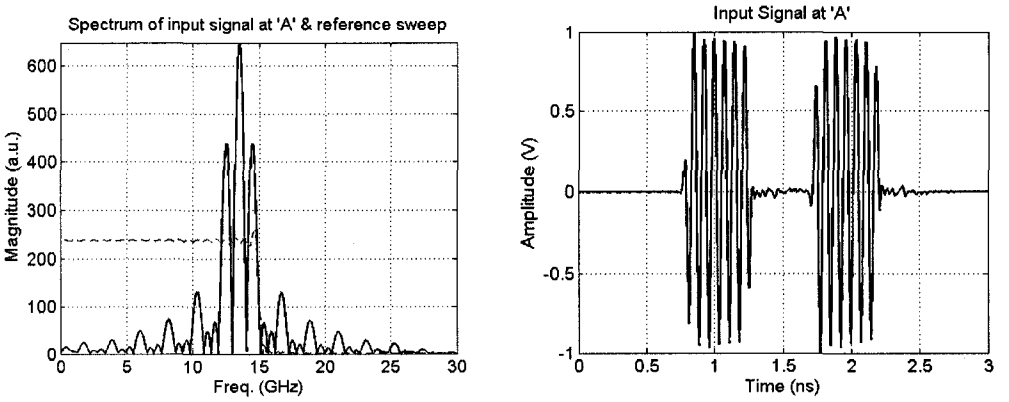

Fig. 4.15. The input '101' signal to the time compression system at point 'A' in the schematic of figure 4.14. in the frequency (left) and time (right, normalized) domains. The spectrum of the reference frequency sweep, generated using an ideal sinc pulse, is also shown (left, dash).

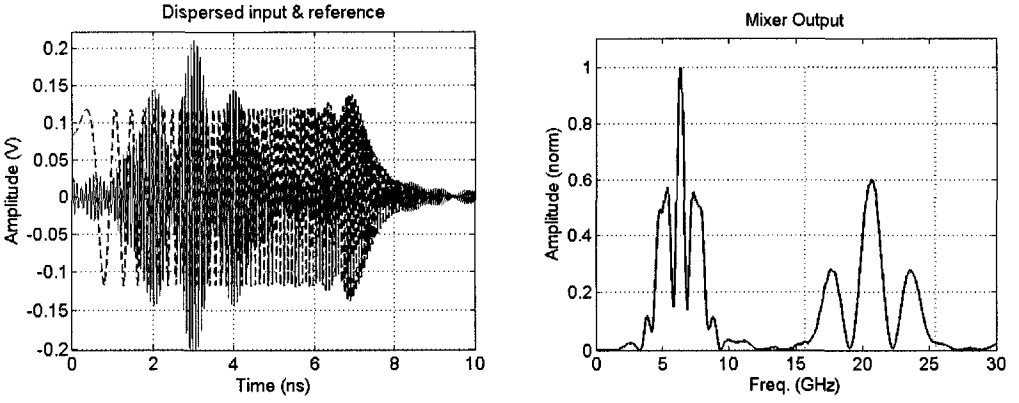

Fig. 4.16. (Left) The dispersed input and reference function at point 'B' from Fig. 4.14, the inputs to the mixer. (Right) the output of the mixer in the frequency domain, with the sum-frequency range within a rectangular bandpass filter from 16-25 GHz.

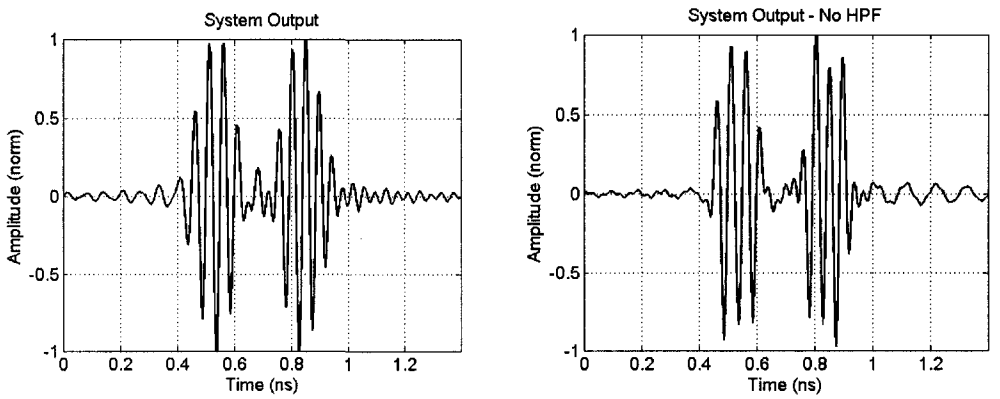

Fig. 4.17. (Left) System output at point 'C' in Fig. 4.14. The '101' pattern remains evident but has lost some sharpness in the filtering process. (Right) The output if no high-pass filtering is applied after mixing: both sum and difference frequencies have contributed.

In figure 4.15, we show the input waveform after up-conversion with the 13.5 GHz carrier in both time and frequency domains, and it spans 1.45 ns. After the first dispersion element, the time-domain waveform is presented in Fig 4.16 aligned with the reference frequency sweep. The product of these signals is shown in the frequency domain where sum and difference frequencies are evident and occupy different bandwidths. When the sum-frequency is band-passed and the difference-frequency rejected (using an ideal, rectangular bandpass filter), the output after the final dispersion is shown in Fig. 4.17 to be 0.53 ns in length –a time-compression factor of 2.8, just shy of the target of 3. The limited system resolution (which can only distinguish a few elements in the original window) still produces a recognizable '101' sequence, although the edges have clearly been rounded, highlighting the loss of detail. This is in part due to the limited bandwidth assumed to be available for the output CEBG. If the output CEBG were assumed to be an all-pass quadratic-phase modulator, the output is somewhat better at retaining the pulse shape (Fig. 4.17, right) since it makes use of the information in both sum and difference frequency outputs.

4.3.2 Time-Reversal

A simple change of dispersion slopes and frequency ranges is enough to modify the simulation to demonstrate microwave time-reversal, which is

potentially interesting for antenna arrays, acoustic and sonar [8]. Here we will target the difference-frequency and set M = -1 by choosing σ_1 = -1 ns/GHz, σ_2 = -0.5 ns/GHz and σ_3 = -1 ns/GHz, respecting the imaging condition (4.4). We use an input signal of 1.45 ns spanning 15-20 GHz and being non-symmetric: in this case, a '101' waveform where the second pulse is twice the amplitude of the first, as presented in Fig. 4.18. We assume the same 15 GHz reference frequency sweep is available. We can see in Fig. 4.19 the output signal has reversed in time, again both with and without an assumed bandpass filter from the final CEBG. The output frequency range here is from 8 to 13 GHz, although this is at the discretion of the designer.

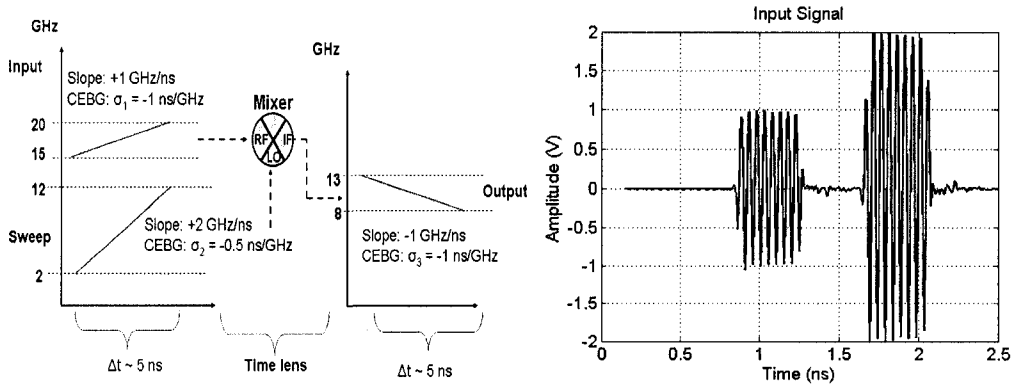

Fig. 4.18. (Left) Frequecy-time representation of the time-lensing process for the time-reversal demonstration. (Right) The input signal for time-reversal.

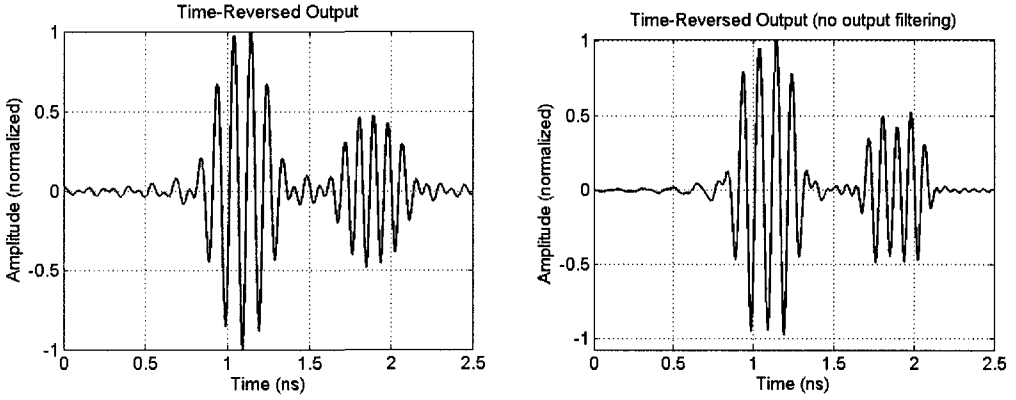

Fig. 4.19. Time-reversed outputs both with (left) and without (right) the assumption of any output bandpass filtering.

4.3.3 Conclusions

In this chapter, we have investigated the application of temporal imaging to systems that are exclusively electronic by handling dispersion using CEBG structures. We experimentally demonstrated the 5X time-magnification of a 0.6 ns time-windowed electronic input, and investigated the limitations of this technique, in particular as compares to photonics-assisted implementations. We also demonstrated how a similar time-compression system could be obtained using the same strategy. Temporal imaging systems for ultra-wideband waveforms with large fractional bandwidths are valuable for applications such as ADC and AWG, and purely electronic implementation could avoid the difficulties of expensive or inconvenient optical hardware associated with these functions.

References

[1] T. Sakano, K. Uchiyama, I. Shake, T. Morioka and K. Hagimoto, "Large-dispersion-tolerance optical signal transmission system based on temporal imaging," Optics Lett., vol. 27, no. 8, pp. 583-5, Apr. 2002.

[2] C. V. Bennett and B. H. Kolner, "Upconversion time microscope demonstrating 103X magnification of femtosecond waveforms," Optics Lett., vol. 24, no.11, pp.783-5, Jun. 1999

[3] Y. Han, O. Boyraz, A. Nuruzzaman and B. Jalali, "Optical header recognition using time stretch preprocessing," Optics Comm., vol. 237, no. 4-6, pp. 333-40, Jul. 2004.

[4] F. Coppinger, A. S. Bhushan, and B. Jalali, "Photonic time-stretch and its application to analog-to-digital conversion," IEEE Trans. Microwave Theory Tech., vol. 47, pp. 1309-1314, July 1999.

[5] A. A. Godil, B. A. Auld and D. M. Bloom, "Time-lens producing 1.9 ps optical pulses," Appl. Phys. Lett., vol. 62, no. 10, pp. 1047-9, Mar. 1993.

[6] X. Chen and S. Kiaei, "Monocycle shapes for ultra wideband system," Proc. IEEE Symp. Circ. Syst., pp. 597-600, May 2002.

[7] M. G. Di Benedetto, L. De Nardis, "Tuning UWB signals by pulse shaping: towards context-aware wireless networks," Signal Processing, vol. 89, no. 9, pp. 2172-84, Sept. 2006.

[8] F. Coppinger, A. S. Bhushan and B. Jalali, "Time reversal of broadband microwave signals," Electronics Lett., vol. 35, no. 15, pp. 1230-2, Jul. 1999.

[9] P. Tournois, "Optical analogy of pulse compression," Annales de Radioélectricité (France), vol. 29, pp. 267-80, Oct. 1964.

[10] A. Papoulis, *Systems and Transforms with Applications in Optics*, New York: McGraw-Hill, 1968.

[11] B. H. Kolner, "Space-time duality and the theory of temporal imaging," IEEE J. Quantum Electron., vol. 30, pp. 1951-63, Aug. 1994.

[12] B. H. Kolner and M. Nazarathy, "Temporal imaging with a time lens," Optics Lett., vol. 14, no. 12, pp. 630-2, Jun. 1989.

[13] A. W. Lohmann and D. Mendlovic, "Temporal filtering with time lenses," Appl. Optics, vol. 31, no. 29, pp. 6212-9, Oct. 1992.

[14] P. Naulleau and E. Leith, "Stretch, time lenses, and incoherent time imaging," Appl. Optics, vol. 34, no. 20, pp. 4119-28, Jul. 1995.

[15] J. van Howe, C. Xu, "Ultrafast optical signal processing based upon space-time dualities," J. Lightwave Tech., vol. 24, no. 7, pp. 2649-62, Jul. 2006.

[16] J. Goodman, *Introduction to Fourier Optics*, Roberts & Co. Publishers, 3rd ed., 2004.

[17] W. J. Caputi, "Stretch: A time transformation technique," IEEE Trans. Aersop. Electron. Syst., vol. AES-7, no. 2, pp. 269-78, Mar. 1971.

[18] C. V. Bennett and B. H. Kolner, "Aberrations in temporal imaging," IEEE J. Quantum Electron., vol. 37, no. 1, pp. 20-32, Jan. 2001.

[19] C. V. Bennett, R. P. Scott and B. H. Kolner, "Temporal magnification and reversal of 100 Gb/s optical data with an up-conversion time microscope," Appl. Phys. Lett., vol. 65, no. 20, pp. 2513-5, Nov. 1994.

[20] J. Azaña, N. K. Berger, B. Levit and B. Fischer, "Broadband arbitrary waveform generation based on microwave frequency upshifting in optical fibers," IEEE J. Lightwave Tech., vol. 24, no. 7, pp. 2663-2675, July 2006.

[21] J. Azaña, N. K. Berger, B. Levit and B. Fischer, "Simplified temporal imaging systems for optical waveforms," IEEE Photon. Tech. Lett., vol. 17, no. 1, Jan. 2005.

[22] F. Coppinger, A. S. Bhushan, and B. Jalali, "Time magnification of electrical signals using chirped optical pulses," Electron. Lett., vol. 34, no. 4, pp. 399-400, Feb 1998.

[23] A. S. Bhushan, F. Coppinger and B. Jalali, "Time-stretched analogue-to-digital conversion," Electron. Lett., vol. 34, no. 11, pp. 1081-3, May 1998.

[24] Y. Han, and B. Jalali, "Photonic time-stretched analog-to-digital converter: fundamental concepts and practical considerations," IEEE J. Lightwave Tech., vol. 21, no.12, pp. 3085-3103, Dec 2003.

[25] M. T. Kauffman, W. C. Banyai, A. A. Godil and D. M. Bloom, "Time-to-frequency converter for measuring picosecond optical pulses," Appl. Phys. Lett., vol. 64, no. 3, pp. 270-2, Jan. 1994.

[26] J. Schwartz, J. Azaña and D. V. Plant, "A fully-electronic time-stretch system," 12th Int. Symp. Antenna Technology and Applied Electromagnetics (ANTEM/URSI), pp. 119-22, Jul. 2006.

[27] J. Schwartz, J. Azaña and D. V. Plant, "A fully-electronic system for the time magnification of GHz electrical signals," IEEE Trans. Microwave Theory Tech., v.55, n.2, pp. 327-34, Feb. 2007.

[28] B. Tzeng, C. Lien, H. Wang, Y. Wang, P. Chao, and C. Cheng, "A 1-17-GHz InGaP-GaAs HBT MMIC analog multiplier and mixer with broad-band input-matching networks," IEEE Trans. Microwave Theory Tech., vol. 50, no. 11, pp. 2564-2568, Nov. 2002.

[29] M. D. Tsai, C. S. Lin, C. H. Wang, C. H. Lien, and H. Wang, "A 0.1-23-GHz SiGe BiCMOS analog multiplier and mixer based on attenuation-compensation technique" Proc. IEEE Radio Freq. Int. Circ. (RFIC) Symp., pp.417-420, 2004.

[30] J. A. Conway, G. C. Valley and J. T. Chou, "Comment on 'a fully electronic system for time magnification of ultra-wideband signals," to appear in IEEE Trans. Microwave Theory Tech., vol. 55, no. 10, Oct. 2007.

[31] J. D. Schwartz, "Reply to comment on 'a fully electronic system for time magnification of ultra-wideband signals," to appear in IEEE Trans. Microwave Theory Tech., vol. 55, no. 10, Oct. 2007.

[32] C. Bennett and B. Kolner, "Principles of parametric temporal imaging - Part I: System configurations," IEEE J. Quantum Electron., vol. 36, no. 4, pp. 430-437, April 2000.

[33] J. Schwartz, J. Azaña and D. V. Plant, "An electronic temporal imaging system for compression and reversal of arbitrary UWB waveforms," submitted to IEEE Radio & Wireless Symp. (RWS 2008), Orlando, FL, Jan. 2008.

CHAPTER 5

Specialty CEBG Designs

In this chapter, we briefly review how phase-shifts can be inserted into bandgap structures to create resonant transmission peaks within the stopband. We extend this idea to describe two techniques for using a CEBG as a multi-frequency resonant filter, transmitting a few narrowband channels within the large stopband. In addition, we discuss the application of the concepts of CEBGs to other media besides microstrip – in particular, stripline and coplanar waveguides which are common microwave transmission lines.

5.1 Multiple-Frequency Resonant CEBGs

It is well-known that by breaking the periodicity of a bandgap structure (e.g. by inserting a local defect or phase-shift), a resonant transmission peak can be inserted within the bandgap as illustrated in Fig. 5.1. This has been demonstrated in fiber Bragg gratings [1] and more recently in microwave bandgap structures as well [2]-[5], where it has attracted attention for resonant antenna design [6]. The presence of this transmission peak can be understood from several points of view. The defect can be interpreted as a section of unperturbed transmission line between two reflectors (i.e. a Fabry-Perot cavity) resulting in a resonance associated with the length (in phase terms) of the cavity. In short, the resonator structure must satisfy:

$$\Phi_{refl1}(f_{res}) + \Phi_{refl2}(f_{res}) + 2 \cdot L \cdot k(f_{res}) = n \cdot 2\pi \tag{5.1}$$

where Φ_{refl} is the phase term introduced upon reflection from one of the resonators[1], L is the length of the transmission line defect, k is the guided wavenumber and n is any integer.

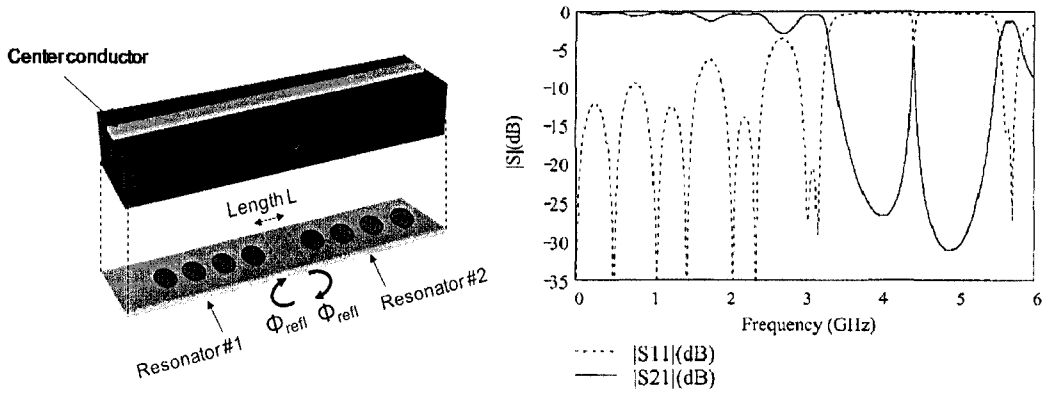

Fig 5.1. (Left) Illustration of a phase-shift inserted in a ground-plane patterned microstrip EBG. (Right) Measurement data taken from [2] demonstrating a resonant cavity at 4.42 GHz.

This interpretation is useful where discretely etched ground circles are concerned, but in a continuous (i.e. sinusoidal) grating there is no need to completely arrest the modulation to achieve this effect – inserting an abrupt local phase-shift is sufficient. In considering the coupled-mode theory, electromagnetic waves that experience Bragg-like reflection from a periodic structure effectively undergo a $\pi/2$ shift each time they reflect. If a direct π phase-shift is inserted in the sinusoidal modulation it will add to the existing π phase-shift experienced by twice-reflected waves at the resonant frequency, constructively supporting a (narrowband) propagating wave.

By using different sizes, locations, and numbers of defects, it has been shown that multiple resonant channels can be created within the bandgap region [5]. A broad stopband with a few transmitting channels may find application as a channelizing filter in communications. The work of [5] relied on placing defects at various points along a single-frequency-tuned EBG based on ground-plan patterning. Another channelizer was demonstrated using defect-insertion include multi-path (branchy) topologies, wherein a microstrip line is divided into several

[1] An analysis of the frequency-dependence of this reflective phase-shift for metallodielectric periodic structures is available in [7].

paths of differing lengths over an EBG-infused ground plane [8]. Unfortunately, the channels demonstrated in [5] and [8] exhibited generally poor performance: insertion losses in excess of 10 dB and stopband widths below 3 GHz. In the work of Kee *et al.* [9], a drop-filter structure was created wherein different channels could be isolated at dedicated ports. The drop-filter approach involves junctions along a microstrip, each leading to 1-D EBG structures interrupted by a chosen defect, thus passing a different channel down each branch. Naturally, this consumes significant board area for multi-channel operation since it requires a dedicated EBG for each dropped frequency.

An extension of the defect-insertion technique is possible with chirped EBG structures in which we will demonstrate broader bandwidths, more channels and higher transmission peaks than previous demonstrations.

5.1.1 Phase-Shifted CEBGs

Instead of inserting different sizes of defects into a single-frequency EBG pattern, it is a simple matter to introduce the same kind of defect (a local π phase-shift in the transmission line perturbation) into a structure whose local period is continually evolving. We demonstrated that this approach dramatically improves channel transmission and stopband bandwidth while reducing the number of etching steps required to one, since the EBG is written in the conductor strip instead of the ground plane [10].

At any location z_{res} along the structure, a resonant channel at the local frequency $\omega(z_{res}) = 2\pi/a_o + 2Cz_{res}$ can be obtained by adding a π phase-shift to the impedance modulation expression (2.4). Each inserted π-shift thus corresponds to one local frequency[2]. Many channels can be inserted within a single chirped structure. A four-channel device is demonstrated in our work [10], where we used in (2.4) the design values of (A = 0.24, C = -1600 m^{-2}, L = 18.9 cm, f_o = 7 GHz) and created the pattern on an alumina substrate. We placed four evenly-spaced π-shifts along the length of line. The actual-size microstrip top conductor pattern is illustrated in Fig. 5.2, which clearly shows the four local phase-shifts. Simulated

[2] Other phase-shifts besides π may be used, the effect of which is to translate the resonance peak away from the local frequency.

(using MoM) and measured (using a VNA) $|S_{11}|$ and $|S_{21}|$ responses are presented in Fig. 5.3, where we also included a structure missing the third phase-shift to show the absence of the corresponding channel. The results show a very close agreement, with an inter-channel spacing of about 1.1 GHz and insertion losses of about 2-3 dB in each channel.

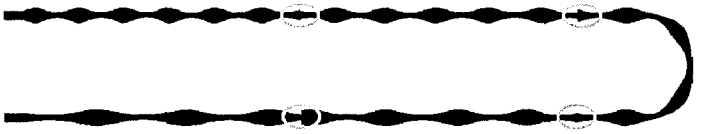

Fig. 5.2. Four-channel phase-shifted microstrip, 18.9 cm long, with channels at 5.35 GHz, 6.45 GHz, 7.5GHz and 8.6 GHz. The meandered shape of the structures was to fit a 10 cm etching process – this representation shown here is approximately actual size.

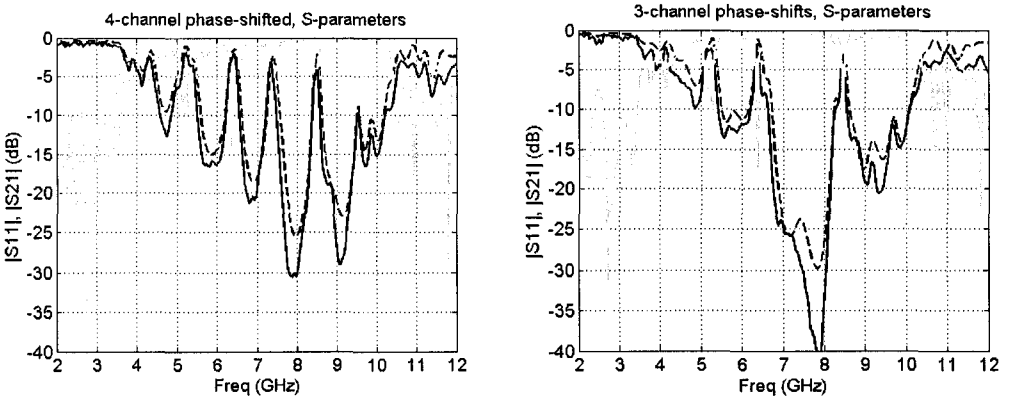

Fig. 5.3. $|S_{11}|$ (grey) and $|S_{21}|$ (black) data from simulation (dash) and measurement (solid) for chirped EBG structures. (Left) Four evenly distributed local π phase-shifts (A = 0.24, C = -1600 m^{-2}, L = 18.9 cm, f_o = 7 GHz). (Right) The same structure with one phase-shift removed.

One standard figure of merit for a resonant channel is the Q factor, defined = as the ratio between the resonant frequency and the 3-dB bandwidth of the channel: $Q = f_{res}/\Delta f_{3dB}$. Our results suggest a Q value of about 50-60 for each channel (3-dB bandwidths of about 150 MHz). The depth of channel isolation (the difference between the transmission peak and the neighboring valley), varies from 8 to 22 dB and generally improves towards the higher frequencies – this is characteristic of linear CEBG structures, which have fewer periods at low frequencies and therefore weakening reflectivity, although asymmetric tapering windows can offer some compensation for this effect.

5.1.2 Moiré-Patterned CEBGs

In the context of optical FBGs, fabrication difficulties surrounding the insertion of abrupt phase-shifts into gratings spurred the development of an alternative approach for generating local π phase-shifts: the chirped superposition or "Moiré" structure [11]. Chirped Moiré gratings in optical fiber attracted attention for applications in sensing [12], wavelength-division multiplexing and optical code-division multiple-access technologies [13].

It was recognized early on that EBGs in microstrip could be superimposed rather than concatenated to design for several frequency ranges in one structure [14]. Extending this, two sinusoidal patterns with the same chirp but different central frequencies can be superimposed. The resulting structure is also chirped and contains evenly-spaced crossover points or "beats", where the phase-shift naturally changes by π and achieves the same resonant transmission effect described in the previous section. We can implement this in microstrip by modifying (2.4) to feature two unique central (z = 0) periods a_{o1} and a_{o2} corresponding to the central Bragg frequencies f_{o1} and f_{o2} of two independent stopbands:

$$Z_0(z) = 50 \cdot \exp\left[A \cdot \left[\sin\left(\left(\frac{2\pi}{a_{o1}} + C \cdot z\right) \cdot z - C\frac{L^2}{4} \right) + \sin\left(\left(\frac{2\pi}{a_{o2}} + C \cdot z\right) \cdot z - C\frac{L^2}{4} \right) \right] \right] \tag{5.2}$$

If the two EBG periods are relatively close, the realized stopband will be slightly wider than that of each individual chirped pattern and will be spectrally centered between the two center Bragg frequencies. A 'fast' and 'slow' envelope can be identified:

$$a_{fast} = 2\left| \frac{1}{a_{o1}} + \frac{1}{a_{o2}} \right|^{-1} \qquad a_{slow} = 2\left| \frac{1}{a_{o1}} - \frac{1}{a_{o2}} \right|^{-1} \tag{5.3}$$

The slow-envelope a_{slow} does not change along the length of the structure since the identical chirp in both CEBGs maintains the same frequency-difference – this is the beat frequency. The frequency-spacing between resonant transmission peaks is determined by:

$$\Delta f = \frac{c}{4\pi\sqrt{\varepsilon_{eff}}} \cdot C \cdot a_{slow} = \frac{c}{2\pi\sqrt{\varepsilon_{eff}}} \cdot C \cdot \frac{a_{o1} \cdot a_{o2}}{|a_{o1} - a_{o2}|} \tag{5.4}$$

An illustration of a Moiré structure with four "beats" is presented in Fig. 5.4, plotted using microstrip widths, and shown realized in Fig. 5.5.

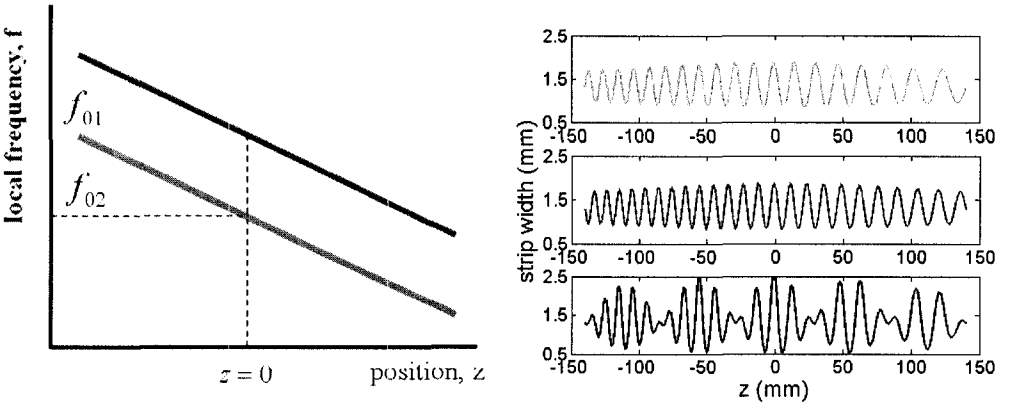

Fig. 5.4. (Left) Frequency vs. position graph of two independent CEBGs with the same chirp but differing central frequencies. (Right) Illustration of the summation of the two CEBGs. Y-axis contains realized widths of microstrip on an alumina substrate.

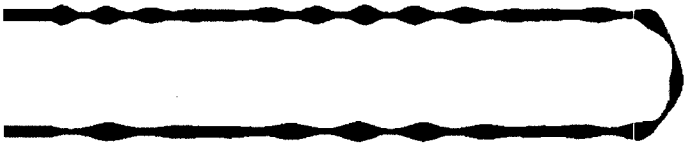

Fig. 5.5. Four-channel chirped Moiré microstrip, 18.9 cm long, shown approximately actual size.

The integer number of channels (beats) 'n' obtained is dependent on the length of the structure:

$$n = 2 \cdot \mathrm{int}\left(\frac{L}{2} \cdot \frac{|a_{o1} - a_{o2}|}{a_{o1} \cdot a_{o2}}\right) \tag{5.5}$$

Unlike the direct phase-shift insertion technique, these channels are by default evenly-spaced within the bandgap. We demonstrated in [10] some simulation and experimental results for a 4- and 6-channel Moiré CEBG in microstrip that exhibited close agreement. The designs both used the values A = 0.14 and C = -1718 m^{-2} in (5.2) and the same *average* center frequency but different spacing between f_{o1} and f_{o2}: a four-channel device used central frequencies 6.12 and 7.96 GHz, whereas a six-channel implementation used 6.12 GHz and 8.27 GHz, reducing the inter-channel frequency separation to 750 MHz

from 1 GHz. As shown in Fig. 5.6, this achieves a slightly broader but shallower rejection band than with the phase-shifting method, resulting in slightly reduced depth of isolation. The Q factor of the established channels varied from channel to channel, reaching as high as 100 for some but as low as 30 for others. There was also some variation in the transmission peak amplitude, which tended to reduce towards higher-frequencies where losses are higher, and the channel isolation, which worsened towards the lower frequencies where there were not as many periods. The channel isolation can be improved by increased the depth of modulation (as controlled by the A value) without significantly altering the transmission peaks, as shown in Fig. 5.7.

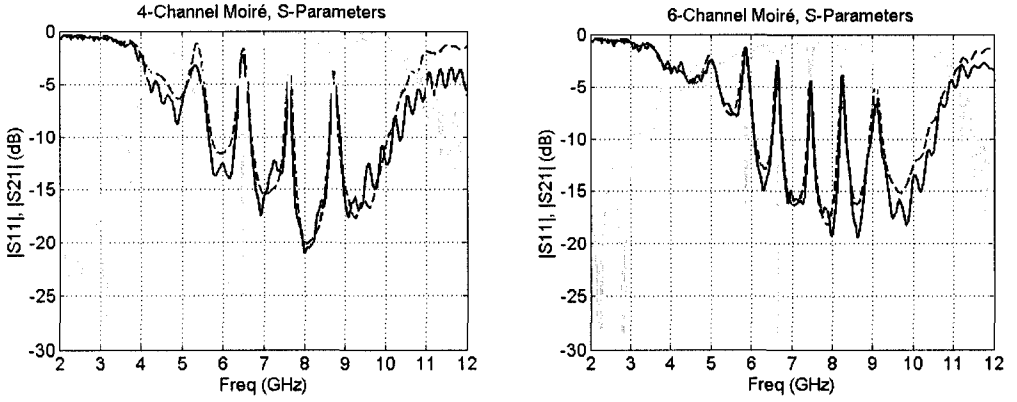

Fig. 5.6. (Left) S11 (grey) and S21 (black) data from simulation (dash) and measurement (solid) for a four-channel 18.9 cm Moiré CEBG structure having f_{o1}=6.43 GHz & f_{o2}=7.96 GHz. (Right) data for the same structure having instead f_{o1}=6.12 GHz, f_{o2}=8.27 GHz, yielding six channels, although one exhibits poor isolation.

We conclude by noting that while the local-phase-shift approach offers the flexibility of channel location since phase-shifts can be applied anywhere, the Moiré method favors broader, shallower stopbands and exhibits a less rippled response due to smoother impedance profiles. Ultimately, both techniques yield far better insertion losses than previously reported bandgap-filter techniques for multi-frequency channelization [5], [8]. Design challenges include weighing the difficulty of longer structures not having sufficient channel isolation at low frequencies, and of having too much insertion loss at high frequencies due to increased conductor and dielectric losses.

	A=0.10	A=0.12	A=0.14
Z_{o_min} (Ω)	41.27	39.72	38.23
Z_{o_max} (Ω)	60.88	63.33	65.87
W_{max} (mm)	1.85	1.98	2.11
W_{min} (mm)	0.84	0.76	0.69

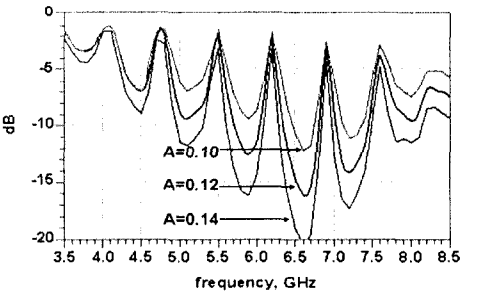

Fig. 5.7. Six-channel structure simulated for different depths of modulation (corresponding min/max impedances and strip widths are shown in table).

5.2 CEBGs in Other Media

The demonstrations of this work have taken place exclusively in microstrip technology, primarily since it is simple to design, fabricate and connectorize. The principles of CEBG design, however, can be extended into any transmission line or waveguiding structure in which the characteristic impedance can be modulated to achieve a target coupling coefficient between forward and backward propagating modes. Transmission technologies that are popular in the microwave range include stripline, coplanar waveguide, ridge waveguide, coaxial line, and many more. Although it would be redundant to describe them all, a few are significant for the improvements they may offer in size and integration of future designs.

5.2.1 Stripline

As a quasi-TEM environment for waves, microstrip lines bear a significant portion of the propagating wave's field structure in the air, resulting in an effective permittivity ε_{eff} that is lower than that of the substrate material. As expressed in (2.8), lower permittivities result in longer CEBG structures. By burying a CEBG in a stripline configuration (Fig. 5.8), a true TEM mode is supported using the material's intrinsic permittivity, and the corresponding structures will be both shorter and narrower in width, although more lossy than equivalent microstrip lines.

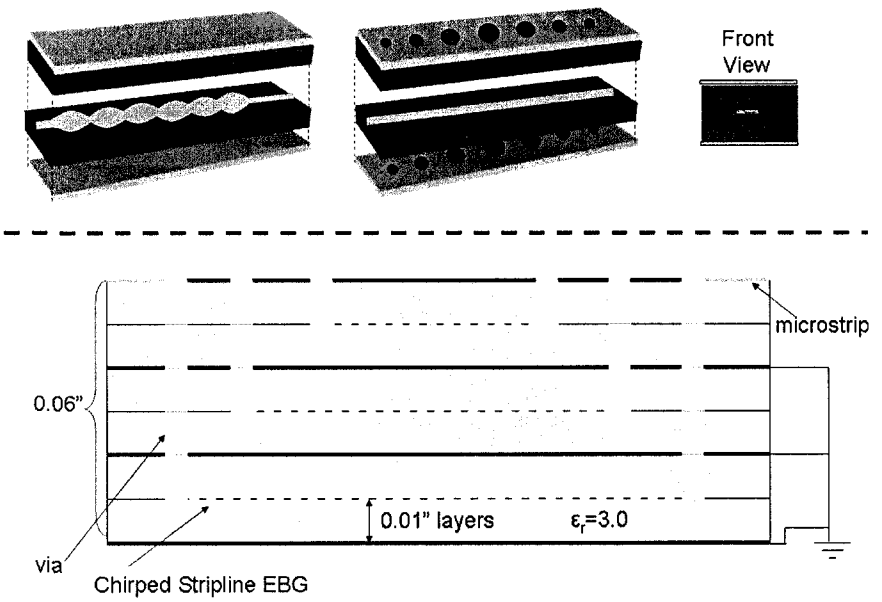

Fig. 5.8. (Top) Possible stripline CEBG implementations –a modulated strip width and a pattern of etched ground plane circle- with a front view of the conventional stripline E-field orientation. (Bottom) Side view cutaway of a stacked-stripline design with three CEBG lines, using microstrips at the top layer to bring the signal to the board edge.

An innate advantage to stripline designs is that it they are stackable in a compact way, unlike microstrips, which much be spaced far apart to avoid crosstalk. In Fig. 5.8 a simple scheme is illustrated to fit three CEBG designs physically above each other in a seven-metal-layer process. The intervening ground planes ensure that crosstalk is absent between the lines, and the modulation can be written in the strip itself rather than the ground planes to isolate each bandgap pattern. The difficulty associated with this strategy is in switching layers: the discontinuities created by vias are inhospitable for ultra-broadband design in the GHz range, and there is further risk of exciting undesired parallel-plate modes[3].

There exists very little research into stripline bandgap structures at the time of this writing and no practical demonstrations yet exist to the author's knowledge. Simulations have been conducted using finite-difference time-domain (FDTD)

[3] Ironically, 2-D EBGs have been proposed as a solution to suppress just such parallel plate modes in multi-layer designs [15].

analysis on rectangular ground-plane etches and another approach, periodic partial-vias, were presented in [16]. Using the standard curve-fitting synthesis equations for stripline [17], we designed and simulated a stripline CEBG with a modulation in the strip-width. Included in our simulation were plated via through-holes connecting the stripline CEBG to a 50-ohm microstrip on the top layer for the purposes of edge-connectorizing the final structure. Our simulation results, presented in Fig. 5.9, suggested fair performance as long as an array of ground-bearing vias are used to encircle the main via – this is the "co-axial via" technique proposed in [18]. Our simulation assumed layers of 0.008" (0.2 mm) Rogers 4403 material were used (ε_r = 3.5, tan δ = 0.0027) and 1 oz metal layers of copper. Although we also fabricated the 10 cm stripline of this design, very poor matching between our edge-coupled SMA-type connectors and the microstrip mode of such a thin board resulted in extremely poor measurement results (even for a simple 50-ohm stripline, reflectivity was very high across the band), leading us to suspect that a better connectorization strategy would be to use vertical coupled SMA connectors (whose pins would go directly into the vias) and forego the microstrip entirely, or else pursue a true edge-connected stripline by press-fitting the layers around a tab contact lead to an SMA.

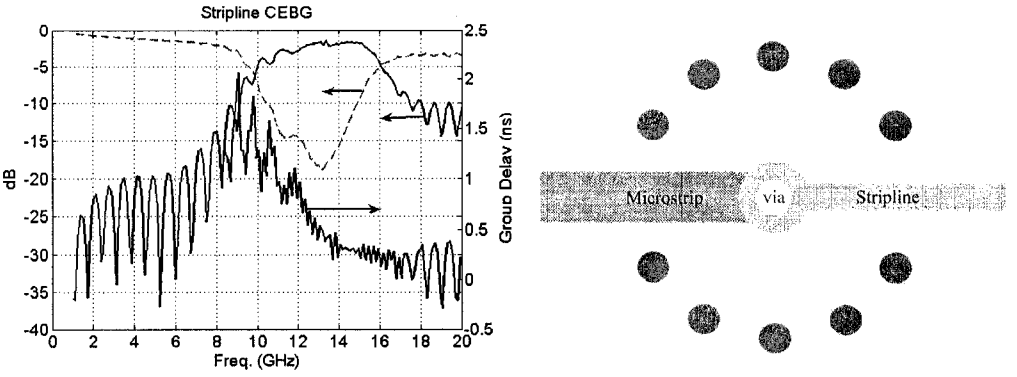

Fig. 5.9. (Left) Simulation of a stripline CEBG |S11| (solid, left axis), |S21| (dash) and reflection-mode S11 group delay (solid, right axis). (Right) Illustration of the microstrip-stripline junction with center via and ten supporting ground vias.

5.2.2 Coplanar Waveguide

Compared to stripline, significantly more research efforts have investigated coplanar waveguide (CPW) implementations of EBGs, which put the ground-

plane on either side of a center conductor, making them extremely convenient for fabrication. CPW-oriented CEBG structures can also be made shorter than conventional microstrip implementations because the effective permittivity can be increased artificially using slow-wave design techniques [19]. Although many designs exist for creating good bandgap behavior by using clever resonator structures [20], it is not yet obvious how well these techniques might be extended to chirped structures, for which there is no consistent "unit-cell" since they are not strictly periodic.

Using closed-form synthesis equations valid up to 20 GHz [21], we designed a simple CPW CEBG structure with a sinusoidal pattern that was 12.7 cm in length on a 0.6-mm-thick Rogers 4403 substrate by varying the center strip width while maintaining its distance to the accompanying ground planes. The results, presented in Fig 5.10 along with a photograph of the structure, show some agreement and proper bandgap behavior but a problematic amount of ripple in the measurement that is generally attributed to poor matching at the soldered SMA connections. Transitioning to and from various types of transmission line is obviously an art in and of itself, and optimizing it for broad bandwidths is likely to require new designs.

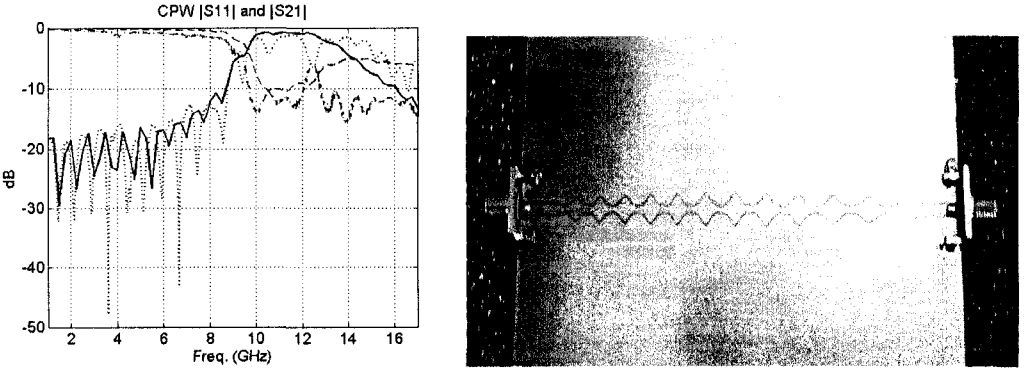

Fig. 5.10. (Left) Simulation and measurement of a CPW CEBG |S11| (solid: simulation, dot: measurement) and |S21| (dash: simulation, dash-dot: measurement). (Right) Photograph of the CPW CEBG.

5.2.3 Other Media

Where high-frequency microwave and mm-wave applications are concerned, transmission lines suffer from increased losses and the problem of crosstalk in

densely populated environments. Waveguide-based interconnects in a circuit substrate are a popularly explored solution, and here EBG structures are also poised to make an impact. There is a growing interest in modifying rectangular waveguides with a periodic array of vertical conducting posts or vias to induce bandgap behavior [22], [23]. By periodically drilling and plating two "fences" of vias through a simple parallel-plate structure, a virtual metal sidewall is created along the fenced-in region in which a TE_{10} mode can potentially propagate [24]. Work in this field is just beginning and it is anticipated that many novel designs will emerge in the next few years.

5.2.4 Conclusions

In this chapter we have seen demonstrations of how CEBGs can be used for their transmission properties as well: as multi-frequency channelizers. We presented demonstrations of 4- and 6-channel filters using two different techniques: defect-insertion and Moiré patterning. We have also explored the potential for CEBGs to be developed in a wide variety of media of interest to the microwave and mm-wave community.

References

[1] G. P. Agrawal and S. Radic, "Phase-shifted fiber Bragg gratings and their application for wavelength demultiplexing," IEEE Photon. Tech. Lett., vol. 6, no. 8, pp. 995-7, Aug. 1994.

[2] T. Lopetegi, F. Falcone and M. Sorolla, "Bragg reflectors in microstrip technology based on electromagnetic crystal structures," Int. J. Infrared and Millimeter Waves, vol. 20, no. 6, pp. 1091-102, Jun. 1999.

[3] F. Falcone, T. Lopetegi, M. A. G. Laso and M. Sorolla, "Novel photonic crystal waveguide in microwave printed-circuit technology," Microw. Opt. Tech. Lett., vol. 34, no. 6, pp. 462-6, Sept. 2002.

[4] M. Bouzouad, A. Saib, R. Platteborze, I. Huynen, and R. Aksas, "Defect modes in microstrip lines on electromagnetic bandgap substrates of finite extent," Microw. Opt. Tech. Lett., vol. 48, no. 1, pp. 144-50, Jan. 2006.

[5] A. Griol, D. Mira, A. Martinez and J. Marti, "Multiple-frequency photonic bandgap microstrip structures based on defects insertion," Microw. Opt. Tech. Lett., vol. 36, no. 6, pp. 479-481, March 2003.

[6] C. Cheype, C. Serier, M. Thèvenot, T. Monédière, A. Reineix and B. Jecko, "An electromagnetic bandgap resonator antenna," IEEE Trans. Antennas Propag., vol. 50, no. 9, pp. 1285-90, Sept. 2002.

[7] M. Golosovsky, Y. Neve-Oz, D. Davidov, and A. Frenkel, "Phase shift on reflection from metallodielectric photonic bandgap materials," Phys. Rev. B, vol. 70, no. 11, pp. 115105-1-10, Sept. 2004.

[8] Y. Li, H. Jiang, L. He, H. Li, Y. Zhang and H. Chen, "Multichanneled filter based on a branchy defect in microstrip photonic crystal," Appl. Phys. Lett., vol. 88, Feb. 2006.

[9] C.-S. Kee, I. Park and H. Lim, "Photonic crystal multi-channel drop filters based on microstrip lines," J. Phys. D (Appl. Phys.), vol. 39, no. 14, pp.2932-4, Jul. 2006.

[10] J. Schwartz, Michael M. Guttman, J. Azaña and D. V. Plant, "Multi-channel filters using chirped bandgap structures in microstrip technology," IEEE Microwave Compon. Lett., v. 17, no. 8, pp. 577-9, Aug. 2007.

[11] L. Zhang, K. Sugden, I. Bennion and A. Molony, "Wide-stopband chirped fibre moiré grating transmission filters," Electron. Lett., vol. 31, no. 6, pp. 477-9, Mar. 1995.

[12] A. M. Gillooly, L. Zhang and I. Bennion, "Quasi-distributed strain sensor incorporating a chirped Moiré fiber Bragg grating," IEEE Photon. Tech. Lett., vol. 17, no. 2, pp. 444-6, Feb. 2005.

[13] L. R. Chen and P. W. E. Smith, "Tailoring chirped Moiré fiber Bragg gratings for wavelength-division multiplexing and optical code-division multiple-access applications," Fiber Integr. Opt., vol. 19, no. 4, pp. 423-37, Oct. 2000.

[14] M. A. G. Laso, T. Lopetegi, M. J. Erro, D. Benito, M. J. Garde and M. Sorolla, "Multiple-frequency-tuned photonic bandgap microstrip structures," IEEE Microwave Guid.Wave Lett., vol. 10, no. 6, pp. 220-2, June 2000.

[15] K. P. Ma, J. Kim, F. R. Yang, Y. Qian and T. Itoh, "Leakage suppression in stripline circuits using a 2-D photonic bandgap lattice," IEEE MTT-S Int. Microw. Symp. Dig., vol. 1, pp. 73-6, Jun. 1999.

[16] M. S. Tong, R. Sauleau, V. Krozer, Y. Lu, "Numerical studies of stripline-typed photonic band-gap (PBG) structures using finite difference time domain (FDTD) method," J. Comput. Electron., vol. 5, no. 1, pp. 53-61, Mar. 2006.

[17] D. M. Pozar, *Microwave Engineering*, 3rd ed., John Wiley & Sons, 2004.

[18] E. R. Pillai, "Coax via – a technique to reduce crosstalk and enhance impedance match at vias in high-frequency multilayer packages verified by FDTD and MoM modeling," IEEE Trans. Microwave Theory Tech., vol. 45, no. 10, pp. 1981-5, Oct. 1997.

[19] H. Kim and R. F. Drayton, "Size reduction method of coplanar waveguide (CPW) electromagnetic bandgap (EBG) structures using slow wave design," Top. Meet. Silicon Monolithic Integr. Circ., pp. 191-4, Jan. 2007.

[20] S. G. Mao, and Y. Z. Chueh, "Coplanar waveguide bandpass filters with compact size and wide spurious-free stopband using electromagnetic bandgap resonators," IEEE Microwave Compon. Lett., vol. 17, no. 3, pp. 181-3, Mar. 2007.

[21] T. Q. Deng, M. S. Leong, P. S. Kooi and T. S. Yeo, "Synthesis formulas simplify coplanar-waveguide design," Microw. RF (USA), vol. 36, no. 3, pg. 84, Mar. 1997.

[22] K. Yasumoto, N. Koike, H. Jia, and B. Gupta, "Analysis of electromagnetic bandgap based filters in a rectangular waveguide," IEICE Trans. Electron., vol. E89-C, no. 9, pp. 1324-9, Sept. 2006.

[23] S. W. H. Tse, A. Karousos and P. R. Young, "Broadband photonic bandgap waveguides," IEEE MTT-S Int. Microw. Symp. Dig., vol. 3, pp. 2063-6, Jun. 2004.

[24] A. Suntives and R. Abhari, "Design and characterization of the EBG waveguide-based interconnects," IEEE Trans. Adv. Packaging, vol. 30, no. 2, pp. 163-70, May 2007.

CHAPTER 6

Conclusions

6.1 Summary

The CEBG structures proposed in this work represent in many ways an interdisciplinary breakthrough: the scaling of the concepts and applications of dispersive gratings in optical regime down to the microwave frequency range. They emerge at a time during which promising UWB systems are challenging RF designers to design for large fractional bandwidths in the GHz regime. As a tool for introducing broadband signal dispersion, CEBGs fill a gap in the frequency spectrum between the (predominantly) sub-GHz domain of chirped SAW structures and the THz domain of fiber-optics. The ease of fabrication and integration of CEBG structures in familiar technologies such as microstrip and stripline make them an attractive tool for signal processing techniques that can benefit from dispersion.

In Chapter 1 we identified a number of sub-systems for which high-bandwidth processing poses a challenge: real-time spectral analysis, tunable time-delay, analog-to-digital conversion, and arbitrary waveform generation. After briefly reviewing the development of the CEBG structure in Chapter 2, we demonstrate how it (and by extension, dispersion) can be deployed to generate real-time Fourier transforms (Chapter 2), yield continuously tunable delays for broadband waveforms (Chapter 3), and produce temporally magnified and compressed replicas of signals for ADC and AWG applications (Chapter 4). We also discussed specialty CEBG designs for multi-frequency resonance, and investigated a variety of media in which CEBGs are feasible (Chapter 5). We summarize in Fig. 6.1 the work described in this thesis, the relevant publications, and the ultimate application of each demonstration.

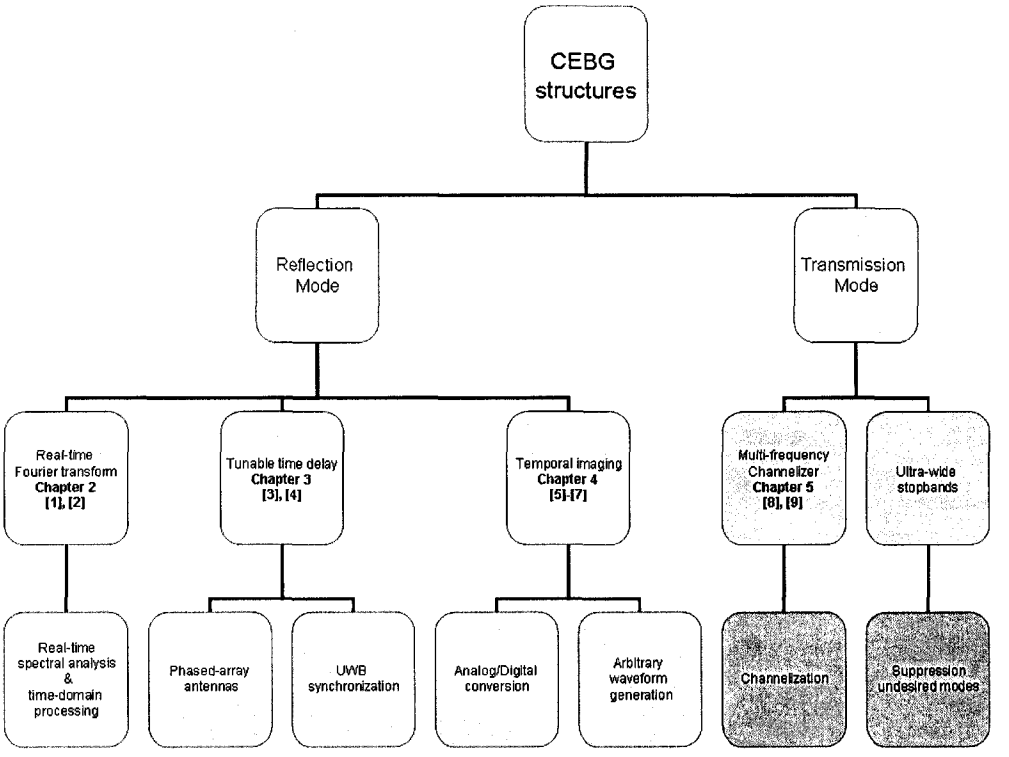

Fig. 6.1 Summary of the work described in this thesis. Work in Chapter 5 on investigating the transfer of CEBG ideas to stripline and CPW structure is not included/ published at this time.

6.2 Future Research

Although many of the first-time demonstrations shown here were useful in proving the principles of operation, the optimization of these systems will require intensive research. Among the most significant obstacles to CEBG-oriented electronic systems are: (i) the scale of the devices themselves; (ii) the ripple of their responses (amplitude & group delay); (iii) losses associated with coupling reflected signals; and (iv) system resolution and aperture limitations. The issues associated with (ii) and (iii), while of interest, are not seriously limiting to functionality (even with dramatic group-delay ripple, we have seen in this work that signals of sufficient bandwidth tend to see mostly the first-order linearity). Furthermore, some very promising 3-dB couplers for UWB have recently been proposed in microstrip [10], addressing (iii). We will briefly explore some potential research directions addressing (i) and (iv).

6.2.1 Sub-Wavelength Structures

One of the primary challenges associated with CEBGs is that, owing to the fact that they require a number of periods to build up a reflectivity, the structures involved tend to be prohibitively long for compact applications. The challenge inherent in trying to reduce the dimension of these structures is that, while it is relatively simple to build resonators that are sub-wavelength in scale, they tend to be inherently narrowband (e.g. consider the popular split-ring resonator or 'SRR' [11], [12]). Although resonators are inherently narrow-band structures, there remains the possibility that with clever design they can be employed to create wideband behaviors: for example, a bandpass filter with over 50% fractional bandwidth (7 GHz bandwidth) was recently demonstrated by using inter-coupled SRRs in a structure only 1.3 cm in length [13]. It is reasonable to assume that there exists a comparable bandstop arrangement of resonators, and it may further be possible to institute a discrete implementation of chirp in such a design simply by staggering the central resonant frequency in a linear fashion. Whether this is sufficient to yield a sufficiently linear group-delay response, or whether the ripple will be too severe, is likely to be a function of how well a continuous chirp can be introduced.

In addition, there has been recent progress towards optical sub-wavelength gratings that exhibit bandgap behavior by using high-contrast index of refraction modulation in the perpendicular direction to the wave [14], [15]. Whether or not this concept can be usefully extended to operate in the microwave regime merits investigation.

6.2.2 Deployment of CEBGs for Continuous-Time Operations

In order to overcome the limitations of short time-windows for operations such as RTFT and temporal imaging, it is necessary to consider how systems involving continuous-time inputs can be developed to perform 'free-running' real-time spectral analysis, and time-magnification and compression operations for ADC and AWG, respectively. Recent demonstrations have shown that this is feasible using photonics-assisted techniques in the context of ADC systems [16],

[17]. In these demonstrations, the continuous input signal was segmented and processed in a parallel manner. A technique referred to as "virtual time-gating" is proposed in [16] whereby the reference impulses which are dispersed and used to effect a time-lens are spaced out (after dispersion) to precisely the inter-pulse timing, and each one modulates a different segment of the original input pulse. Careful filtering can then be applied to distinguish the outputs belonging to each of the parallel channels, which can be separately digitized and then the overall digital signal reconstructed from the channels.

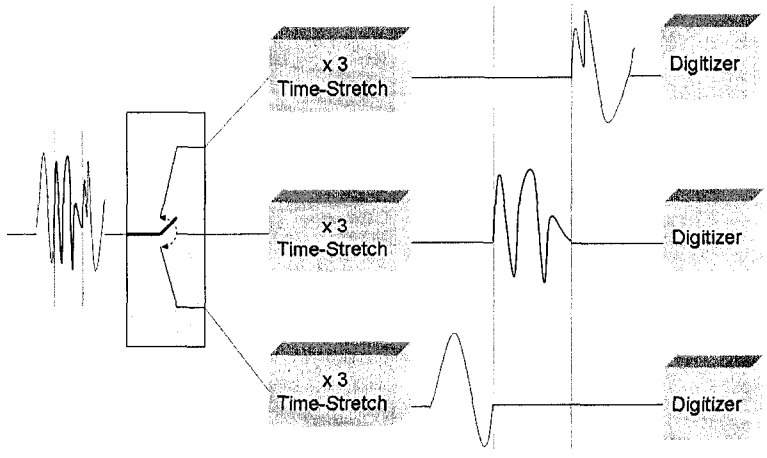

Fig. 6.2 Conceptual illustration of parallel continuous-time ADC using 3 channels, as described in [16].

It is of course of interest to see if such strategies can be adapted to the microwave regime. Parallel configurations requiring a large number of CEBGs would of course consume a lot of space; it is recommended that stacked stripline structures be explored for just this sort of application.

References

[1] J. Schwartz, J. Azaña and D. V. Plant, "Real-time microwave signal processing using microstrip technology," IEEE MTT-S Int. Microw. Symp., San Francisco, CA, USA, pp. 1991-4, Jun. 2006.

[2] J. Schwartz, J. Azaña and D. V. Plant, "Experimental demonstration of real-time spectrum analysis using dispersive microstrip," IEEE Microwave Compon. Lett., vol. 16, n. 4, pp. 215-217, Apr. 2006.

[3] J. Schwartz, J. Azaña and D. V. Plant, "Design of a tunable UWB delay-line with nanosecond excursions using chirped electromagnetic bandgap structures," Proc. 4th IASTED Int. Conf. Antennas, Radar and Wave Prop., Montreal, Canada, #566-814, May 2007.

[4] J. Schwartz, I. Arnedo, M. A. G. Laso, T. Lopetegi, J. Azaña and D. V. Plant, "An electronic UWB continuously tunable time-delay system with nanosecond delays," submitted to IEEE Microwave Compon. Lett., Jul. 2007.

[5] J. Schwartz, J. Azaña and D. V. Plant, "An electronic temporal imaging system for compression and reversal of arbitrary UWB waveforms," submitted to IEEE Radio & Wireless Symp. (RWS 2008), Jan. 2008.

[6] J. Schwartz, J. Azaña and D. V. Plant, "A fully-electronic time-stretch system," **Best Student Paper**, 12th Int. Symp. Antenna Technology and Applied Electromagnetics (ANTEM/URSI), pp. 119-22, Jul. 2006.

[7] J. Schwartz, J. Azaña and D. V. Plant, "A fully-electronic system for the time magnification of GHz electrical signals," IEEE Trans. Microwave Theory Tech., v.55, n.2, pp. 327-334, Feb. 2007.

[8] J. Schwartz, Michael M. Guttman, J. Azaña and D. V. Plant, "Multi-channel filters using chirped bandgap structures in microstrip technology," IEEE Microwave Compon. Lett., v. 17, no. 8, pp. 577-9, Aug. 2007.

[9] J. Schwartz, M. Guttman, J. Azaña and D. V. Plant, "A multiple-frequency resonator in microstrip technology," 12th Int. Symp. Antenna Technology and Applied Electromagnetics (ANTEM/URSI), pp. 569-72, Jul. 2006.

[10] A. M. Abbosh and M. E. Bialkowski, "Design of compact directional couplers for UWB applications," IEEE Trans. Microwave Theory Tech., vol. 55, no. 2, pp. 189-94, Feb. 2007.

[11] J. B. Pendry, A. J. Holden, D. J. Robbins and W. J. Stewart, "Magnetism from conductors and enhanced nonlinear phenomena," IEEE Trans. Microwave Theory Tech., vol 47, no. 11, pp. 2075-84, Nov. 1999.

[12] P. Gay-Balmaz and O. J. F. Martin, "Electromagnetic resonances in individual and coupled split-ring resonators," J. Appl. Phys., vol. 92, no. 5, pp. 2929-36, Sept. 2002.

[13] J. Wu, S. N. Qiu, C. X. Qiu and I. Shih, "Wideband microstrip bandpass filter based on intercoupled split-ring resonator," Microw. Opt. Tech. Lett., vol. 49, no. 8, pp. 1809-13, Aug. 2007.

[14] C. F. R. Mateus, M. C. Y. Huang, Y. Deng, A. R. Neureuther and C. J. Chang-Hasnain, "Ultrabroadband mirror using low-index cladded subwavelength grating," IEEE Photon. Tech. Lett., vol. 16, no. 2, pp. 518-20, Feb. 2004.

[15] E. Bisaillon, D. Tan, B. Faraji, A. G. Kirk, L. Chrowstowski and D. V. Plant, "High reflectivity air-bridge subwavelength grating reflector and Fabry-Perot cavity in AlGaAs/GaAs," Optics Express, vol. 14, no. 7, pp. 2573-82, Apr. 2006.

[16] Y. Han and B. Jalali, "Continuous-time time-stretched analog-to-digital converter array implemented using virtual time gating," IEEE Trans. Circ. Syst. I: Regular Papers, vol. 52, no. 8, pp. 1502-7, Aug. 2005.

[17] G. C. Valley, G. A. Sefler, J. Chou and B. Jalali, "Continuous time realization of time-stretch ADC," Int. Top. Meet. Microw. Photon., pp. 271-3, Oct. 2006.

Theory of Temporal Imaging

In this appendix we present a brief mathematical treatment following the work of Caputi [1] in the context of microwave systems. Although a slightly different mathematical framework was laid out more recently by Kolner [2], we treat the original approach since it is more in keeping with our microwave interpretation of temporal imaging, and our system most closely mirrors Caputi's configuration. For the purposes of this analysis, we will use $S(\omega)$ to denote the Fourier transform of $s(t)$. To begin, we consider a general complex input signal of the form:

$$s(t)e^{j\omega t} \tag{1}$$

For reasons that will soon become clear, we now make the assumption that the input is on a carrier frequency of $\omega_1+\omega_2$, and that this frequency is greater than the single-sided bandwidth of $s(t)$ (i.e. no aliasing in the up-conversion). We also rewrite the signal in a form that anticipates our treatment:

$$s'(t)e^{j[(\omega_1+\omega_2)t-(a+b)t^2]} \qquad s'(t)=s(t)e^{j(a-b)t^2} \tag{2}$$

We now create the first all-pass dispersive network, which is designed to introduce a group delay slope of $\sigma_{in} = 2\pi/(a+b)$ and whose phase response is centered at the carrier frequency of our signal.

$$H(\omega)=\exp\left(j\frac{(\omega-(\omega_1+\omega_2))^2}{-4(a+b)}\right) \tag{3}$$

We invoke a mathematical form for the time-domain output of the convolution of a signal of form $s(t)\exp(j(\omega_o t \pm kt^2))$ with the time-domain $h(t)$ for a quadratic filter centered at ω_o of form $H(\omega) = \exp(j(\omega-\omega_o)^2/\pm 4k)$ [3], which results in the form:

$$\sqrt{\frac{a+b}{\pi}}S'(2(a+b)t)\exp\{j[(\omega_1+\omega_2)t+(a+b)t^2-\frac{\pi}{4}]\} \tag{4}$$

Where it is clear that we have used k = (a+b) and $\omega_o = \omega_1+\omega_2$ and our motivation for the mathematical rewriting in (2) should be apparent. It should also be clear that we are now working with a time-scaled Fourier transform of the original signal, as expected from a dispersive filter. We now perform the time-lensing operation by mixing with a linear frequency sweep LO(t) (quadratic phase modulation in time with group delay slope $\sigma_{LO} = 2\pi/a$):

$$LO(t) = 2\cos(\omega_1 t + at^2) \tag{5}$$

Taking the product of (4) and (5) and filtering for only the difference frequency, we find:

$$\sqrt{\frac{a+b}{\pi}}S'(2(a+b)t)\exp\{j[\omega_2 t+bt^2-\frac{\pi}{4}]\} \tag{6}$$

The final step is to introduce the output dispersion element which is compressive [note the change of sign as compared to (3)], centered at the new carrier frequency ω_2 and has group delay slope $-\sigma_{out} = 2\pi/b$:

$$H(\omega) = \exp(j\frac{(\omega-\omega_2)^2}{4b}) \tag{7}$$

The product that results has now undergone a double-Fourier transform:

$$\sqrt{\frac{a+b}{\pi}}\sqrt{\frac{b}{\pi}}S^*(-2bt)\exp[j(\omega_2 t+bt^2)] \tag{8}$$

where the double Fourier-transform $S^*(-2bt)$ can be expressed as:

$$\begin{aligned} S^* &= \int m'(\lambda)\int\exp\{-j\tau[2(a+b)\lambda-2bt]\}d\tau d\lambda \\ &= \int m'(\lambda)\cdot 2\pi\delta[2(a+b)\lambda-2bt]d\lambda \end{aligned} \tag{9}$$

where δ is the Dirac (delta) function. We can solve the integral of (9) using the change of variables $\mu = 2(a+b)\lambda$:

$$\int s'(\frac{\mu}{2(a+b)}) \cdot 2\pi\delta(\mu - 2b\tau)\frac{d\mu}{2(a+b)} = \frac{\pi}{(a+b)} s'(\frac{bt}{(a+b)}) \tag{10}$$

Using this result in (8) we find that our output can be expressed as:

$$\begin{aligned} &\sqrt{\frac{a+b}{\pi}}\sqrt{\frac{b}{\pi}}\frac{\pi}{(a+b)} s'(\frac{bt}{(a+b)})\exp[j(\omega_2 t + bt^2)] \\ &= \sqrt{\frac{b}{a+b}} s'(\frac{bt}{a+b})\exp[j(\omega_2 t + bt^2)] \\ &= \sqrt{\frac{b}{a+b}} s(\frac{bt}{a+b})\exp[j(\omega_2 t + at^2)] \end{aligned} \tag{11}$$

Where we have invoked (2) to restore our treatment to input signal s(t). If we define the magnification factor M as (a+b)/b it is easy to see that the envelope of the resulting chirped signal of (11) is:

$$\sqrt{\frac{1}{M}} s(\frac{t}{M}) \tag{12}$$

This result captures both the voltage amplitude-scaling factor and the time-scaling factor that has been applied to the input. If we rewrite M in terms of group delay slope, we have $M = -\sigma_{out}/\sigma_{in}$[1], suggesting that tuning the ratio of output and input group delay slopes is a simple way to design the system magnification.

References

[1] W. J. Caputi, "Stretch: A time transformation technique," IEEE Trans. Aersop. Electron. Syst., vol. AES-7, no. 2, pp. 269-78, Mar. 1971.

[2] B. H. Kolner, "Space-time duality and the theory of temporal imaging," IEEE J. Quantum Electron., vol. 30, pp. 1951-63, Aug. 1994.

[1] Caputi's treatment differs slightly in terminology in a way that may provoke confusion – Caputi defines σ in units of Hz/second whereas in this thesis and related published works we consistently describe σ in seconds/Hz. We apologize for this potentially confusing choice of terms!

[3] J. R. Klauder, A. C. Price, S. Darlington and W. J. Albersheim, "Theory and design of chirp radars," Bell System Tech. J., vol. 39, no. 4, pp. 745-808, Jul. 1960.

APPENDIX B

Analog Multiplier

In this appendix we briefly discuss the analog multiplier constructed for our demonstration of temporal imaging. This circuit, in conjunction with a reference frequency sweep, served as a time lens in our imaging demonstration. Our purpose in designing an analog multiplier was threefold:

(i) To provide broadband conversion gain to offset other system losses

(ii) To produce a faithful analog product at the output with minimal feed-through and harmonics for two time-limited and chirped inputs

(iii) To provide a low-pass output filter to isolate the difference-frequency output

Although these functions could have been performed independently, we observed that they could be efficiently handled together by designing a custom-built analog multiplier.

Our multiplier was based on a standard double-balanced Gilbert-cell architecture [1] with added predistortion circuitry. This architecture has previously been shown to be suitable for very broad operating bandwidths approaching 20 GHz by using judicious choice of impedance matching schemes [2], [3]. Our input range of frequencies (signal and reference sweep) was from 2 to 10 GHz, with a difference-frequency output range from 0.5-2 GHz. We chose a differential multiplier topology to improve the conversion gain performance based on the availability of a differential broadband signal. Briefly, a basic double-balanced Gilbert core with some emitter degeneration resistance is presented in Fig. B.1. Although we will forego detailed analysis here (this kind of circuit is extensively covered in the literature), it can be shown that the circuit of Fig. B.1 yields a differential output of approximately:

$$V_{o+} - V_{o-} \approx -2\frac{R_C}{R_E} I_o \tanh(\frac{v_1}{2V_T}) \tanh(\frac{v_2}{2V_T}) \quad \text{(B.1)}$$

where V_T is the thermal voltage. It is evident that for small-signal inputs, the tanh functions can be linearized and a term proportional to the direct product of the two inputs emerges (i.e. proportional to $v_1 \cdot v_2$), which for sinusoidal inputs yields a sum- and difference-frequency term. Because we have control over the signal amplitude but were less certain about the amplitude of our eventual reference sweep (created using a dispersed impulse) we included a predistortion circuit to compensate for potentially larger inputs that would otherwise result in non-linear tanh-like behavior.

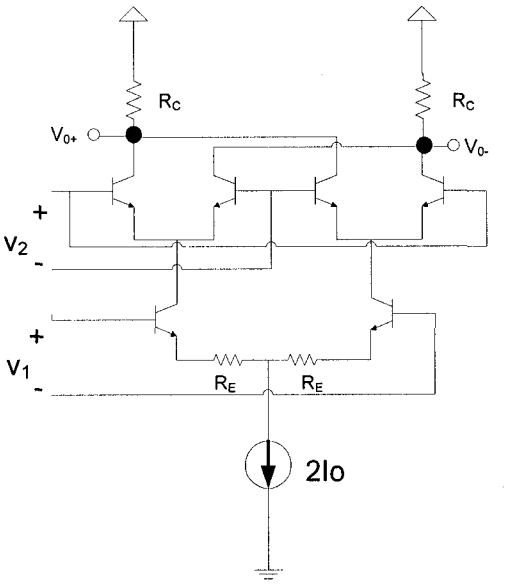

Fig. B.1. Classical Gilbert cell arrangement for a double-balanced mixer

The analog multiplier was fabricated in an available 0.5-micron SiGe BiCMOS technology (cutoff frequency f_T = 47 GHz), although this was far from state-of-the-art even at the time. The design was exclusively created using bipolar transistors (since no logic was required and our current budget was not limited), although this choice was generally not critical and a CMOS-flavor design could just as easily have been deployed. All simulations and designs were carried out using the Cadence software suite.

Our realized circuit is presented in Fig. B.2, through which we will refer to points 'A'-'F' to discuss aspects of the design. We designed for a +3.3V supply

and used simple resistive networks for broadband impedance matching (point 'A') since power consumption was not a concern for this demonstration – although we acknowledge that it would have been vastly superior from both a noise and power perspective to institute a broadband LC-ladder type network instead as in other recent broadband multiplier demonstrations [2], [3]. Stage 'B' forms a simple current mirror that drives both stages of the circuit.

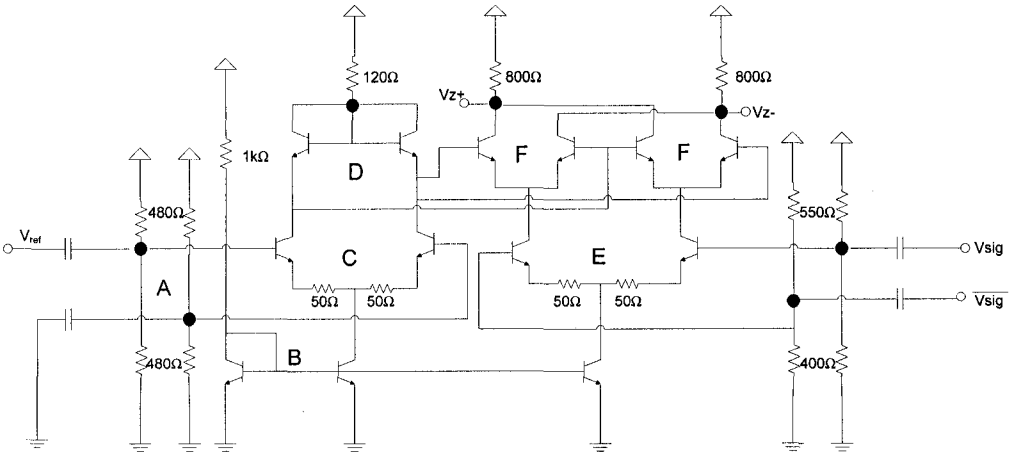

Fig. B.2. Schematic of our Gilbert core

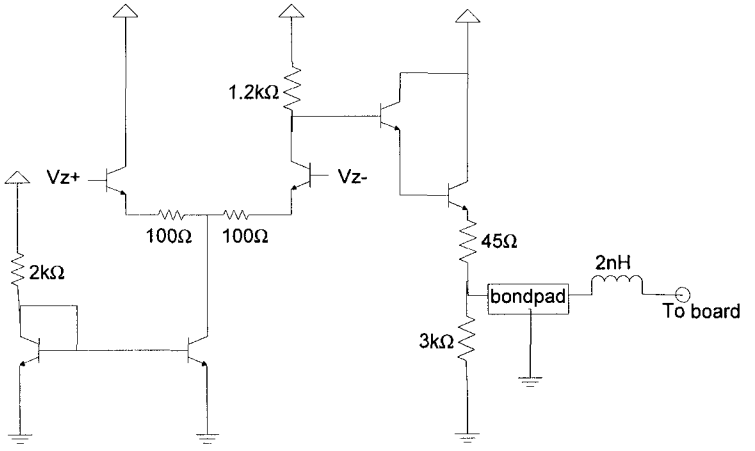

Fig. B.3 Output diff-to-single-ended conversion and buffer with bondpad and wirebond

Although a differential input signal was available, the reference frequency sweep was assumed to be a single-ended input since a differential impulse-generator was not available. The function of the block depicted at points 'C' and 'D' was to produce a predistorted output proportional to the inverse-tanh of the input reference frequency sweep and therefore avoid potentially non-linear

behavior. Parts 'E' and 'F' formed the fundamental double-balanced Gilbert cell mixer and were driven differentially by V_{sig}. This stage is followed by a differential-to-single-ended conversion step (Fig. B.3) and output buffer designed with the bondpad and wirebond to yield 50-Ω output impedance for up to ~3 GHz.

After layout and extraction, the design yielded voltage conversion gains of about 2 V/V (relative to the signal input) for 100 mV input waveforms at the signal and reference sweep with a difference-frequency of 1 GHz, although a gain roll-off occurred that reduced this to 1.2 V/V when the difference-frequency increased to 2 GHz. The gain roll-off was steep but in fact was generally compensated for by the roll-off in amplitude of the reference frequency sweep itself (going from 300mV to 150mV as depicted in Fig. 4.8), which was of a similar slope but an inverse orientation (i.e. lower amplitude for the lower difference-frequency product, which occurred at the higher-end frequencies), giving us acceptable results without the need for post-processing. This auspicious result is a fortunate example of two undesired effects canceling each other's influence.

The final design loosely occupied a $1mm^2$ area (shared with another design). The chip was wirebonded into a 24-pin ceramic flat package mounted on a simple test board (PCB-TF2) provided by the Canadian Microelectronics Corporation (CMC). Input signals were brought on-chip using high-frequency probes from Cascade Microtech's Infinity™ series, while a difference-frequency, single-ended output of 1-2.5 GHz was passed off-chip via wirebond through the test board to an SMA output. Sum-frequencies generated by the mixing process were inherently filtered by the combination of inductive wirebond, bondpad and the board itself (limited to ~3 GHz), which effectively acted a low-pass filter since the sum-frequencies spanned 4.5-20 GHz. The multiplier's functionality was verified with tone-inputs and yielded lower overall conversion gain than expected by approximately 2 dB (since the current draw was very close to the target, the authors suspect some external impedance mismatch – a design error occurred in which an output capacitor was omitted and an external bias-T network was

required). Despite this setback, difference-frequency outputs were clearly distinguishable for the target range of frequencies across the full range of input frequency combinations.

Future designs could certainly be improved upon with regards to both conversion gain and flatness, particularly by incorporating some high-quality reactive components in design. Furthermore, no efforts were made here to minimize noise or to operate under any power/current constraints, which may be significant to practical implementations in the future. The author wishes to stress that this design served the purposes of a proof of principle demonstration of temporal imaging and does not itself represent a novel contribution.

References

[1] B. Gilbert, "A precise four-quadrant multiplier with subnanosecond response," IEEE J. Solid-State Circ., vol. SC-3, no. 4, pp. 365-73, Dec. 1968.

[2] B. Tzeng, C. Lien, H. Wang, Y. Wang, P. Chao, and C. Cheng, "A 1-17-GHz InGaP-GaAs HBT MMIC analog multiplier and mixer with broad-band input-matching networks," IEEE Trans. Microwave Theory Tech., vol. 50, no. 11, pp. 2564-2568, November 2002.

[3] M. D. Tsai, C. S. Lin, C. H. Wang, C. H. Lien, and H. Wang, "A 0.1-23-GHz SiGe BiCMOS analog multiplier and mixer based on attenuation-compensation technique" IEEE Radio Freq. Integr. Circ. (RFIC) Symp., pp.417-420, 2004.